

WINGLETS FOR WIND TURBINES:
AN EXPERIMENTAL STUDY ON AERODYNAMIC PERFORMANCE AND
TIP VORTEX BEHAVIOR

A THESIS SUBMITTED TO
THE GRADUATE SCHOOL OF NATURAL AND APPLIED SCIENCES
OF
MIDDLE EAST TECHNICAL UNIVERSITY

BY

YAŞAR OSTOVAN

IN PARTIAL FULFILLMENT OF THE REQUIREMENTS
FOR
THE DEGREE OF DOCTOR OF PHILOSOPHY
IN
AEROSPACE ENGINEERING

OCTOBER 2017

Approval of the thesis:

**WINGLETS FOR WIND TURBINES:
AN EXPERIMENTAL STUDY ON AERODYNAMIC PERFORMANCE AND
TIP VORTEX BEHAVIOR**

submitted by **YAŞAR OSTOVAN** in partial fulfillment of the requirements for the degree of **Doctor of Philosophy in Aerospace Engineering Department, Middle East Technical University** by,

Prof. Dr. Gülbin Dural Ünver
Dean, Graduate School of **Natural and Applied Sciences**

Prof. Dr. Ozan Tekinalp
Head of Department, **Aerospace Engineering**

Assoc. Prof. Dr. Oğuz Uzol
Supervisor, **Aerospace Engineering Dept., METU**

Examining Committee Members:

Prof. Dr. İsmail H. TUNCER
Aerospace Engineering Dept., METU

Assoc. Prof. Dr. Oğuz Uzol
Aerospace Engineering Dept., METU

Assoc. Prof. Dr. M. Metin Yavuz
Mechanical Engineering Dept., METU

Asst. Prof. Dr. Munir Elfarra
Aerospace Eng. Dept., Ankara Yıldırım Beyazıt University

Asst.Prof. Dr. Mustafa Kaya
Aerospace Eng. Dept., Ankara Yıldırım Beyazıt University

Date: 16.10.2017

I hereby declare that all information in this document has been obtained and presented in accordance with academic rules and ethical conduct. I also declare that, as required by these rules and conduct, I have fully cited and referenced all material and results that are not original to this work.

Name, Last Name : Yaşar Ostovan

Signature :

ABSTRACT

WINGLETS FOR WIND TURBINES: AN EXPERIMENTAL STUDY ON AERODYNAMIC PERFORMANCE AND TIP VORTEX BEHAVIOR

Ostovan, Yaşar

Ph.D., Department of Aerospace Engineering

Supervisor: Assoc. Prof. Dr. Oğuz Uzol

October 2017, 103 pages

This study experimentally investigated the effects of winglets on power performance and tip vortex behavior of two interacting similar model horizontal axis wind turbines. Power performance of both turbines positioned in-line was measured with and without winglets attached to the blade tips of the upstream turbine. Results showed that power coefficient of upstream turbine increased about 3% operating with winglets around rotor design TSR. Downstream turbine produced less energy while operating in the wake of the “wingletted” upstream turbine. However, the overall efficiency of two turbines increased with winglets. Trajectories of three vortex structures shed from three consecutive blades of the rotor were captured in Phase-locked PIV measurements covering 120 degrees of azimuthal progression of the rotor. The impact of using winglets on the flow field near the wake boundary as well as on the tip vortex characteristics were investigated. Results showed that winglets initially generated an asymmetric co-rotating vortex pair, which eventually merged together after about 10 tip chords downstream. Mutual induction of the initial double vortex structure caused a faster downstream convection and a radially outward motion of tip vortices. The wake boundary was shifted radially outwards, and velocity gradients were diffused. Vorticity and turbulent kinetic energy levels were significantly reduced across the wake boundary and within the vortex core. The vortex core sizes were tripled. Results showed consistency with various vortex core and expansion models. The estimated induced drag reduction was about 15% with winglets. Meandering analysis showed that the meandering amplitude increased as the vortices aged.

Keywords: Winglets, Wind Turbines, Tip Vortex, Vortex Models, Particle Image Velocimetry

ÖZ

RÜZGAR TÜRBİNLERİ İÇİN KANATÇIKLAR: AERODİNAMİK PERFORMANS VE UÇ GIRDABI DAVRANIŞI ÜZERİNDE DENEYSEL BİR ÇALIŞMA.

Ostovan, Yaşar
Doktora, Havacılık ve Uzay Mühendisliği Bölümü
Tez Yöneticisi: Doç.Dr. Oğuz Uzol

Ekim 2017, 103 Sayfa

Bu tez çalışmasında birbirleriyle etkileşim halinde olan iki benzer yatay eksenli rüzgar türbinlerinde kanatçıkların performans ve kanat uç girdabı davranışına etkisi incelenmiştir. İki türbin için de güç performansı ölçümleri öndeki türbinde kanatçık varken ve yokken yapılmıştır. Sonuçlar, öndeki türbin tasarım uç hız oranında çalışırken kanatçıkların kullanılmasıyla bu türbinin performansında %3'lük bir artış olduğunu göstermiştir. Kanatçıklı türbinin arkasında çalışan türbinin ise daha az enerji ürettiği tespit edilmiştir. Ancak, iki türbinin toplam verimi kanatçıkların kullanımıyla artmıştır. Peş peşe gelen kanat uçlarından kopan üç adet girdap yapısının yörüngeleri faz-kilitmeli PIV ölçümleri ile 120 derecelik azimut açısını kapsayacak bir şekilde takip edilmiştir. Türbinin iz bölgesi sınırındaki akışa ve uç girdaplarına olan etkileri incelenmiştir. Sonuçlar kanatçıkların ilk başta asimetric birbiri etrafında dönen bir girdap çifti oluştuğunu ve bu girdap çiftinin 10 uç veteri mesafe sonrasında tek girdap oluşturmak üzere birleştiğini göstermektedir. İki girdap yapısının birbirleriyle olan etkileşimi referans deneylere göre arka bölgede daha hızlı bir girdap konveksiyonu ve yarıçap yönünde dışa doğru bir harekete neden olmuştur. İz sınırı yarıçap yönünde dışa doğru kaymış ve hız gradyanlarında bir yayılma görülmüştür. Vortisite ve türbülans kinetik enerjisi seviyeleri iz bölgesi sınırında ve girdap merkezinde önemli bir ölçüde düşmüştür. Uç girdabı merkezi boyutlarının kanatçıklı durumda referans duruma kıyasla üç kat büyük olduğu görülmüştür. Sonuçlar çeşitli girdap merkezi ve genişleme modelleriyle uyum göstermektedir. Kanatçıklar kullanıldığında indüklenmiş sürüklenmede %15 civarında bir azalma olduğu değerlendirilmektedir.

Anahtar kelimeler: Kanatçık, Rüzgar Türbinleri, Uç Girdabı, Girdap Modelleri, Parçacık Görüntülemeli Akış Ölçümü

To my family

ACKNOWLEDGMENTS

First and for most, I would like to thank my supervisor Assoc. Prof. Dr. Oğuz Uzol. Whose kindness, patience and academic experience are invaluable for me through all these years. Without his enthusiasm, energy, and support, I could not be able to complete this study.

I have been working with lots of MSc and Ph.D. students in the aerodynamics lab, for which I am very grateful. I have enjoyed working and studying with you all. Big thanks go to M. Tugrul Akpolat for spending long nights with me at the aerodynamics lab while we were performing the PIV measurements. I would like to thank my colleague and office-mate Hooman Amiri Hazaveh for nice discussions about various topics related to fluid mechanics. I would like to thank department technician Ahmet Uyar, for all help I received in lab.

Part of this study was performed at NTNU closed-loop wind tunnel. I am grateful to Prof. Lars Roar Sætran for allowing me to use their aerodynamic lab. I would like to thank Jan Bartl for his hospitality and valuable technical discussions during my stay at Trondheim, Norway. I will not forget the NTNU aerodynamics laboratory engineer Arnt Egil and his team, for all the help they provided during the measurements.

Lastly, but most importantly, I would like to express my eternal gratitude to my family for their love and support throughout my life.

This study was supported by METU Center for Wind Energy (RÜZGEM).

TABLES OF CONTENTS

ABSTRACT	v
ACKNOWLEDGMENTS	viii
TABLES OF CONTENTS.....	ix
LIST OF TABLES	xi
LIST OF FIGURES	xii
LIST OF SYMBOLS	xvi
CHAPTERS	
1 INTRODUCTION	1
1.1 Motivation.....	1
1.2 A Qualitative Description of Wind Turbine Aerodynamics	3
1.2.1 Actuator disk theory	5
1.2.2 Rotational effects.....	7
1.2.3 Vorticity based description of the flow through a turbine rotor.....	7
1.2.4 Wake of a wind turbine	8
1.2.5 Wind farm Aerodynamics	9
1.3 Literature Survey on Winglets for Wind Turbines	10
1.3.1 Effects of winglets on wind turbine loads	10
1.3.2 Effects of winglets on the tip vortex.....	12
1.4 Objectives and Scope	13
2 EXPERIMENTAL SETUP AND MEASUREMENT DETAILS.....	15
2.1 Wind Tunnels.....	15
2.1.1 NTNU closed-loop wind tunnel	15

2.1.2	METWIND open jet wind tunnel.....	17
2.2	Model Horizontal Axis Wind Turbines	19
2.3	Winglet Design	24
2.4	Particle Image Velocimetry Measurements	26
2.5	Instrumentation and Uncertainty	28
3	RESULTS AND DISCUSSION	31
3.1	Effects of Winglets on the Performance of Two Interacting Model Wind Turbines and Comparison with Wing Extensions.....	31
3.1.1	NTNU closed-loop tunnel measurements	31
3.1.2	METUWIND open jet tunnel measurements	35
3.2	PIV Measurements of the Effects of Winglets on the Tip Vortex Behavior of the Model Wind Turbine.....	40
3.2.1	Flow field characteristics near the tip	40
3.2.2	Effects on tip vortex characteristics	52
3.2.3	Effects on induced drag.....	59
3.2.4	Vortex meandering analysis	61
4	CONCLUSIONS	75
	REFERENCES	81
	APPENDICES	
	A. DETAILED FIGURES FROM PIV MEASUREMENTS.....	87
	CURRICULUM VITAE.....	101

LIST OF TABLES

Table 2-1 Spanwise chord and twist distribution of the rotor blades.....	20
Table 3-1 Overall efficiency of two turbines	34
Table 3-2 Actual power production of turbines for all three cases	39
Table 3-3 Vortex swirl velocity and core expansion models.....	55
Table 3-4 Coefficient values that give the best fit to the experimental data.....	57

LIST OF FIGURES

Figure 1-1 World total energy consumption from 1971 to 2014 [1]	1
Figure 1-2 (a) Global annual installed wind capacity 2001-2016, (b) Global cumulative installed wind capacity 2001-2016 [3]	2
Figure 1-3 1D flow field through an actuator disk	5
Figure 1-4 Vortex system on a rotating turbine with three blades [9]	8
Figure 1-5 Flow field schematic downstream a turbine [9]	9
Figure 2-1 Schematic of NTNU closed-loop wind tunnel	16
Figure 2-2 (a) Picture of the NTNU closed loop wind tunnel balance system, (b) Picture of the model horizontal axis turbine attached to balance system located inside the NTNU wind tunnel test section.....	16
Figure 2-3 Schematic of the METUWIND open jet wind tunnel	17
Figure 2-4 Hotwire measurements of mean velocity (top row) and turbulence intensity (bottom row) for two different jet exit speeds of 5 m/s (left column) and 11.5 m/s (right column) at several downstream distances from the tunnel jet exit.	18
Figure 2-5 Angular aperture of the shear layer at the exit of METUWIND open jet wind tunnel.....	19
Figure 2-6 A 3D CAD model of the wind turbine	21
Figure 2-7 Front panel screen shot of the LabVIEW code to control rotation speed of both turbines and obtain simultaneous data from torque and thrust sensors. it also monitors the tunnel free stream speed	22
Figure 2-8 Picture of the camera of the PIV system mounted properly in order to adjust rotor blades' pitch angle (a). Screen shots of PIV Dynamic Studio software while performing aluminum (b) and titanium (c) blades' manual pitch adjustment.	23
Figure 2-9 Titanium and aluminum rotors power coefficient measured at free stream velocity of 11.5 m/s.....	23
Figure 2-10 Definitions of winglet design variables.....	25
Figure 2-11 Picture of the winglets attached to the blades of the first turbine; (a) Plastic winglets at NTNU closed-loop wind tunnel, (b) Aluminum winglets at METUWIND open jet wind tunnel.....	25
Figure 2-12 Picture of the facility while performing PIV measurements.....	27
Figure 2-13(a) Phase definitions and sample three phases, (b) PIV domain.....	27

Figure 3-1 Power coefficient variations with TSR measured for upstream turbine with and without winglets at NTNU wind tunnel with freestream velocity of 11.5 m/s. ...32

Figure 3-2 Thrust coefficient variations with TSR measured for upstream turbine with and without winglets at NTNU wind tunnel with freestream velocity of 11.5 m/s. ...32

Figure 3-3 Power coefficient for downstream turbine with three and six rotor diameters distance in between while the upstream turbine is operating at TSR=6 (rotor design TSR) with and without winglets34

Figure 3-4 Thrust coefficient for downstream turbine with three rotor diameter distance in between while the upstream turbine is operating at TSR=6 with and without winglets (all coefficients are calculated according to free stream velocity equal to 11.5 m/s).....35

Figure 3-5 Individual turbine baseline (no tip devices) power performance comparison between measurements at NTNU closed loop and METUWIND open jet wind tunnels.36

Figure 3-6 Power coefficient measurement results of first turbine with winglets37

Figure 3-7 Power coefficient measurement results of first turbine with wing extensions38

Figure 3-8 Power coefficient for downstream turbine with 3 rotor diameters distance in between while the upstream turbine is operating at TSR=6 (rotor design TSR) without any tip devices, with winglets, and with wing extensions (all coefficients are calculated according to free stream velocity equal to 11.5 m/s).39

Figure 3-9 (a) A sample PIV raw image for the baseline case at phase angle $\Phi=36^\circ$, (b) and (c) corresponding phase averaged velocity \bar{u} and out-of-plane vorticity $\overline{\Omega_z}$ distributions near the blade tip, respectively, superimposed by vortex induced velocity vectors. The free stream flow is from left to right. The dashed rectangle represents the blade position at phase $\Phi=0^\circ$. Point $\frac{y'}{R} = \frac{x'}{R} = 0$ represents the position of the blade tip at phase= 0°41

Figure 3-10 Phase-averaged distribution of axial velocity \bar{u} of rotor phases 0° to 120° for the baseline (left) and winglet (right) cases with 24-degree intervals.....47

Figure 3-11 Phase-averaged distribution of out-of-plane vorticity ($\overline{\Omega_z}$) of rotor phases 0° to 120° for the baseline (left) and winglet (right) cases with 24-degree intervals.48

Figure 3-12 Turbulent kinetic energy distribution of rotor phases 0° to 120° for the baseline (left) and winglet (right) cases with 24-degree intervals.49

Figure 3-13 The overall average of 21 phases (0° to 120° with 6-degree intervals) for (a) phase-locked average axial velocity, (b) turbulent kinetic energy and (c) phase-locked average vorticity of each phase angle for baseline (left) and winglet cases (right).....50

Figure 3-14 Data extracted from a vertical line at $\frac{y'}{R} = 0.8$ from the overall average of 21 phases (0° to 120° with 6-degree intervals) for (a) axial velocity, (b) out-of-plane vorticity and (c) turbulent kinetic energy for baseline and winglet cases.....	51
Figure 3-15 Vortex center positions from vortex age 30° to 330° with 30-degree intervals for the baseline and winglet cases.	53
Figure 3-16 (a) Vortex induced swirl (tangential) velocity magnitude, (b) out-of-plane vorticity and (c) turbulent kinetic energy distributions along a horizontal line intersecting the center of second vortex core at rotor phase 60° (vortex age 180°). Horizontal axis is the non-dimensional distance from the vortex core center normalized by the tip chord length of the rotor blade, c	54
Figure 3-17 Comparison of vortex core models with current experimental data for the second vortex at rotor phase 60° (vortex age 180°) for (a) baseline and (b) winglet cases.	57
Figure 3-18 Vortex core growth for the baseline case from vortex age 12° to 348° with 6-degree intervals compared to winglet case. The vortex core expansion model of Sant et al. [38] is also presented.....	58
Figure 3-19 Estimated rotor induced drag for baseline and winglet cases, calculated for rotor phases 24° to 114°	60
Figure 3-20 Schematic of the path used to calculate circulation around each node. .	62
Figure 3-21 vortex center locations obtained from instantaneous vector maps for vortex age 30° to vortex age 330° with 30-degree intervals.....	63
Figure 3-22 Vortex meandering amplitude in axial and lateral directions for baseline and winglet vortices.	64
Figure 3-23 Comparison of swirl velocity magnitude (a), vorticity (b) and turbulent kinetic energy (c) distribution along a horizontal line intersecting the vortex core center for conditionally phase-averaged and normal phase-averaged data for vortex age 60° for the baseline case.	66
Figure 3-24 Comparison of swirl velocity magnitude (a), vorticity (b) and turbulent kinetic energy (c) distribution along a horizontal line intersecting the vortex core center for conditionally phase-averaged and normal phase-averaged data for vortex age 210° for the baseline case.	67
Figure 3-25 Comparison of swirl velocity magnitude (a), vorticity (b) and turbulent kinetic energy (c) distribution along a horizontal line intersecting the vortex core center for conditionally phase-averaged and normal phase-averaged data for vortex age 300° for the baseline case.	68
Figure 3-26 Swirl velocity distribution in conditional averaged data (a) and normal averaged data (b), for vortex ages 60° , 210° and, 300° for the baseline case over a horizontal line intersecting the vortex centers.	71

Figure 3-27 Vortex viscous core radius growth with vortex age for conditional and normal averaged data. The vortex core expansion model of Sant et al. [38] is also presented.	71
Figure 3-28 Maximum vorticity occurring at vortex core centers for the conditionally and normal averaged data of baseline vortex from vortex age 30° to 330°.....	72
Figure 3-29 Maximum turbulent kinetic energy magnitudes occurring at vortex core centers for the conditionally and normal averaged data of baseline vortex from vortex age 30° to 330°.....	72
Figure 3-30 Comparison of swirl velocity magnitude (a), vorticity (b) and turbulent kinetic energy (c) distribution along a horizontal line intersecting the vortex core center for conditionally phase-averaged and normal phase-averaged data for vortex age 240° for the winglet case	73
Figure 3-31 Self-similar distributions of swirl velocity in conditional averaged data of baseline vortex (ages 60°, 210°, and 300°)	74
Figure A. 1 Phase-averaged distribution of axial velocity \bar{u} of rotor phases 0° to 120° for the baseline (left) and winglet (right) cases with 6-degree intervals.....	88
Figure A. 2 Phase-averaged distribution of axial velocity \bar{v} of rotor phases 0° to 120° for the baseline (left) and winglet (right) cases with 6-degree intervals.....	91
Figure A. 3 Phase-averaged distribution of out-of-plane vorticity ($\overline{\Omega_z}$) of rotor phases 0° to 120° for the baseline (left) and winglet (right) cases with 6-degree interval....	94
Figure A. 4 Turbulent kinetic energy distribution of rotor phases 0° to 120° for the baseline (left) and winglet (right) cases with 6-degree intervals.	97

LIST OF SYMBOLS

Acronyms

CFD	Computational Fluid Dynamics
CTA	Constant temperature anemometry
HAWT	Horizontal Axis Wind Turbine
PIV	Particle Image Velocimetry
RPM	Revolution per minute
TKE	Turbulent kinetic energy

Dimensionless numbers

C_P	Power coefficient, $C_P = \frac{P}{\frac{1}{2}\rho_{air}U_{\infty}^3 A_{rotor}}$
C_T	Thrust coefficient, $C_T = \frac{T}{\frac{1}{2}\rho_{air}U_{\infty}^3 A_{rotor}}$
Re	Reynolds number, $Re_D = \frac{UD}{\nu}$
TSR	Tip speed Ratio, $\lambda_R = \frac{\Omega R}{U_{\infty}}$

Roman Symbols

c	tip chord length of rotor blade
k	turbulent kinetic energy
$\langle k \rangle$	overall average turbulent kinetic energy
P	wind turbine power
r	radial distance from vortex core center

R	Wind turbine rotor radius
D	Wind turbine rotor diameter
r_c	vortex core radius
T	Wind turbine thrust
\bar{u}	phase average axial velocity
$\langle \bar{u} \rangle$	overall average axial velocity
$\overline{u_v}$	phase average vortex induced axial velocity
\bar{u}_{core}	average vortex core convection axial velocity
\bar{v}	phase average lateral velocity
$\langle \bar{v} \rangle$	overall average lateral velocity
$\overline{v_v}$	phase average vortex induced lateral velocity
\bar{v}_{core}	average vortex core convection lateral velocity
V_θ	vortex induced swirl (tangential) velocity
x'	x coordinate with the blade tip at the origin
y'	y coordinate with the blade tip at the origin

Greek Symbols

Γ_∞	vortex circulation in the far field
δ_ν	turbulent viscosity coefficient

ν	kinematic viscosity
ρ_∞	air density
Φ	rotor phase angle (degree)
$\overline{\Omega_z}$	phase average out-of-plane vorticity
$\langle \overline{\Omega_z} \rangle$	overall average out-of-plane vorticity

CHAPTER 1

INTRODUCTION

1.1 Motivation

Humankind demand for energy is growing tremendously over recent decades. According to International Energy Agency report [1], the annual energy consumption in the world has been increased by more than 2.5 times from 1971 to 2014 (Figure 1-1). On the other hand, the traditional energy resources like coal, oil, and natural gas reserves are limited and will finish in the near future. So, there is a necessity to produce energy from sustainable resources which already got a large amount of interests in recent years.

World¹ total primary energy supply (TPES) from 1971 to 2014 by fuel (Mtoe)

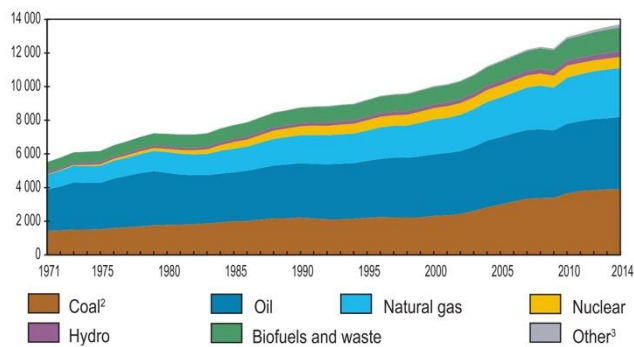
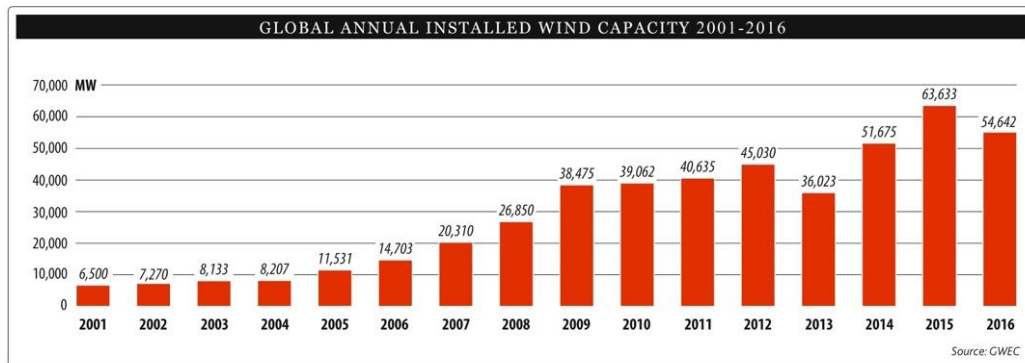


Figure 1-1 World total energy consumption from 1971 to 2014 [1]

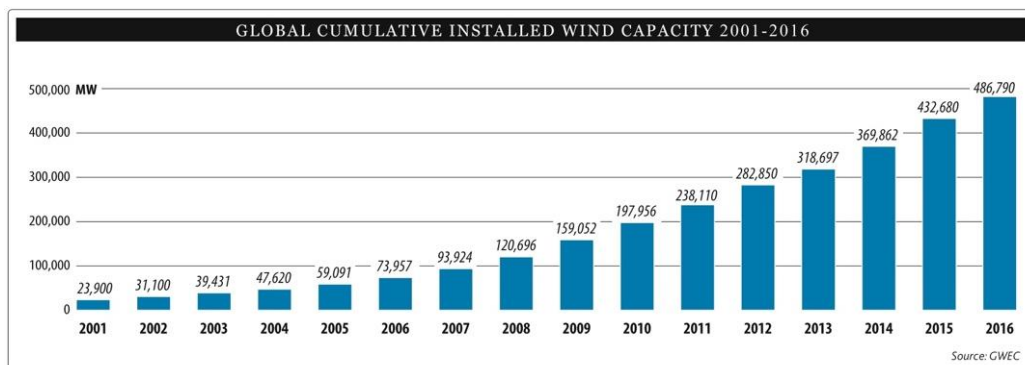
Currently, the contribution of renewable energy in total final energy consumption is about 18%. Half of this portion is for traditional renewables like biomass fuels used for heating and cooking. The other half belongs to modern renewables like wind and solar energies. Another interesting point is that since 2012, new generating capacity

for energy production supplied by renewable resources has exceeded that fueled by non-renewables. For instance, in 2015, installed capacity from renewables represented 61% of all new power generating capacity added worldwide [2].

Renewable power is now competitive with conventional sources of energy, as their costs have dropped substantially in recent years. For example, The cost of wind



(a)



(b)

Figure 1-2 (a) Global annual installed wind capacity 2001-2016, (b) Global cumulative installed wind capacity 2001-2016 [3]

turbines has reduced by nearly three times since 2009 [2].

Wind energy along with solar power is one of the most important renewable energy resources. The global total installed capacity of wind energy at the end of 2016 was 486.8 GW, corresponding to a cumulative annual market growth of more than 12%. This means an approximate annual installed capacity of about 50 GW (Figure 1-2). According to wind energy market forecasts, annual global installed capacity will grow

up to 66.5 GW by the year 2019 which will lead to a global cumulative installed capacity of 666.1 GW [3].

Considering these numbers, it is certain that the future wind farms will consist of a higher number of wind turbines with higher power production capacities. Turbines with higher power production mean larger rotors. On the other hand, there are always constraints on the rotor diameter of wind turbines because of structural loads [4]. Moreover, by increasing rotor diameters of turbines, larger areas are required to establish windfarms because of the wake interactions of turbines. To produce more power while maintaining the rotor diameter, wind turbines need to have higher power coefficients.

One of the possible ways of maximizing the power coefficient, C_P , is adding tip devices to the blades to minimize the aerodynamic tip losses. Winglets are one of the most common used tip devices in aerodynamics. Nowadays, winglets are a part of wing design for almost all modern commercial airplanes. Using winglets can reduce the induced drag and hence, increase the aerodynamic performance of flying devices[5]. This study presents an experimental investigation of the effects of a designed set of winglets on the power performance of two in-line positioned model wind turbines. The effect of the winglets on the behavior of tip vortices shed from the blade tips were also investigated utilizing phase-locked PIV measurements. This would help to get a better understanding of the flow physics when there are winglets attached to the blade tips. Moreover, this set of experimental data could be a valuable validation case for numerical simulations.

1.2 A Qualitative Description of Wind Turbine Aerodynamics

The history of wind power illustrates a general advancement from the use of light and simple drag-based wind turbines to giant but material-efficient lift-based devices in the modern era. The first windmills were established to mechanize the tasks such as grain-grinding and water-pumping. The earliest known wind turbine design is the vertical axis system developed in Persia about 500-900 A.D.

In the wind energy science, aerodynamics is one of the oldest fields. Lanchester predicted the maximum efficiency of an ideal wind turbine known as '*Betz limit*' [6] in 1915. Since then, although there have been lots of efforts for better understanding of wind turbine aerodynamics, there are still some aspects that are not fully understood or quantified. Some reasons are described below. [7]

- Wind turbines operate in the lowest part of the earth boundary layer. Hence, all aerodynamic conditions faced by wind turbines are essentially unsteady (i.e., steady wind is an off-design condition for them).
- Wind turbines count on the stall for torque limitation in high wind speeds, so a detailed understanding of unsteady (deep) stall phenomena is crucial.
- Due to three-dimensionality of the flow in the tip and root regions of the rotor blades, 2D airfoil data may not be sufficient for accurate wind turbine design. For instance, the flow in the boundary layer at the root region is in spanwise direction due to the centrifugal and Coriolis forces, while the flow just outside the layer is chord wise.

In recent years, people started to position a large number of wind turbines together in wind farms in order to reduce the maintenance as well as electricity transfer costs. On the other hand, wind turbines in wind farms can lose a noticeable portion of their energy production operating in the wake of upstream turbines. As a result, the aerodynamic interaction between wind turbines as well as their wake characteristics have become a field of significant interest in the design process of wind turbines as well as wind farms. Downstream wind turbine's performance is highly affected by the wake characteristics of the upstream turbines.

To get a better understanding of the complicated flow structure of the wake region behind a turbine, it is crucial to start from fundamental physics of the flow passing through the rotor of the wind turbines.

1.2.1 Actuator disk theory

The classical actuator disk theory describes the working principle of a wind turbine and helps to understand the physics of the flow field. A wind turbine rotor converts kinetic energy flux from the atmospheric flow to mechanical shaft power. So, fluid particles moving through the rotor disk lose a part of their kinetic energy. The incoming flow of a wind turbine rotor slows down gradually from its unobstructed value u to an average value u_w far downstream in the wake of the rotor. Meanwhile, the static pressure increases from its ambient value P_∞ to a value P_d^+ just before the disk and then suddenly drops to P_d^- after the disk. This pressure jump is due to the axial thrust force of the rotor. The pressure recovered gradually to its freestream value P_∞ . Figure 1-3 shows a schematic of one-dimensional flow through an actuator disk.

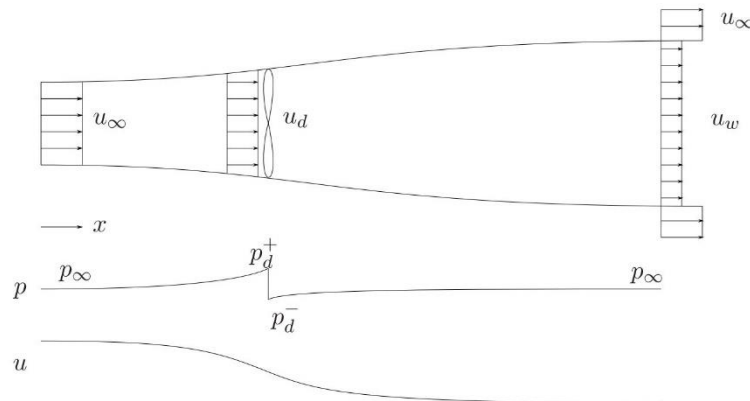


Figure 1-3 1D flow field through an actuator disk

Using equations of continuity, conservation momentum and conservation of energy (for incompressible flow) one can derive:

Conservation of mass:

$$\dot{m} = \rho A_{\infty} u_{\infty} = \rho A_d u_d = \rho A_w u_w \quad (1.1)$$

Conservation of momentum:

$$T = \dot{m} (u_{\infty} - u_w) = (P_d^+ - P_d^-) A_d \quad (1.2)$$

Conservation of energy:

$$E = \frac{1}{2} \dot{m} (u_{\infty}^2 - u_w^2) \quad (1.3)$$

Energy extracted per unit time, i.e., Power:

$$P = \frac{1}{2} \dot{m} (u_{\infty}^2 - u_w^2) \quad (1.4)$$

The extracted power is equal to the power performed by thrust T acting on the disk;

$$P = T u_d = \dot{m} (u_{\infty} - u_w) u_d \quad (1.5)$$

Which results in:

$$u_d = \frac{1}{2} (u_{\infty} + u_w) \quad (1.6)$$

The power is divided into the total kinetic energy flux of the free stream passing through the rotor disk to get the power coefficient for a wind turbine:

$$C_p = \frac{P}{P_0} = \frac{P}{\frac{1}{2}\rho u_\infty^3 A_d} = \frac{\frac{1}{4}\rho A_d (u_\infty + u_w)(u_\infty^2 - u_w^2)}{\frac{1}{2}\rho u_\infty^3 A_d} = 4a(1 - a)^2 \quad (1.7)$$

Where $(a = 1 - \frac{u_d}{u_\infty})$ is called the axial induction factor, the optimal C_p is found at $a = \frac{1}{3}$ which is $C_{p_{max}} = \frac{16}{27} \approx 0.59$ (*Betz limit*).

1.2.2 Rotational effects

The energy converter part of the wind turbine (i.e., rotor) usually involves some blades, that transform axial motion energy into rotational energy. The torque of the rotor is applied by the flow passing through it. Thus, a reaction torque should be acting on the flow, resulting in a rotational motion in the direction opposite to the rotor. This means in a flow passing a turbine rotor there exists a tangential velocity component which is neglected in the actuator disk theory.

1.2.3 Vorticity based description of the flow through a turbine rotor

To discuss the vortex system of a turbine rotor, it is beneficial to first consider flow over a stationary finite blade with the bound vortex and tip vortices forming a horseshoe vortex. *Kelvin's* Theorem states that for an inviscid and incompressible flow, the material derivative of circulation is equal to zero ($\frac{D\Gamma}{Dt} = 0$). Therefore, there is a vortex with equal strength and rotating in the opposite direction to the bound vortex far downstream (named as *starting vortex* which is formed as the flow over the wing started) [8].

It is similar regarding a wind turbine but, the mentioned vortex system is rotating. Figure 1-4 shows a schematic of vortex system for a rotating turbine with three blades. The root vortex at the hub is formed by the combination of tip vortices shed from each rotor blade [9]. The tangential velocity at the rotor plane which has a direction opposite to that of the rotor is caused by the root vortex. This tangential velocity causes the tip

vortices to follow a helical path. If the number of blades is high, the tip vortices are close to each other, which leads to the concept of a tubular vortex sheet[10].

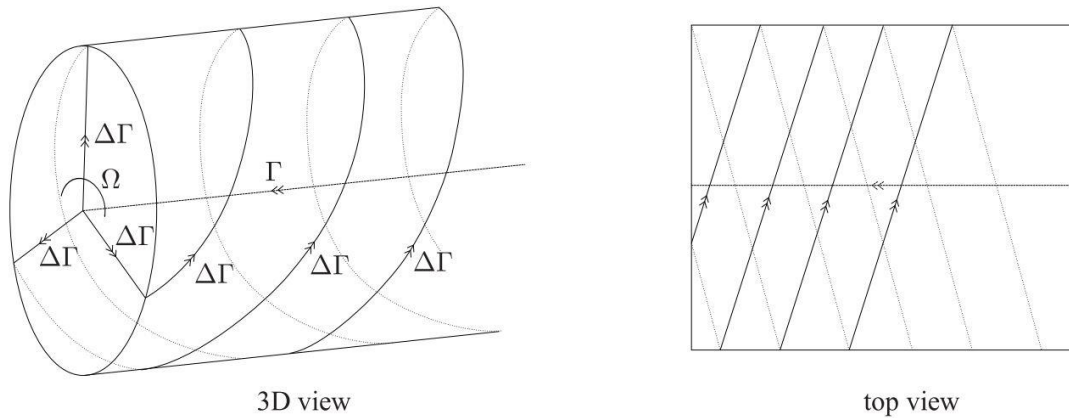


Figure 1-4 Vortex system on a rotating turbine with three blades [9]

1.2.4 Wake of a wind turbine

Downstream region of a wind turbine rotor is divided into near wake and far wake. The near wake is usually considered from the rotor up to 1 diameter downstream, where the shape of the flow field is determined by the geometry of the turbine that also determines the aerodynamic performance. In this region, high axial pressure gradients are observed developing the wake deficit. The far wake is the region in which the behavior of the velocity deficit profile is almost universal, and the rotor shape has less importance. The focus of the wake modeling and wake interactions in wind farms are on the far wake region. The velocity profile and vortex system downstream of a wind turbine rotor are not as simple as presented in previous sections. The velocity difference between inside and outside of the wake region causes a shear layer, which results in the velocity deficit recovery and meanwhile thickens moving downstream.

The shear layer consists of turbulent eddies which are distributed non-uniformly including tip vortices.

Figure 1-5 shows a more realistic schematic of the flow field downstream of a wind turbine rotor. The maximum velocity deficit is usually observed after about 1-2 rotor diameters (D). The wake continues to expand until some distance downstream where the wake is fully expanded. In the far wake region, the velocity deficit profile can be represented by an axisymmetric (because of atmospheric boundary layer) Gaussian distribution regardless of the geometry of the rotor blades. [9]

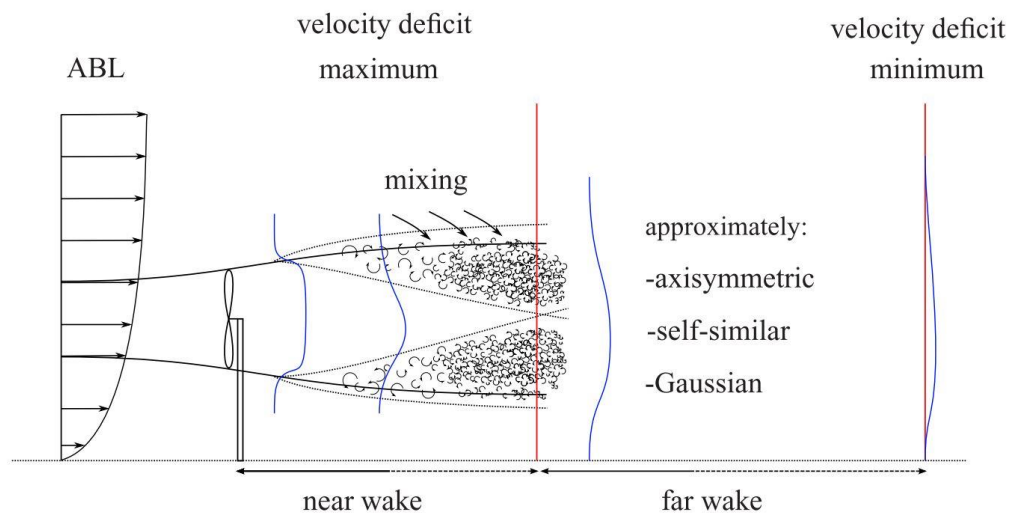


Figure 1-5 Flow field schematic downstream a turbine [9]

1.2.5 Wind farm Aerodynamics

The aerodynamic interaction of wind turbines in wind farms results in power losses and increased dynamic structural loads. Two most important factors influencing the total efficiency of a wind farm are the field geometry and the ambient turbulence. The former is the way in which the turbines are positioned. (i.e., the distance between individual turbines and the direction of arrays with respect to the mean wind direction). The latter influences the velocity deficit recovery in turbine wakes. The more the

ambient turbulence level, the velocity field recovers faster. For instance, for off-shore wind farms, the ambient turbulence is often lower than on-shore, resulting in more persistent wakes. The mechanical turbulence created by upstream turbines is also important. The wake of a downstream turbine recovers faster than the one in upstream, due to the higher turbulence levels in incoming flow.

Another important phenomenon in windfarm aerodynamics is the wake meandering. Wake meandering is known as the large-scale movement of the entire wake thought to be due to eddies that are larger compared to the size of the wake (large scale atmospheric structures)[9]. Effects of yawed inflow are also crucial regarding wind farm aerodynamics. Yawed incoming flow can cause a periodic change in power as well as structural loads which could lead to fatigue. A previous study [11] shows that a yawed turbine deflects the wake to the side which can be a potential method to control the wake direction and hence increase the wind farm efficiency.

1.3 Literature Survey on Winglets for Wind Turbines

This subsection is divided into two part. The first part contains literature survey on studies about the effects of blade tip devices on the power and thrust characteristics of the turbine. The second part includes previous studies on the effects of tip devices on the tip vortex behavior of the wind turbines.

1.3.1 Effects of winglets on wind turbine loads

Similar to airplanes, winglets in wind turbines decrease the induced drag of the blade by reducing the downwash effect in the tip region[12].

However, winglets also add excess profile drag (form drag) to the blades and the outcome of these two effects is important regarding having a positive or negative effect on the power production [13].

Numerical and experimental studies on the effects of winglets on the wind turbines' power and thrust performance show that properly designed winglets can have a positive effect on the power production of the wind turbines.

Johansen and Sorensen [14] investigated the effects of several winglet designs on the power performance of a modern wind turbine using computational fluid dynamics. The winglets have similar heights (1.5% of rotor radius) and cant angles (90°) but different airfoils and twist angles. Results showed that for different wind speeds, winglets had either positive or negative effect on the performance of the wind turbine. Two of the designs had positive effects for all wind speeds. The maximum increasing effect on the power performance was 1.67%.

Gaunna and Johansen [12] tried to determine the maximum achievable aerodynamic efficiency for wind turbine rotors with winglets using free wake lifting line method and CFD simulations. Results showed that winglets could be used successfully to increase power coefficient. Also, it was shown that the downwind winglets are more efficient than upwind ones of the same height.

Gertz et al. [15] experimentally investigated the effects of a designed set of winglets on a 3.3 m diameter model wind turbine. Results showed that winglets increased the power up to 6% over the central part of the operating range of the turbine while reducing it elsewhere.

Elfarrar et al. [16] designed an optimized winglet for NREL Phase VI wind turbine using CFD. The optimized winglet achieved around 9% increase in the power production.

Regarding wind farm applications, any possible increase in the power coefficient of “wingletted” turbines will lead to excess thrust coefficient which can affect the power production of downstream turbines in the negative direction [9]. There are not many research studies conducted on the effects of these devices on the turbines that are operating downstream. Tobin et al. [17] experimentally investigated the effects of

downwind winglets on the performance of two interacting model wind turbines with a rotor diameter of 0.12 m. Results for the “wingletted” turbine showed an increase in the power and thrust coefficient of 8.2% and 15.0%, respectively. Authors stated that a simple analytical treatment of obtained results showed a possible positive balance between the increasing power and thrust coefficients for a wind farm scale.

Shimizu et al. [18] and Abdulrahim et al. [19] have experimentally shown that Miervane type tip devices can also have positive effects on the power performance of wind turbines.

1.3.2 Effects of winglets on the tip vortex

Although it has been shown in the literature that the winglets have the potential to increase the power performance of turbines especially near design conditions, the effects on the tip vortex and wake characteristics are less clear. Most of the numerical and experimental studies on the tip vortex characteristics focus on wind turbines with no tip devices.

Laser sheet visualization (LSV) technique was used by Grant et al. [20] to picture the trajectories of the trailing vorticity under several conditions of turbine yaw and rotor azimuth with a rotor diameter of 0.9 m. Results were compared with a wake model highlighting the effects of wind tunnel walls that should be numerically represented in the wake model.

Xiao et al. [21] experimentally investigated the initiation and development of the tip vortex for a model HAWT using particle image velocimetry. Results showed that the tip vortex first moves inward for a very short period and then moves outward with the wake expansion. The downstream movement of the tip vortex was depicted to be nearly linear in the very near wake region.

Massouh and Dobrev [22] conducted an experimental study on the flow characteristics of the near wake of a model HAWT with a rotor diameter of 0.5 m. PIV region of interest contained vortex ages 0° to 810° showing that the vortex wandering motion increased significantly as the vortices aged downstream of the rotor. Moreover, it was concluded that the vortex characteristics such as vortex core diameter, the swirl velocity distribution and the vortex diffusion obtained from data were quite different from those obtained for model helicopter rotor.

Tobin et al. [17] conducted PIV measurements up to 5 D downstream a model turbine with and without winglets attached. Their experiments showed that the winglets did not significantly change the tip-vortex strength, suggesting that the aerodynamic improvements came from a downwind shift in the tip-vortex structure rather than diminishing its magnitude.

1.4 Objectives and Scope

The objective of this study consists of two main parts. In the first part, the effects of a designed set of winglets attached to the blades of a 0.94 m diameter three-bladed horizontal axis model wind turbine were investigated on its performance as well as on the performance of a similar turbine operating downstream. Design parameters of the winglets were selected in a manner to have a maximal increasing effect on the performance of the model wind turbine. The effect of a set of wing extensions of the same height as winglets is also investigated. Moreover, the effects of the distance in between two turbines were investigated with and without winglets or wing extensions attached to the upstream wind turbine.

The second part of this study focuses on the effects of winglets on the near wake flow around the tip region and the tip vortex characteristics within the wake. Phase-locked two-dimensional Particle Image Velocimetry (PIV) measurements are performed downstream of the model turbine, with and without winglets, following 120 degrees of azimuthal progression of the rotor. Details of the flow field are presented as phase-

locked and overall averages (i.e., averages of phase-locked data). The impact of using winglets on the tip vortex structure in terms of its downstream convection, vortex core size and core expansion characteristics as well as induced velocity field, vorticity and turbulent kinetic energy around the vortex core are presented in detail using the PIV data.

Chapter one contains motivation of the study, a brief qualitative description of wind turbine aerodynamics, a literature survey on winglets for wind turbines and, objectives and scope of the thesis. In chapter two, technical properties of experimental facilities used in this study, and measurement methods, are described in detail. In chapter three, the results are presented and discussed. Finally, in chapter four, the conclusions are summarized, and a brief future work suggestion is included.

CHAPTER 2

EXPERIMENTAL SETUP AND MEASUREMENT DETAILS

In this chapter, technical properties of experimental facilities used in this study, and measurement methods, are described in detail. In the first part, the properties of the two wind tunnels utilized for measurements are presented. The second part is about the technical specifications and aerodynamic behavior of the model horizontal axis wind turbines used in this study. In the third part, the design method of the winglets is described. Finally, the particle image velocimetry facility and PIV measurement details are presented.

2.1 Wind Tunnels

The first part of experiments was conducted in the closed loop large-scale wind tunnel at the department of energy and process technology of NTNU located in Trondheim, Norway. The second part of experiments was conducted in open jet wind tunnel of METU Center for wind energy located in Ankara, Turkey. Technical specifications of these wind tunnels are described below.

2.1.1 NTNU closed-loop wind tunnel

The test section of the NTNU closed-loop wind tunnel is 2.71m wide, 1.81m high and 11.15 m long. A 220 kW radial fan circulates the air inside the tunnel. The air speed could reach up to 30 m/s. A schematic of the wind tunnel is shown in Figure 2-1. Pitot-static tube with digital pressure transducers were used in the experiments to monitor the air flow speed at the inlet of the test section. This tunnel is equipped with a six-component force balance system attached to a turn table located in the middle of the test section. During the measurements, one of the model wind turbines was attached

to the balance in order to measure aerodynamic thrust force. Figure 2-2 shows a picture of NTNU closed-loop wind tunnel force balance system and a picture of the model horizontal axis wind turbine attached to the balance system turntable located at the middle of the test section. The measurements were conducted at free stream velocity of 11.5 m/s. Average turbulence intensity was 0.2 % at the inlet of the test section.

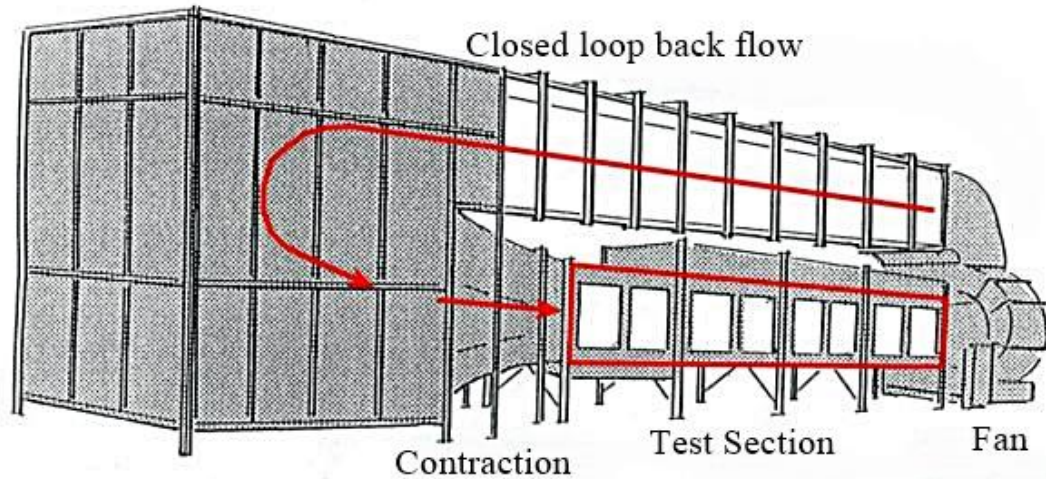


Figure 2-1 Schematic of NTNU closed-loop wind tunnel



Figure 2-2 (a) Picture of the NTNU closed loop wind tunnel balance system, (b) Picture of the model horizontal axis turbine attached to balance system located inside the NTNU wind tunnel test section

2.1.2 METWIND open jet wind tunnel

METUWIND open jet wind tunnel has a jet exit diameter of 1.7 m. The axial fan of the tunnel has a diameter of 1.25 m and is driven by a 45 KW variable speed control electric motor. A schematic of the wind tunnel is shown in Figure 2-3. After the fan, there exists a diffuser and a straight section before the exit which contains two screens and one honeycomb as flow straighteners.

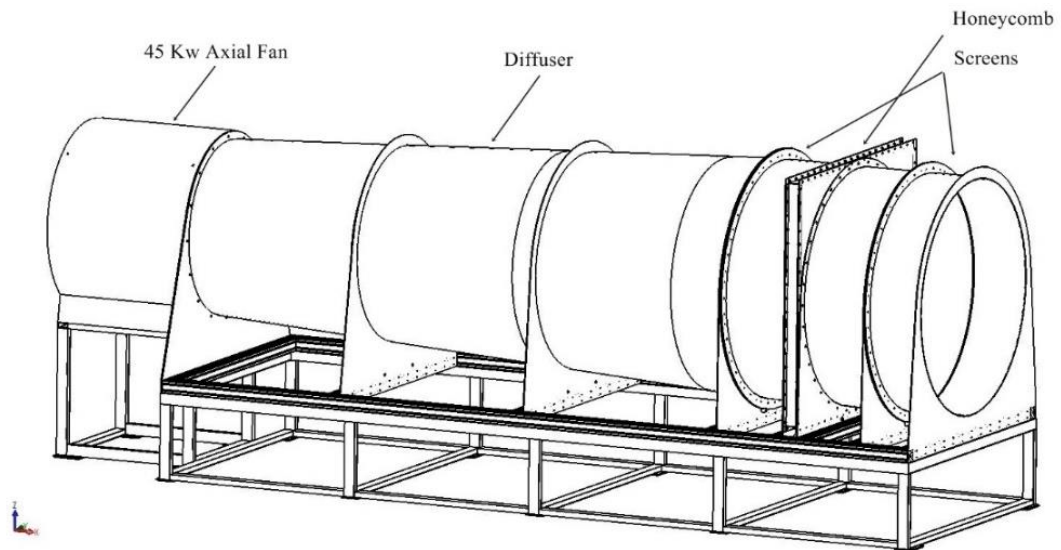


Figure 2-3 Schematic of the METUWIND open jet wind tunnel

The maximum speed at the exit of the tunnel can reach up to 12.5 m/s. To determine the usable area of the jet exit as well as aperture angle of the shear layer, hotwire measurements were conducted along radial direction at several downstream distances from the tunnel outlet. Figure 2-4 shows mean velocity (top row) and turbulence intensity (bottom row) for two different jet exit speeds of 5 m/s (left column) and 11.5 m/s (right column) at several downstream distances from the tunnel jet exit. D is the diameter of the model turbine rotor utilized in this study that is equal to 0.95 m. Two vertical dashed lines are showing the location of the boundary for the rotor of the model turbine (when its axis is aligned with tunnel center line) and the boundary of the tunnel exit. At $0.5D$ downstream location, for both 5 m/s and 11.5 m/s jet exit

velocities, mean velocity had an acceptable uniformity along radial direction up to approximately 800 mm from tunnel center line.

By moving downstream, the distance from the centerline in which the velocity distribution was uniform decreased due to the expansion of the mixing layer. In both jet exit velocities, turbulence intensity was measured about 2% at 0.5 D downstream of the jet exit from the tunnel centerline up to the rotor boundary. Turbulence intensity increased with downstream distance up to 6% at 4.5 D. To identify the potential core region at the jet exit of the tunnel, angular aperture of the mixing layer was calculated to be sure that wind turbines were located inside the potential core region.

Figure 2-5 shows a schematic of potential core and aperture angle of the shear layer at the jet exit of the tunnel for both 5 m/s and 11.5 m/s jet exit velocities.

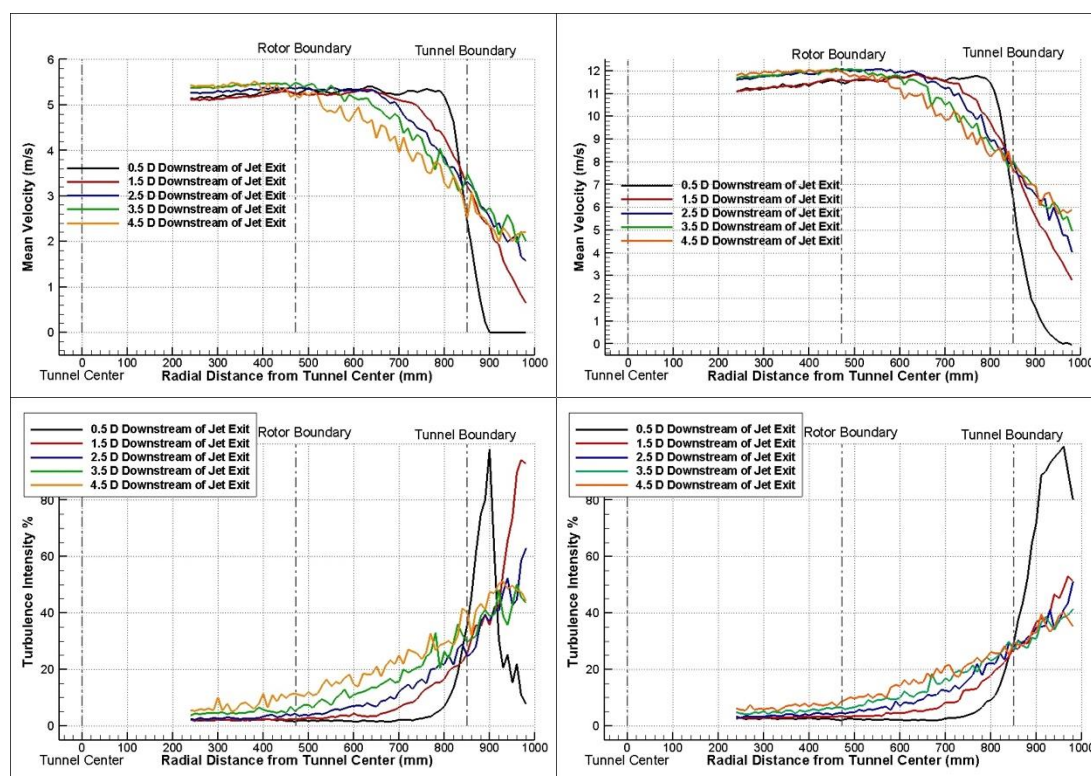


Figure 2-4 Hotwire measurements of mean velocity (top row) and turbulence intensity (bottom row) for two different jet exit speeds of 5 m/s (left column) and 11.5 m/s (right column) at several downstream distances from the tunnel jet exit.

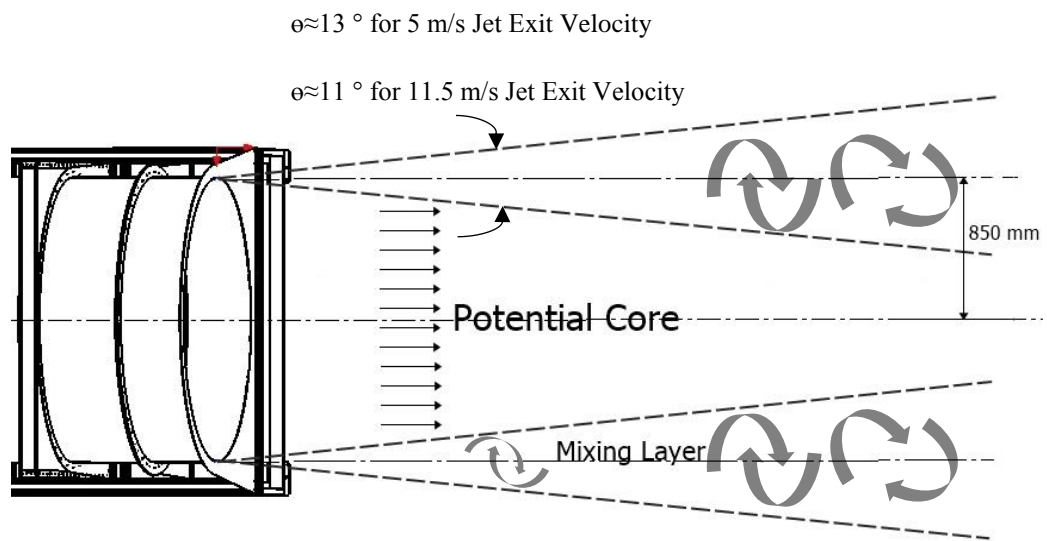


Figure 2-5 Angular aperture of the shear layer at the exit of METUWIND open jet wind tunnel.

2.2 Model Horizontal Axis Wind Turbines

Two similar model horizontal axis wind turbines were utilized in this study. The turbines have a diameter of 0.95 m. The rotors are three bladed and have NREL S826 airfoil profile twisted and tapered nonlinearly along the span. The blades taper and twist distributions are similar to the ones used in a series blind test wind tunnel campaigns [23–26] performed at the Norwegian University of Science and Technology (NTNU). Chord and twist distributions of the blades are shown in Table 2-1[23].

There is a transition region from airfoil cross-section to a circular cross-section between $r/R=0.15$ to $r/R=0.109$. The blades were mounted to a 0.13 m diameter hub.

Table 2-1 Spanwise chord and twist distribution of the rotor blades

r/R	c/R	α
0.016667	0.03	–
0.05	0.03	–
0.10889	0.03	–
0.12222	0.11	38
0.15	0.18096	37.055
0.18333	0.17802	32.544
0.21667	0.17114	28.677
0.25	0.1625	25.262
0.28333	0.15335	22.43
0.31667	0.14434	19.988
0.35	0.13578	18.034
0.38333	0.12782	16.349
0.41667	0.1205	14.663
0.45	0.11379	13.067
0.48333	0.10766	11.829
0.51667	0.10207	10.753
0.55	0.09696	9.8177
0.58333	0.092286	8.8827
0.61667	0.088002	7.9877
0.65	0.084068	7.2527
0.68333	0.080446	6.565
0.71667	0.077104	5.9187
0.75	0.074014	5.3045
0.78333	0.071149	4.7185
0.81667	0.068487	4.1316
0.85	0.066009	3.5439
0.88333	0.063697	2.9433
0.91667	0.061536	2.2185
0.95	0.059512	1.097
0.98333	0.057613	0.71674

Each turbine was equipped with one torque meter, and one electric servo motor to monitor power characteristics of the turbines for different tip speed ratios (TSR). A 3D CAD model of the wind turbine with a section view is shown in Figure 2-6.

It is important to note that the nacelle, hub and the blades of the model turbine were designed in detail to allow pressurized air injection from the blade tips while the rotor was rotating. For this aim, a pressure chamber was embedded in the nacelle that covers the hollow shaft and was sealed with rotating mechanical seals. The pressurized air

passed through the hollow shaft into the hub and consequently through the injection channel of the blades (which are embedded in blade geometry along the span) toward the tips. As this study was about winglets and there was no investigation on tip injection, the pressure chamber was disassembled from the nacelle, and the injection channel was closed from blade root using appropriate taping.

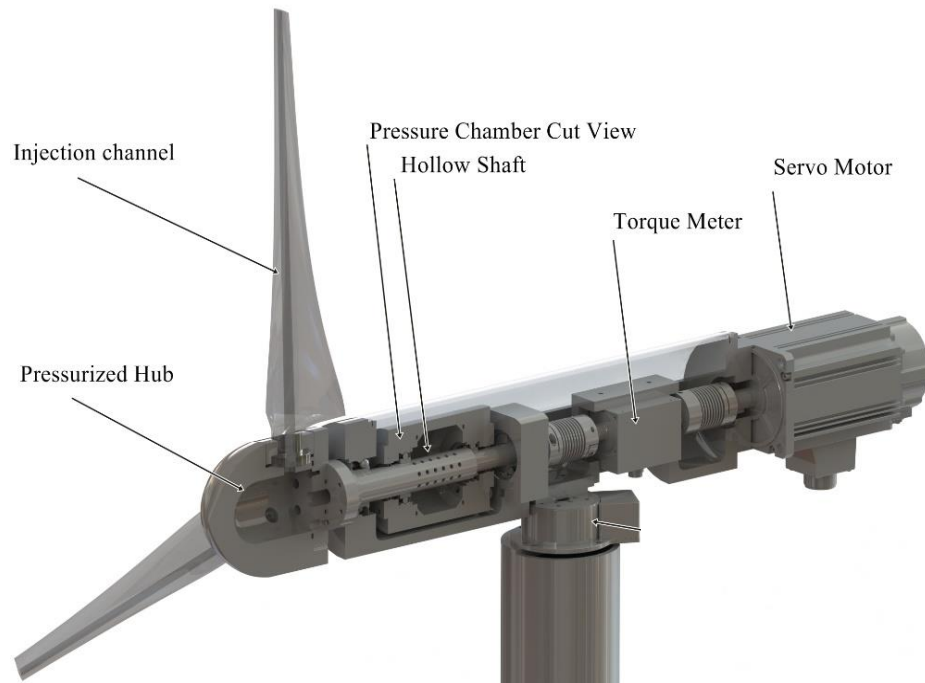


Figure 2-6 A 3D CAD model of the wind turbine

A LabVIEW code was developed to control the rotation speed of the turbines and to perform automated and synchronized data acquisition for given RPM lists. At each set of tip speed ratios, data acquisition from torque sensors was done for both turbines simultaneously. The code was monitoring the tunnel jet exit velocity using data from pressure transducers connected to a pitot-static tube located at $0.5D$ downstream of the tunnel jet exit. Figure 2-7 shows a screenshot of the front panel of the LabVIEW code.

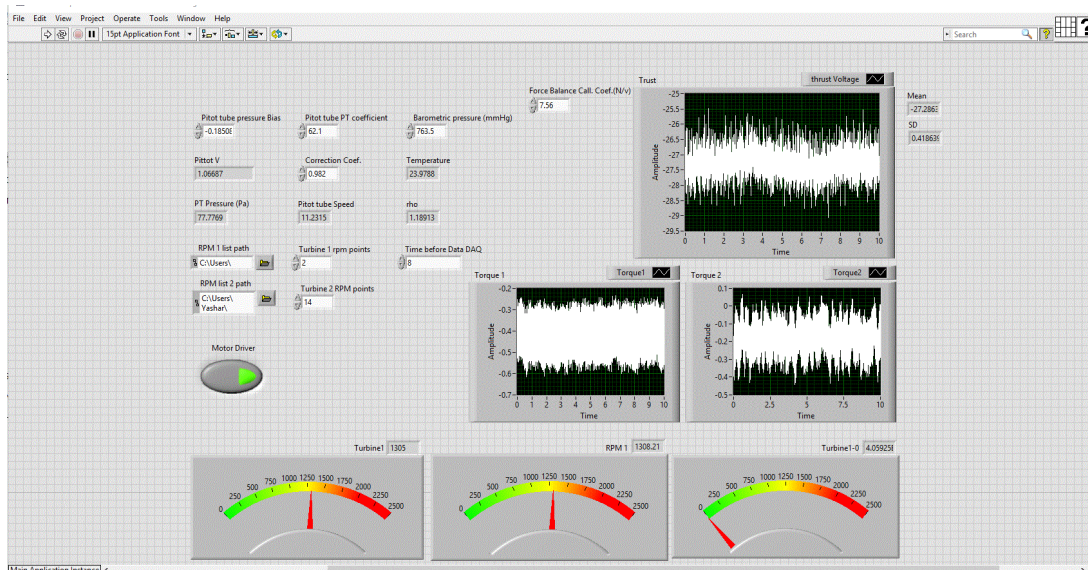


Figure 2-7 Front panel screen shot of the LabVIEW code to control rotation speed of both turbines and obtain simultaneous data from torque and thrust sensors. it also monitors the tunnel free stream speed

Two sets of rotor blades were used in the experiments. The first set of blades was manufactured by metal sintering (3D printing) technology from titanium material which have injection channel all along the span appropriate for tip injection. The other set was manufactured from aluminum alloy in CNC milling machine without injection channel.

All experiments through this study were conducted with zero pitch angle for the rotor blades. It was a challenge to adjust the zero pitch angles of the blades with good precision. For this aim, the camera of the PIV system was utilized. It was located below the turbine looking upward and focused to the tip of the blade positioned vertically on top of the camera. Figure 2-8 (a) shows a picture of the camera mounted below the turbine to monitor the tip of the blade. One side of the camera casing was aligned with rotor axis (nacelle casing) using a laser distance meter. As a result, the horizontal grid lines in the field of view of the camera were aligned with rotor axis, and vertical grid lines were parallel to the rotor turning plane which corresponded to the pitch angle equal to zero. Figure 2-8 shows screenshots of PIV Dynamic Studio software while performing manual pitch adjustment of aluminum and titanium blades.

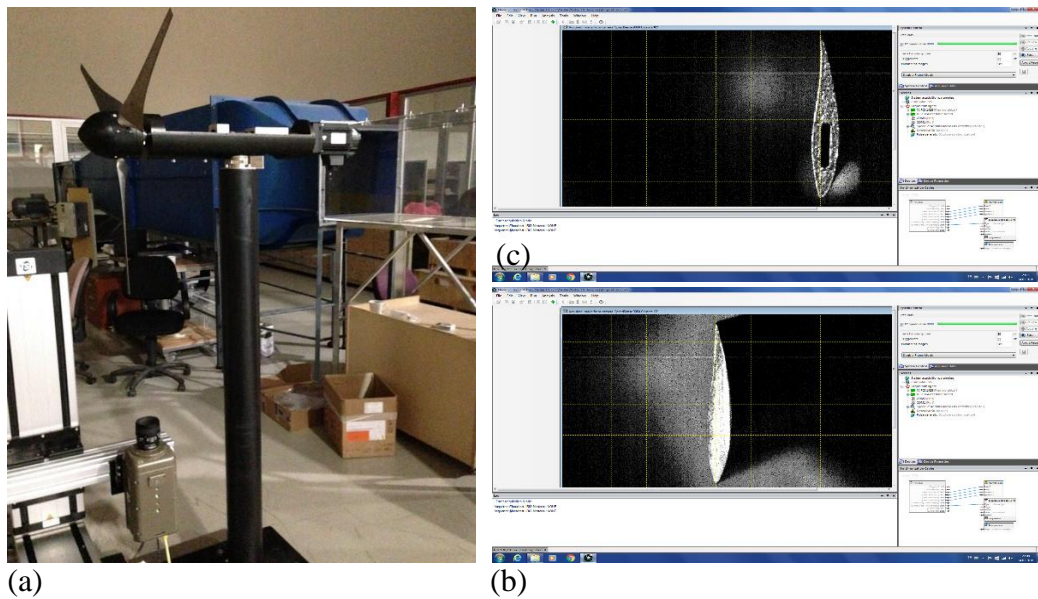


Figure 2-8 Picture of the camera of the PIV system mounted properly in order to adjust rotor blades' pitch angle (a). Screen shots of PIV Dynamic Studio software while performing aluminum (b) and titanium (c) blades' manual pitch adjustment.

Before starting the experiments with winglets, the performances of both aluminum and titanium rotors were measured at NTNU closed-loop wind tunnel at free stream velocity of 11.5 m/s presented in Figure 2-9. It was depicted that rotor with titanium blades had slightly higher C_P values compared to the rotor with aluminum blades. This difference in C_P curves could be due to differences in blade geometry and surface

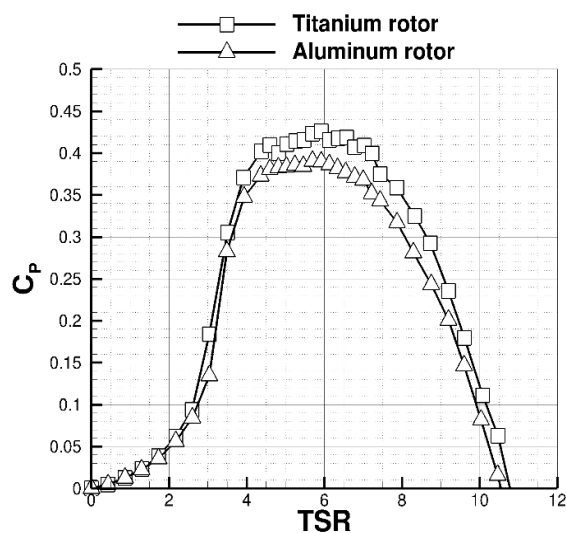


Figure 2-9 Titanium and aluminum rotors power coefficient measured at free stream velocity of 11.5 m/s.

roughness as the titanium blades were 3D printed whereas the aluminum blades were manufactured by milling technique. It is important to mention that throughout the experiments, the air channel of titanium blades was closed from the root side using appropriate taping.

2.3 Winglet Design

Winglets for wind turbines are mainly considered in two categories, upwind and downwind. The blade bends toward its pressure side for upwind winglet whereas it bends toward its suction side for downwind configuration. Upwind winglets are expected to contract the wake while the downwind winglets are supposed to cause the wake to expand [14].

For the current study, a set of downwind winglets was designed. Winglet profile was selected as PSU 94-097. This airfoil is designed by Maughmer et al. [27] for use on winglets for low-speed airplanes which was also suitable for our turbines regarding Re number. Cant, toe, twist and sweep angles were selected as 90° , 1° , -0.5° and 19° , respectively, defined in Figure 2-10. These angles were selected considering the behavior of the airfoil in the corresponding Re number at rotor TSR=6 and the chord length of the winglet at its root and tip. To estimate the lift and drag coefficients XFOIL analysis was performed. The toe and twist angles were selected properly to have the minimum drag coefficients in each section (root and tip). The winglet root chord length was selected to be equal to the blade tip chord. The height of the winglet was selected as 6% of the rotor radius.

Two sets of designed winglets were manufactured using 3D print technology. The first set was manufactured from plastic material and was used in NTNU wind tunnel experiments. The second set of winglets was manufactured from aluminum material and was used in METUWIND open jet wind tunnel experiments. Figure 2-11 shows pictures of the plastic and aluminum winglets attached to the rotor in NTNU and METUWIND wind tunnels.

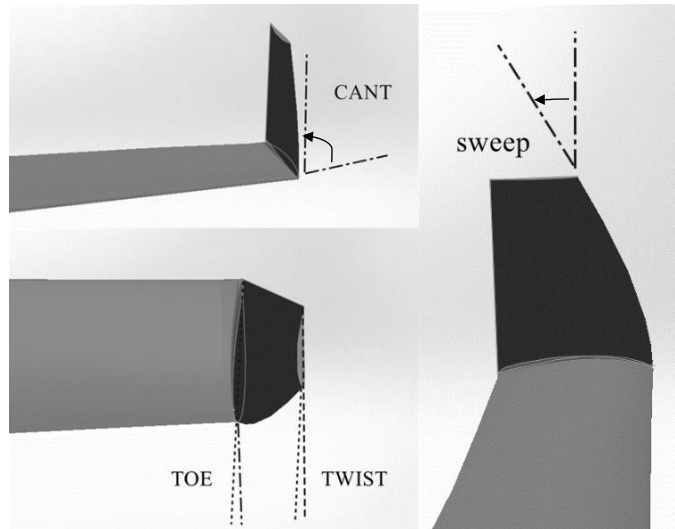


Figure 2-10 Definitions of winglet design variables



(a)

(b)

Figure 2-11 Picture of the winglets attached to the blades of the first turbine; (a) Plastic winglets at NTNU closed-loop wind tunnel, (b) Aluminum winglets at METUWIND open jet wind tunnel

2.4 Particle Image Velocimetry Measurements

PIV system consisted of a Nd:YAG laser (15 kHz and 120 mJ) and a Phantom v640 camera with a maximum resolution of 2560×1600 pixels at a frequency of 1.5 kHz (4 megapixels at full resolution). Proper optics were used to guide the laser beam to the hub height of the turbine and convert it to a laser sheet aligned with the free stream flow and passed through the central axis of the rotor. Figure 2-12 shows a picture of the test facility while performing Phase-locked PIV measurements at rotor phase 0° .

A hall-effect sensor attached to the turbine hub was sending a once-per-revolution signal to the synchronizer box. The laser and the camera could be triggered at predetermined azimuthal positions of the rotor by the involvement of proper trigger time delay from DANTEC DynamicStudio software. The experiments were conducted at 21 different azimuthal positions of the rotor from 0° to 120° phase angles with 6-degree intervals. Figure 2-13a shows the phase definitions and sample three phases. Phase 0° is defined as the azimuthal position in which the laser cuts the blade#1 tip from the mid-chord. The picture in Figure 2-12 captured at phase 0° .

PIV region of interest is shown in Figure 2-13b. It consisted of two identical measurement windows with an area of $228 \text{ mm} \times 141 \text{ mm}$. The overlap region of two windows was 10% that resulted in a total measurements area of $436 \text{ mm} \times 141 \text{ mm}$. Digital 3D traverse system was used to move the camera between two windows. To merge the data of two windows in the overlap region, inverse distance interpolation method was implemented.

The PIV measurements were conducted for the baseline and winglet cases resulting in a total number of 84 measurement windows. For each measurement window and for each phase, 1000 image pairs were recorded to obtain converged statistics. The images were processed utilizing cross-correlation method with interrogation area size of 64×64 pixels with 50% overlap resulted in a 2.88 mm vector spacing. Moving average validation was conducted on the vector maps before calculating the vector statistics. The time interval between two laser pulses was $25 \mu\text{s}$.

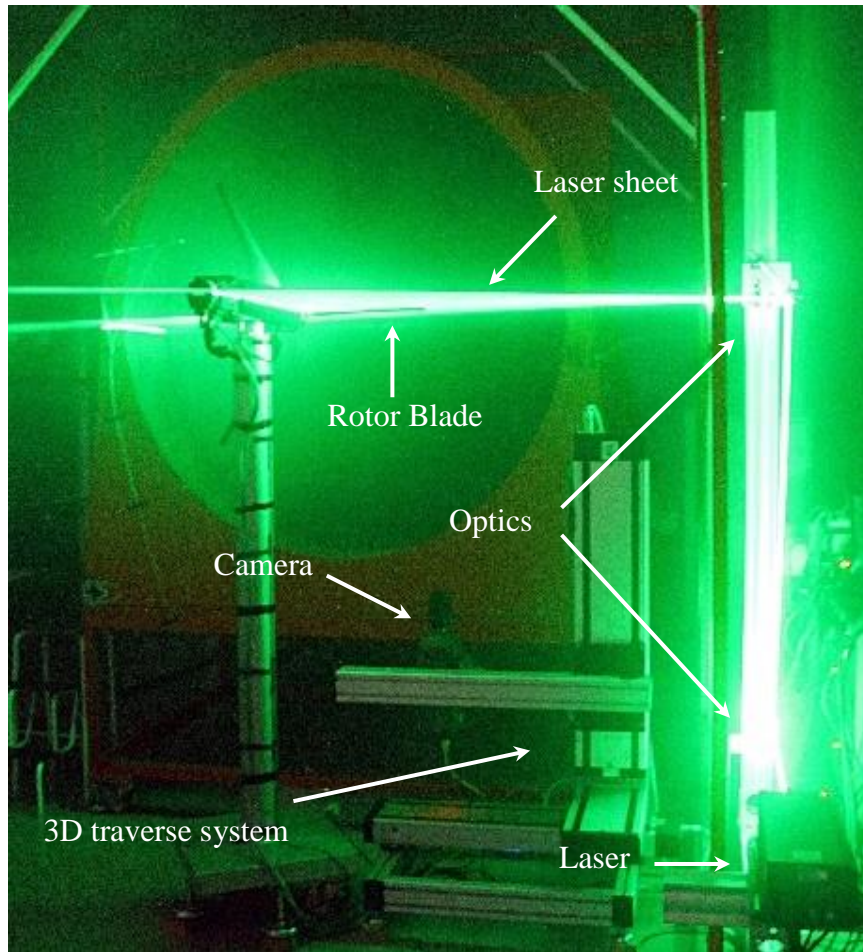


Figure 2-12 Picture of the facility while performing PIV measurements

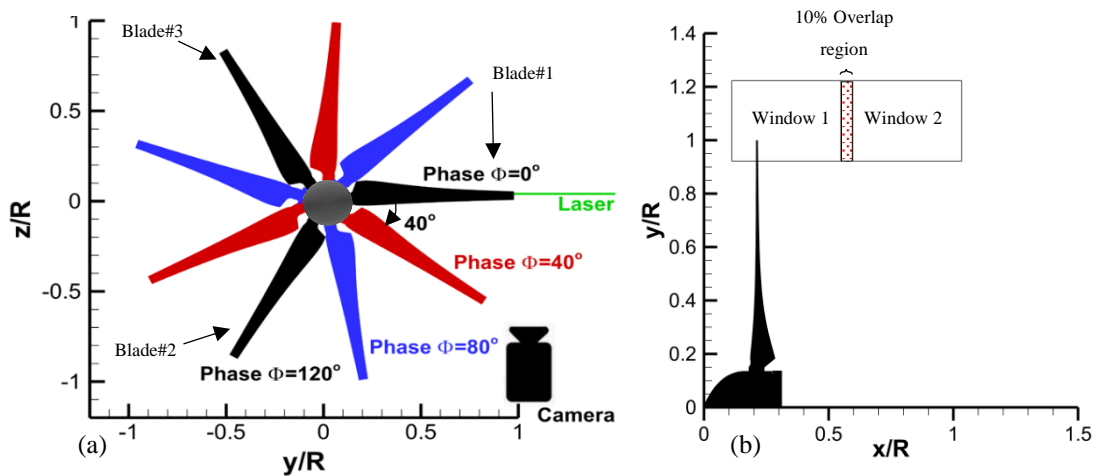


Figure 2-13(a) Phase definitions and sample three phases, (b) PIV domain

The flow was seeded using a fog generator located at the inlet of wind tunnel fan. The measurements were conducted at jet free stream velocity of 11.5 m/s while the turbine was rotating at 1348 rpm corresponding to $TSR \approx 6$, which is the design rpm of the rotor.

2.5 Instrumentation and Uncertainty

While performing the aerodynamic load measurements (C_P and C_T) of the model wind turbines, for each tip speed ratio, a sufficient number of samples are recorded for sampling period equal to one minute. Most of the required variables such as turbine rotation speed, the torque of the rotor, thrust value, ambient temperature and dynamic pressure of the tunnel, were measured simultaneously utilizing National Instrument data acquisition system and a LabVIEW code developed for this study. Each set of measurements was conducted twice regarding repeatability, and the results showed acceptable precision.

The open-jet wind tunnel velocity was measured using a Pitot-Static probe positioned $0.5D$ downstream of the tunnel jet exit. The Pitot-Static probe was operating through a Scanivalve DSA 3217 pressure scanner, which has an accuracy of 0.1%. For each measurement point, the ambient temperature was monitored using National Instrument K type thermocouple. The uncertainty value for the torque and rpm measurements are specified as 0.2% by the manufacturer.

If a parameter depends on several measured parameters it can be expressed as Equation 2.1:

$$P = f(x_1, x_2, \dots, x_n) \quad (2.1)$$

Now if the sensitivity of P to x_i , $\left(\frac{\partial P}{\partial x_i}\right)$ and the uncertainty of x_i , w_{x_i} is known, the uncertainty of P can be estimated as shown in Equation 2.2[28]:

$$w_P = \left[\sum \left(w_{x_i} \frac{\partial P}{\partial x_i} \right)^2 \right]^{1/2} \quad (2.2)$$

Using equation 2.2 the uncertainty in power coefficient values are estimated for the model turbine at free stream velocity of 11.5 m/s operating at design TSR value (TSR=6). The estimated uncertainty value is 1.1 %. Please note that the uncertainties of calculated air density and free stream velocity are estimated using the same method.

CHAPTER 3

RESULTS AND DISCUSSION

This chapter consists of two main parts. In the first part, the effects of the winglets on the power performance of two interacting model wind turbines are investigated and compared to the effects of wing extensions of the same height as winglets. In the second part, the results of PIV measurements of the effects of winglets on the tip vortex behavior of the individual wind turbine in the very near wake region is presented.

3.1 Effects of Winglets on the Performance of Two Interacting Model Wind Turbines and Comparison with Wing Extensions

Two sets of experiments were conducted to see the effects of winglets on the performance of two interacting model wind turbines. The first set of experiments were conducted at NTNU closed-loop wind tunnel using plastic winglets. In addition to power measurements, thrust measurements were performed utilizing six-component force balance system embedded below the test section floor of the wind tunnel. The second set of measurements on the power performance of two interacting wind turbines were conducted in METUWIND open jet wind tunnel utilizing aluminum winglets, and the results were compared to wing extensions of the same height as winglets.

3.1.1 NTNU closed-loop tunnel measurements

To see the effects of winglets on the aerodynamic performance of individual turbine, the turbine was mounted to the force balance system of the NTNU closed-loop wind tunnel. Power and thrust measurements were conducted with and without (referred as

the baseline) winglets attached to the blade tips at free stream velocity of 11.5 m/s. Results on the power and thrust coefficients are shown in Figure 3-1 and Figure 3-2, respectively. As depicted in Figure 3-1, winglets have a noticeable increasing effect on the power performance of the turbine for TSR values higher than 4. As shown in Figure 3-2, thrust measurement results have similar behavior for the same TSR values. For the turbine running at $TSR \approx 6$, power and thrust coefficients are increased about 4.2% and 6.5%, respectively.

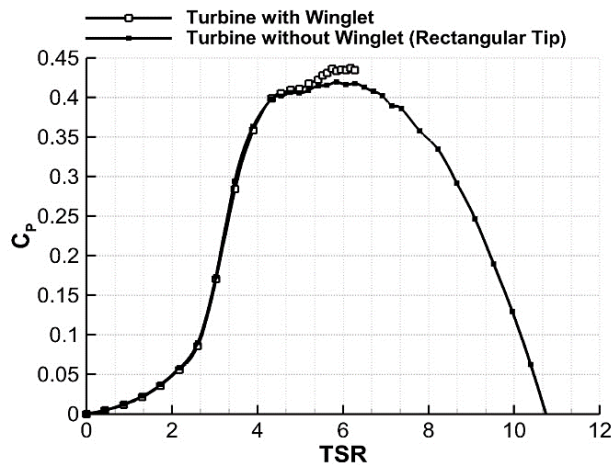


Figure 3-1 Power coefficient variations with TSR measured for upstream turbine with and without winglets at NTNU wind tunnel with freestream velocity of 11.5

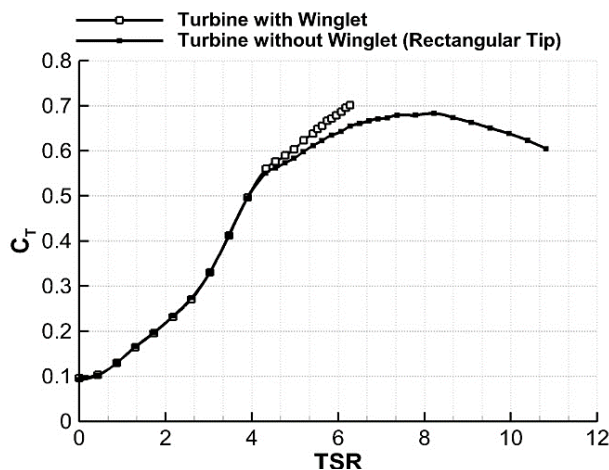


Figure 3-2 Thrust coefficient variations with TSR measured for upstream turbine with and without winglets at NTNU wind tunnel with freestream velocity of 11.5 m/s.

It should be noted that while the rotor was turning, the centrifugal force caused an outward deflection on the winglet tips (as the material for winglets used in NTNU wind tunnel was plastic). Because of this centrifugal force, the “wingletted” rotor was not turned higher than 1450 rpm (TSR≈6.25). The winglet outward deflection angle for TSR=6 (1350 rpm) was measured to be about 20° which caused a 4.4% increase in the rotor swept area. Power and thrust coefficients for the “wingletted” case is calculated taking this growth in rotor swept area into consideration.

Figure 3-3 shows the results of the downstream turbine’s power coefficient measurements located at three and six rotor diameters downstream of the first turbine while the upstream turbine is rotating at TSR=6 (design TSR) with and without winglets. It should be noted that in this study winglets were attached only to the first (upstream) turbine. The second (downstream) turbine was always operating with no tip devices. For both downstream locations, it is observed that the second turbine produced less power while operating downstream of the wingletted first turbine. As expected, the power coefficient is lower in the whole TSR range, which is a result of less incoming kinetic energy, while operating downstream of the wingletted turbine. Additionally, as seen in Figure 3-3, by increasing the distance in between turbines, the power production of the downstream turbine is increased.

Moreover, results show that the overall power efficiency of two turbines is increased for both three and six diameters distances in between turbines while the winglets were attached. Overall (wind farm) efficiency is defined as the ratio of the sum of measured power output from the two turbines to the sum of the maximum power obtained if they were both in an unobstructed environment (Equation 3.1). Table 3-1 presents the quantitative comparison of the overall efficiency of two turbines.

$$\eta_{overall} = \frac{C_{P1upstream} + C_{P2downstream}}{C_{P1max(unobstructed)} + C_{P2max(unobstructed)}} \quad (3.1)$$

Table 3-1 Overall efficiency of two turbines

Distance in between Turbines	Overall efficiency	
	Upstream Turbine without Winglets	Upstream Turbine with Winglets
	3 rotor diameters	65.6%
6 rotor diameters	69.9%	71.0%

Figure 3-4 shows the thrust coefficient variation with TSR for the second turbine at three rotor diameters downstream of the first turbine operating at TSR=6 with and without winglets. It should be noted that all power and thrust coefficients were calculated according to free stream velocity equal to 11.5 m/s.

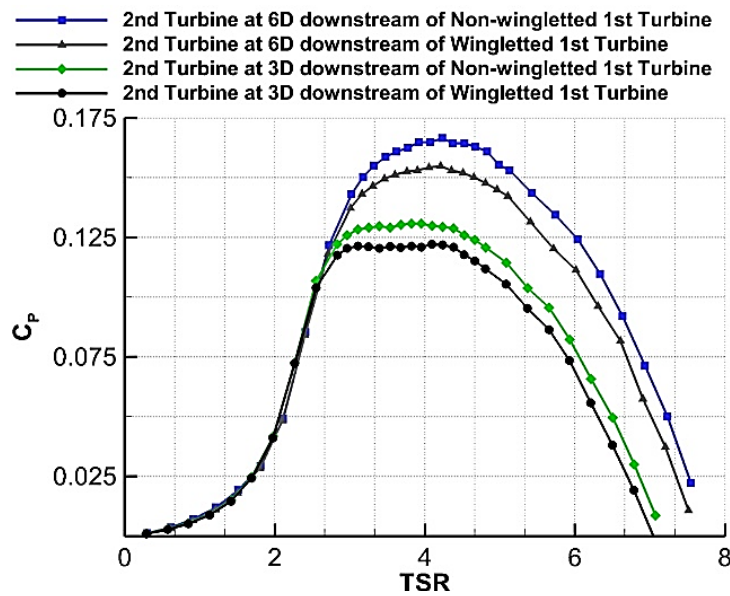


Figure 3-3 Power coefficient for downstream turbine with three and six rotor diameters distance in between while the upstream turbine is operating at TSR=6 (rotor design TSR) with and without winglets

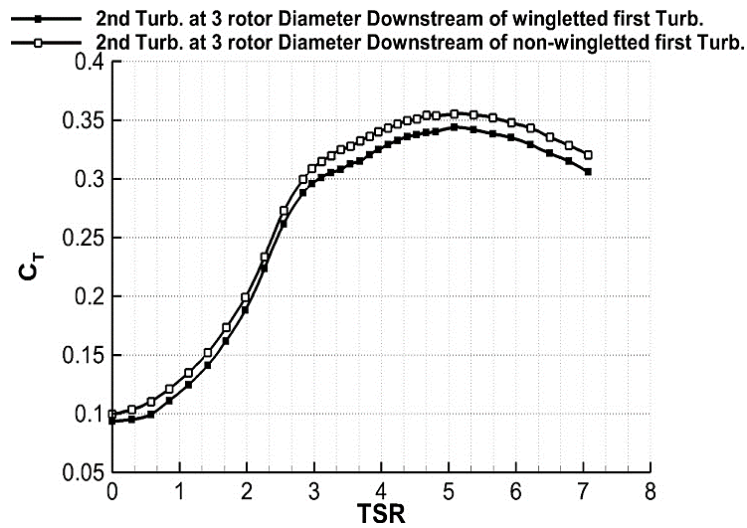


Figure 3-4 Thrust coefficient for downstream turbine with three rotor diameter distance in between while the upstream turbine is operating at $TSR=6$ with and without winglets (all coefficients are calculated according to free stream velocity equal to 11.5 m/s).

3.1.2 METUWIND open jet tunnel measurements

The second series of experiments were conducted in METUWIND open jet wind tunnel. Figure 3-5 shows the comparison between power coefficients of the individual turbine at free stream velocity of 11.5 m/s measured at closed loop wind tunnel of NTNU and open jet wind tunnel of METUWIND. The results of two measurements are quite consistent. However, around design TSR region ($TSR=6$), the turbine has a slightly higher power coefficient at the closed loop wind tunnel. Different blockage ratios in two wind tunnels (14.33% in NTNU and 30.6% in METUWIND), as well as different incoming flow turbulence intensities (0.2% in NTNU and 2% in METUWIND), can be possible reasons. One should note that the blockage ratio for METUWIND open jet tunnel was calculated for the area of the open jet exit. However, the turbine was located 0.5 D downstream of the jet exit, where the jet flow expands freely. Hence, the blockage effect for the open jet wind tunnel was lower, which can be a reason for less power production.

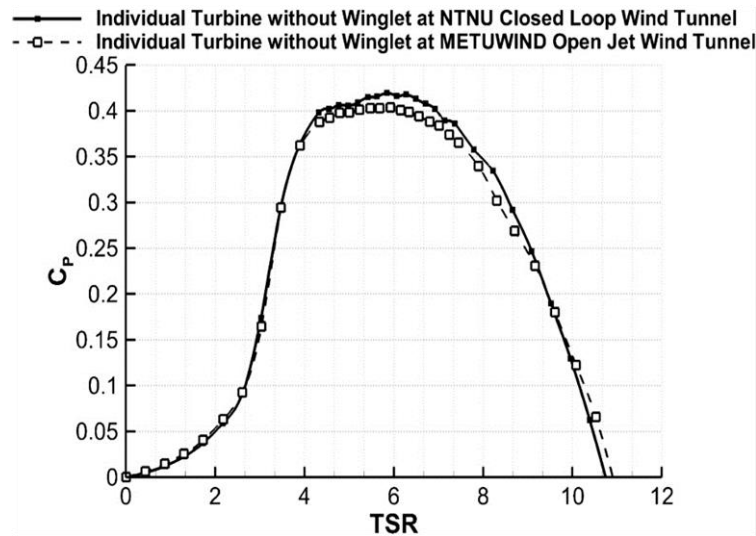


Figure 3-5 Individual turbine baseline (no tip devices) power performance comparison between measurements at NTNU closed loop and METUWIND open jet wind tunnels.

Figure 3-6 shows the power coefficient measurement results of the individual turbine with winglets attached compared to the baseline case (no tip devices). It is observed that winglets have a noticeable increasing effect on the power coefficient of the turbine around design TSR region (TSR=6) that is consistent with closed-loop wind tunnel measurements.

Please note that the winglets have adverse effects on the power performance of the turbine at TSRs higher than 6.7. Winglets decrease the induced drag of the blade by reducing the downwash effect in the tip region. Meanwhile, they add excess parasitic drag (friction plus pressure drag) to the blades, and the outcome of these two effects is important regarding having a positive or negative effect on the power production [14]. For our case, by increasing the tip speed of the rotor, the drag of the winglets exceeds the reduction in the induced drag of the blade, so the balance is negative. For tip-speed-ratios lower than TSR=5, as there is no change in power production, it seems that the decrease in induced drag and increase in parasitic drag balanced each other.

Figure 3-7 shows the effect of wing extensions (of the same height as winglets) on the power coefficient of the turbine. The power coefficient has similar values to the

baseline case. However, there is a small shift in the corresponding TSR values that is due to growth in radius because of wing extensions.

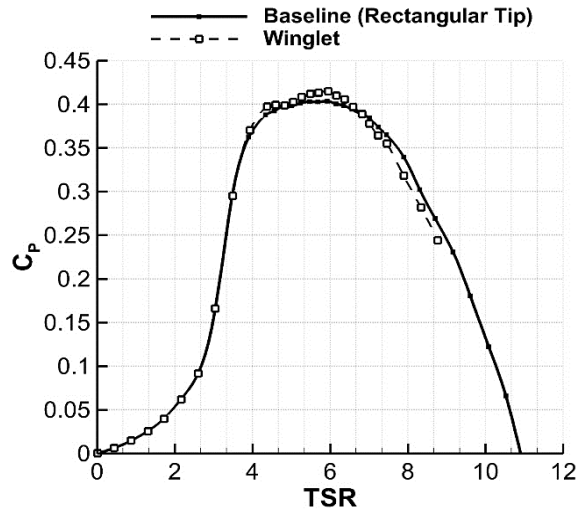


Figure 3-6 Power coefficient measurement results of first turbine with winglets

Please note that for each case (baseline and wing extension), power coefficient values are normalized due to rotor swept areas, so it is clear that the turbine with wing extension produces more power compared to the turbine with no tip device (baseline). This set of experiments were conducted utilizing winglets and wing extensions 3D printed from aluminum material, so contrary to NTNU experiments, it was possible to rotate the turbine at higher RPMs while the tip devices were attached, and there was no deflection in the winglets caused by centrifugal force.

Figure 3-8 shows the measured power coefficient for the downstream turbine with three rotor diameters distance in between while the upstream turbine was operating at TSR=6 (rotor design TSR) with no tip devices, with winglets, and with wing extensions. Please note that all power coefficients are normalized according to free stream velocity equal to 11.5 m/s. It is depicted that similar to what was observed in the first set of experiments, the downstream turbine has less power coefficient while operating in the wake of wingletted upstream turbine compared to the baseline case. For the case that the first turbine has wing extensions, the highest drop is observed in

the power performance of the downstream turbine. The upstream turbine with wing extensions extracted more power from the incoming flow. Hence, the velocity deficit in its wake region was higher, and consequently, there is less energy left for the downstream turbine.

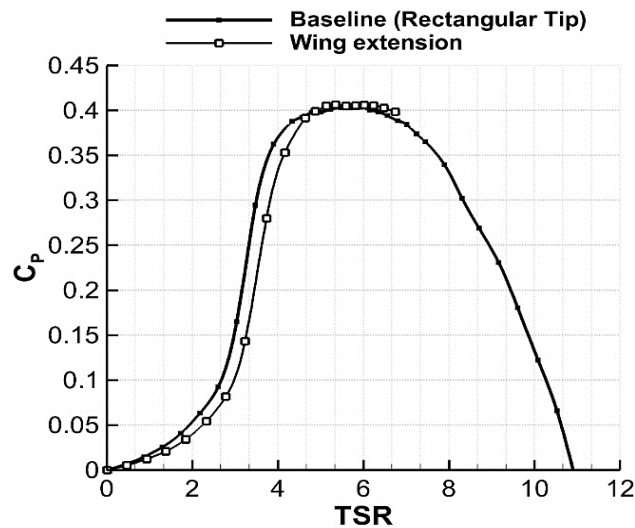


Figure 3-7 Power coefficient measurement results of first turbine with wing extensions

Table 3-2 presents the actual power production of the upstream turbine as well as the downstream turbine for all three cases. The upstream turbine's power production is increased about 3% while the winglets are attached compared to the baseline case. By attaching the wing extensions to the upstream turbine, its power production increased about 16%. However, this is due to increase in its rotor swept area by the same ratio (power coefficient remained the same as the baseline). Increase in the total power production of two turbines for the cases of winglets and wing extensions compared to the baseline case were about 1% and 9%, respectively. From these results, initially, it seemed that using wing extensions (in other words larger rotors) are more beneficial compared to winglets. However, there are always restrictions on increasing the turbines' rotor radius. Another remarkable point is that these results were for two turbines in line. Considering a higher number of turbines operating downstream of the first turbine, it is not beneficial to use wing extensions (larger rotors) for the upstream

turbine. However, using winglets may still be favorable regarding higher total power production as well as less structural loads.

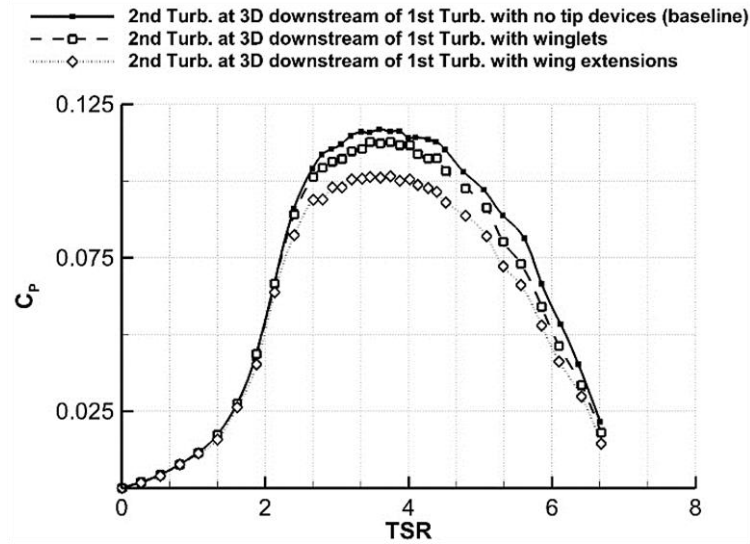


Figure 3-8 Power coefficient for downstream turbine with 3 rotor diameters distance in between while the upstream turbine is operating at TSR=6 (rotor design TSR) without any tip devices, with winglets, and with wing extensions (all coefficients are calculated according to free stream velocity equal to 11.5 m/s).

Table 3-2 Actual power production of turbines for all three cases

Power Production (watts)			
Upstream turbine without any tip devices			
		Upstream Turbine with Winglets	Upstream Turbine with Wing Extensions
Upstream turbine	214.1	219.76	250.74
Downstream turbine	63.07	60.46	53.16
Total	277.17	280.22	303.9

3.2 PIV Measurements of the Effects of Winglets on the Tip Vortex Behavior of the Model Wind Turbine

Particle image velocimetry measurements were performed to investigate the effects of the winglets on the tip vortex behavior of the model turbine in the very near wake region. In the first part of this section, the flow field characteristics near the tip are presented to understand the effects of winglets. In the second part, effects on the tip vortex characteristics are discussed. In the next part, effects of winglets on the induced drag are presented. Finally, the vortex meandering (wandering) motion is investigated in the last part of this section.

3.2.1 Flow field characteristics near the tip

In order to give an orientation for the reader before presenting all the PIV data, Figure 3-9a shows a sample PIV raw image superimposed by phase-averaged vortex-induced velocity vectors on window 1 (see Figure 2-13b) for the baseline case (i.e., no winglet) at rotor phase angle $\Phi=36^\circ$. Corresponding phase-averaged axial velocity \bar{u} and out-of-plane vorticity $\bar{\Omega}_z$ distributions are shown in Figure 3-9b and Figure 3-9c, respectively. The vortex-induced velocity vectors were obtained by subtracting average vortex core convection velocity values from the actual measured velocity components [29]. Vortex centers are defined as the points in which the vortex induced velocity vectors are zero, which very well coincide also with maximum out-of-plane vorticity locations. The free stream flow is from left to right. The dashed rectangular region represents the position of the blade at phase $\Phi=0^\circ$, and the point $\frac{x'}{R} = \frac{y'}{R} = 0$ represents the position of the blade tip at phase $\Phi=0^\circ$ (the blade is out of the field of view in the presented phase $\Phi=36^\circ$ in Figure 3-9). The tip vortices, their corresponding trajectories marking the wake boundary as well as their impact on the local velocity and vorticity fields can clearly be observed in Figure 3-9. As expected, the vortex rotation direction is from pressure side to the suction side of the blade, which generates a high negative out-of-plane vorticity component.

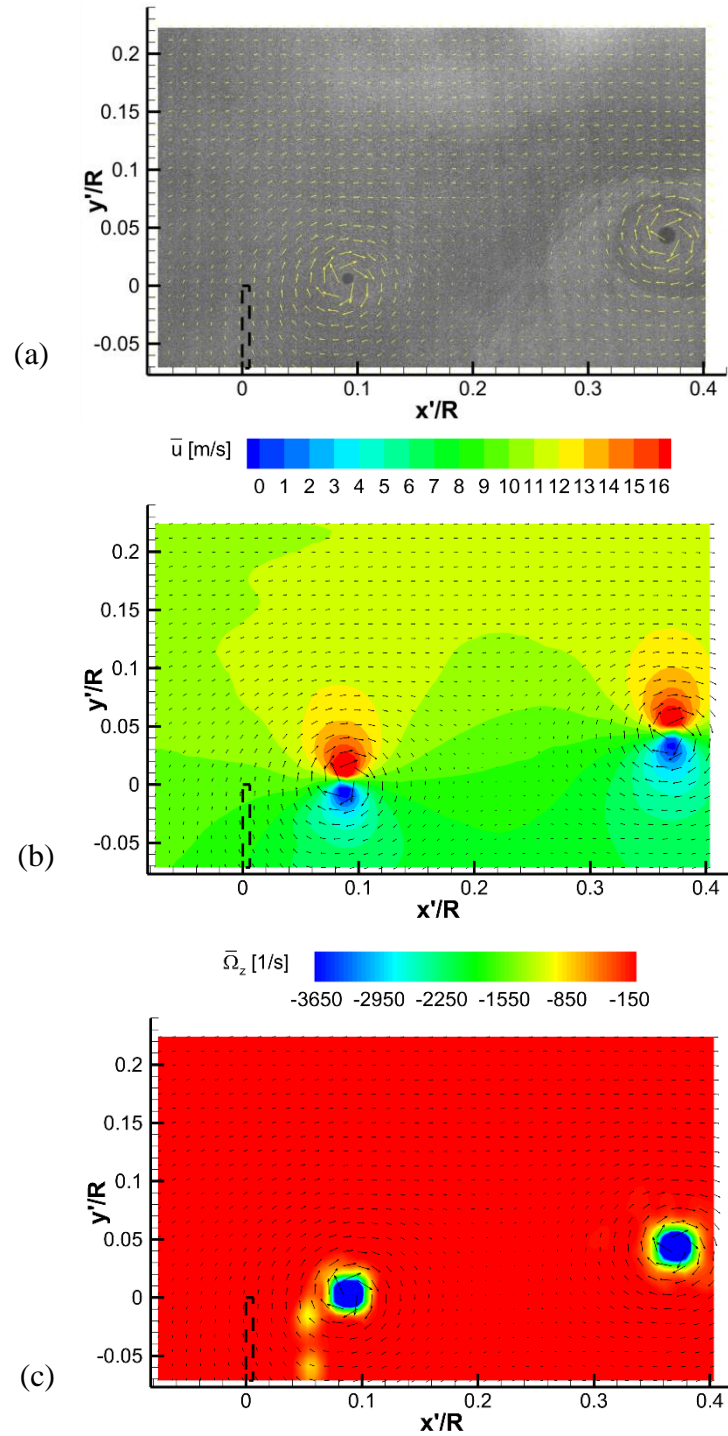


Figure 3-9 (a) A sample PIV raw image for the baseline case at phase angle $\Phi=36^\circ$, (b) and (c) corresponding phase averaged velocity \bar{u} and out-of-plane vorticity $\bar{\Omega}_z$ distributions near the blade tip, respectively, superimposed by vortex induced velocity vectors. The free stream flow is from left to right. The dashed rectangle represents the blade position at phase $\Phi=0^\circ$. Point $\frac{y'}{R} = \frac{x'}{R} = 0$ represents the position of the blade tip at phase $=0^\circ$.

As seen in Figure 3-9a, the vortex core does not perfectly match with the vortex induced velocity vectors. This is due to vortex wandering motion, as this figure shows a sample raw image, whereas the vortex induced velocity vectors are phase-averaged.

Figure 3-10, Figure 3-11 and Figure 3-12 show phase-averaged distributions of axial velocity (\bar{u}), out-of-plane vorticity ($\overline{\Omega_z}$) and turbulent kinetic energy (k) for 6 different phases of the rotor for the baseline (left) and winglet (right) cases. Here, the turbulent kinetic energy is calculated using the differences between phase-averaged and instantaneous measurements for each phase similar to [24]. Note that the original data set contains 21 phases of the rotor (every 6 degrees from 0° to 120°), but in Figure 3-10 to Figure 3-12, only 6 phases are presented to be concise (every 24-degrees from 0° to 120°). The blades cut the laser sheet plane only at phases $\Phi=0^\circ$ and $\Phi=120^\circ$ as marked by the white rectangular zones in the figures. In the winglet case a larger region is blocked due to the presence of the winglet.

The PIV data shows the creation and evolution of three distinct tip vortices within the measurement domain. As the phase angle increases, these vortices get convected downstream following and in fact constituting the expanding wake boundary. For example, in $\Phi=24^\circ$ in Figure 3-10 baseline case, the vortex on the left is shed from blade#1, the vortex in the middle is shed from blade#2, and the vortex on the right is shed from blade#3 (the blade numbering is shown in Figure 2-13a). In order to present a clear discussion regarding these vortices in the following sections we marked them as the first, the second and the third vortex, as shown in Figure 3-10, $\Phi=24^\circ$, baseline case. Note that the blade#1 and the blade#3 cut the laser sheet at $\Phi=0^\circ$ and $\Phi=120^\circ$, respectively.

To resolve the vortex characteristics, one should determine the vortex induced velocity vectors. The flow field can be assumed as a superposition of a background flow field that includes the convection velocity of the vortices, and a vortex induced flow field[29]. The velocity components of the background flow should be determined and subtracted from the original flow field. For this study, the center of the first vortex at

rotor phase 120° for the baseline case was identified using maximum vorticity method[22] in which the point with maximum vorticity is defined as the vortex core center. Then assuming that the vortex moved with a constant velocity[30] from blade tip at phase 0° to the determined coordinates at phase 120° , and knowing the time interval between these two phases, the average velocity components of the vortex core convection (\bar{u}_{core} , \bar{v}_{core}) were calculated. Then these values were subtracted from the velocity components of the original phase-averaged flow field for each phase to find the vortex induced velocity vectors. Vortex centers are defined as the points with zero vortex induced velocity vectors. Out-of-plane vorticity plots in Figure 3-11 are superimposed by vortex induced velocity vectors. In all Figures of this thesis with the vortex induced in-plane velocity vectors, only every third vector is shown in both directions with regard to visibility. As seen in Figure 3-11, there is acceptable coincidence between in-plane vortex induced velocity vector maps with vorticity distribution in terms of vortex core center locations.

Results from Figure 3-10 to Figure 3-12 show that for the baseline case in which there are no tip devices, there is a strong vortex shed from the blade tips. The implementation of the winglet creates significant modifications in the velocity, vorticity and turbulent kinetic energy fields as expected. As is evident from Figure 3-10, the axial velocity levels around the tip vortices, as well as velocity gradients, are substantially reduced when a winglet is present at the blade tips alluding to the creation of much weaker tip vortex structures within the wake. The downstream convection speed of the vortices, as well as the expansion of the wake boundary, also seem to be getting affected due to the change in the velocity fields. This point will be discussed in a more quantitative manner in the next section. Weakened tip vortices due to the presence of the winglets are also expected to cause an increase in power performance, which is consistent with the increase in the power production of the turbine near design TSR presented in the previous section.

The vorticity distributions presented in Figure 3-11 show that the vorticity levels within the vortex cores are also significantly reduced in the winglet case confirming

the weakening of the tip vortices. Vortex induced velocity vectors, also shown in Figure 3-11, coincide very well with the vortex centers. The results also show the existence of a double vortex shedding process that occurs near the tip when a winglet is present. One of these vortices gets shed from the corner where the pressure side meets the winglet, and the other gets shed from the tip of the winglet. These two distinct vortices can readily be seen in phase $\Phi=24^\circ$ in the vorticity contours in Figure 3-11 at $0.04 < \frac{x'}{R} < 0.12$. The one on the left is shed from the pressure side corner and larger in size compared to the one on the right that is shed from the tip of the winglet. However, the smaller winglet tip vortex has a slightly higher vorticity level around its center. These two vortices constitute a co-rotating asymmetric vortex pair, start rotating around each other and get merged at about $\frac{x'}{R}=0.4$, which is about 10 tip chords downstream from the rotor blade tip. This characteristic behavior of co-rotating vortices was also observed in previous fixed wing studies (e.g., Devenport et al. [31], Romeos et al. [32]). After merging they get convected as a single but distorted and non-uniform vortex structure, which is also clearly visible in phases $\Phi > 24^\circ$. The mutual interaction of these two vortices and resultant induced velocities on each other is generating a faster convection of the vortices along streamwise direction as well as a radially outward convection of the vortices causing a slight expansion of the vortex trajectories towards the freestream, hence a slightly wider wake boundary. More quantitative details will be given in the next section.

Turbulent kinetic energy distributions presented in Figure 3-12 show that though the levels near the vortex centers are reduced in the winglet case, wider areas are occupied around the vortices. This can clearly be seen for example at $\Phi=72^\circ$ and for the first vortex, wherein the winglet case the high turbulent kinetic energy region around the vortex seems to be approximately three times larger than that of the baseline case. This is most probably due to the mutual interaction of the double vortex structure shed from the blade tip for the winglet case. After the two vortices are merged, the wide region gets smaller, and a more uniform distribution can be observed around the vortices.

Figure 3-13 presents the overall average of all available 21 phases (0° to 120° with 6-degree intervals) for axial velocity (Figure 3-13a), out-of-plane vorticity (Figure 3-13b) and turbulent kinetic energy (Figure 3-13c) for baseline and winglet cases. In Figure 3-13, data masking due to the presence of blade at the camera field of view is done according to phase $\Phi=0^\circ$. The axial velocity distributions presented in Figure 3-13a clearly show the wake boundary and the expansion of the wake downstream of the turbine both for baseline and winglet cases. Near the wake boundary the lateral gradients (along y) of the axial velocity are very much reduced, and therefore in average, the wake boundary region looks much more diffused. Furthermore, the width of the wake boundary region is not as uniform in the case of the winglet, mainly due to the presence of the double vortex structure up to about $\frac{x'}{R} = 0.4$ and due to the distorted and non-uniform merged vortex structure after that point.

The vorticity distributions shown in Figure 3-13b also show a nice and uniform vorticity region along the wake boundary for the baseline case whereas in the winglet case significant streamwise and lateral non-uniformities are observed. Within the wake boundary centerline, which basically indicates the locus of vortex core center trajectories, the vorticity levels are substantially reduced compared to the no winglet case.

Overall average distributions of turbulent kinetic energy presented in Figure 3-13c illustrate a quite strange characteristic. For the baseline case and along the wake boundary centerline there seems to exist a gradual increase in k levels as one travels downstream. This is, of course, unexpected and this behavior could be due to increased tip vortex wandering (meandering) near the wake boundary further downstream from the rotor as also reported in [22]. The instantaneous meandering motion of the vortex contributes the velocity field fluctuations and gets reflected in the turbulent kinetic energy field if not appropriately filtered out. Keep in mind that the turbulent kinetic energy is calculated as the difference between phase-averaged and instantaneous vortex fields in this study and the amount of vortex meandering is expected to be observed in the turbulent kinetic energy distributions. The quantification of the amount

of vortex meandering is presented in the last section of the Results Chapter. Regarding the case with the winglet, within the very near wake region, $\frac{x'}{R} < 0.4$, the turbulent kinetic energy levels at the wake boundary are initially high, most probably due to the mutual interaction of the double vortex structure, then a quick decay is observed. However, similar to the baseline case, after the merging of the two vortices the overall averaged turbulent kinetic energy levels again start to steadily increase as one moves downstream.

In order to make more quantitative comparisons, Figure 3-14 presents extracted distributions of overall averaged axial velocity, vorticity and turbulent kinetic energy across the wake boundary at $\frac{x'}{R} = 0.8$. The distributions clearly show the effects of implementing a winglet, especially within the wake boundary region. Although similar wake and freestream levels are reached away from the wake boundary, i.e., below $\frac{y'}{R} < 0$ and above $\frac{y'}{R} > 0.2$, some of the previously discussed effects within the wake boundary are readily observable such as the reduction in the axial velocity gradient across the wake boundary, radially outward displacement of the wake boundary centerline and the reduction of vorticity and turbulent kinetic energy levels on the wake boundary centerline. The wake boundary seems to get pushed radially outwards about 30% compared to the baseline case. The magnitude of the out-of-plane vorticity and the turbulent kinetic energy levels are reduced about 26% and 60%, respectively, compared to the no winglet case. The reduction in the axial velocity gradient is about 33% within the wake boundary

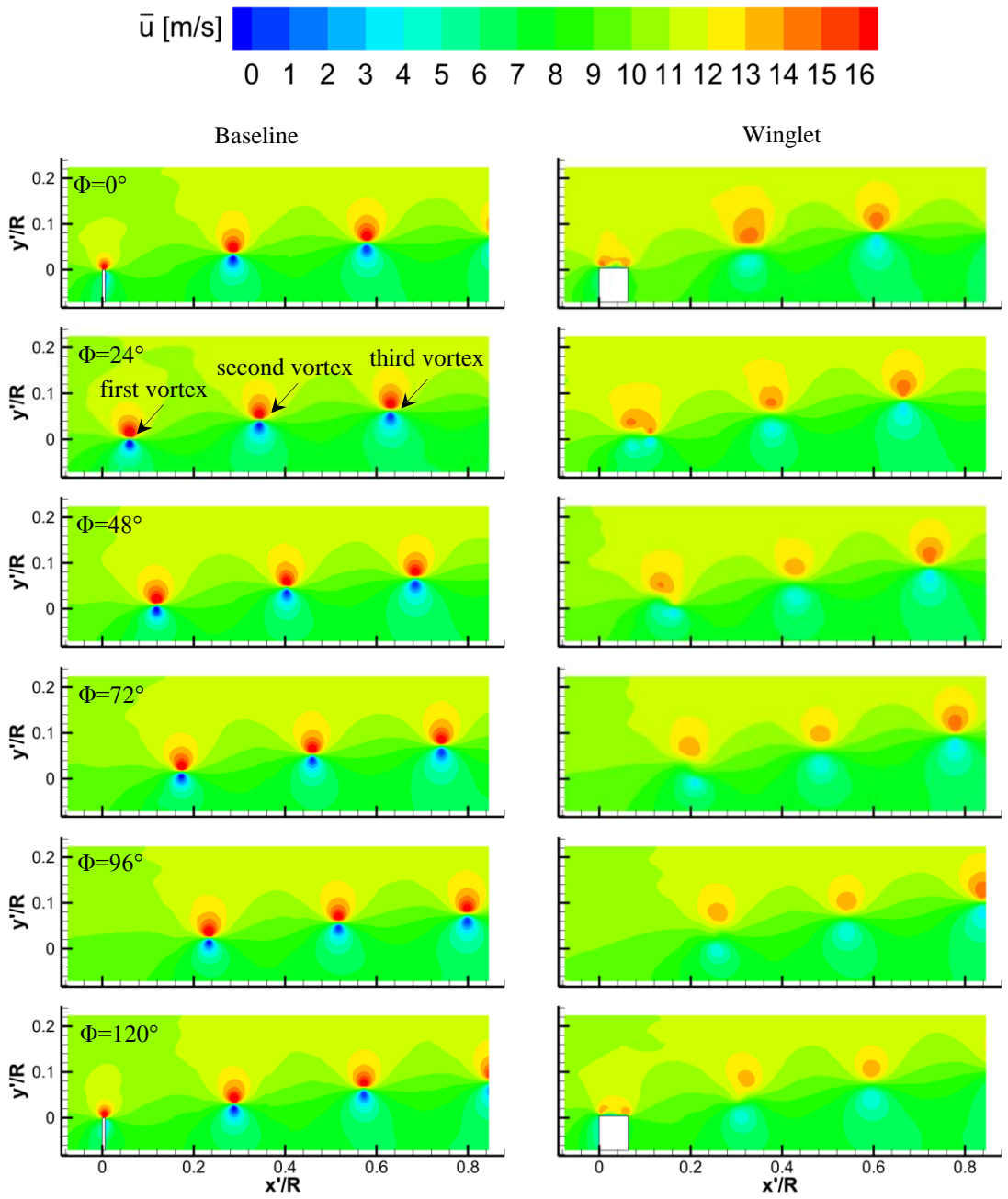


Figure 3-10 Phase-averaged distribution of axial velocity \bar{u} of rotor phases 0° to 120° for the baseline (left) and winglet (right) cases with 24-degree intervals.

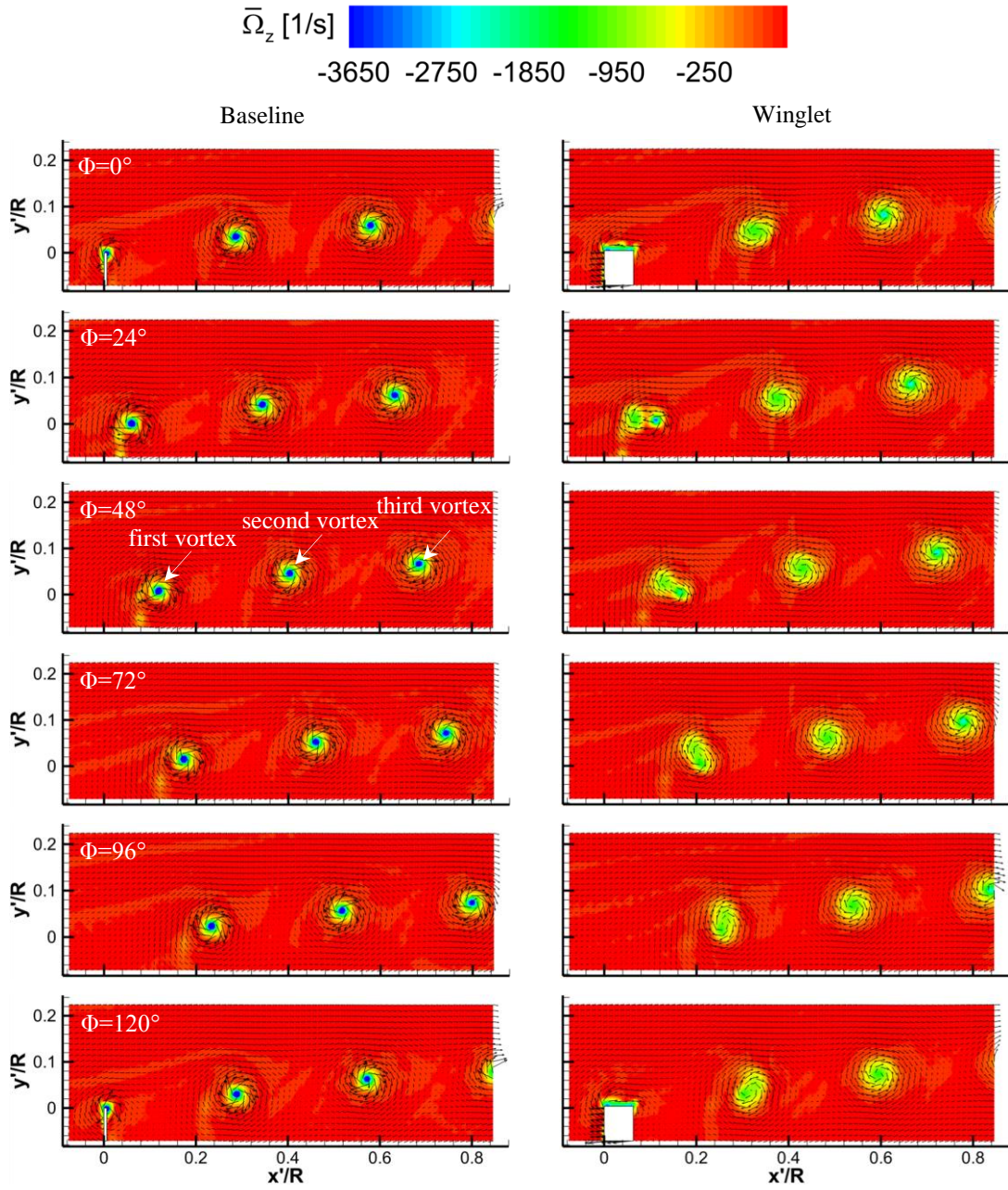


Figure 3-11 Phase-averaged distribution of out-of-plane vorticity ($\overline{\Omega_z}$) of rotor phases 0° to 120° for the baseline (left) and winglet (right) cases with 24-degree intervals.

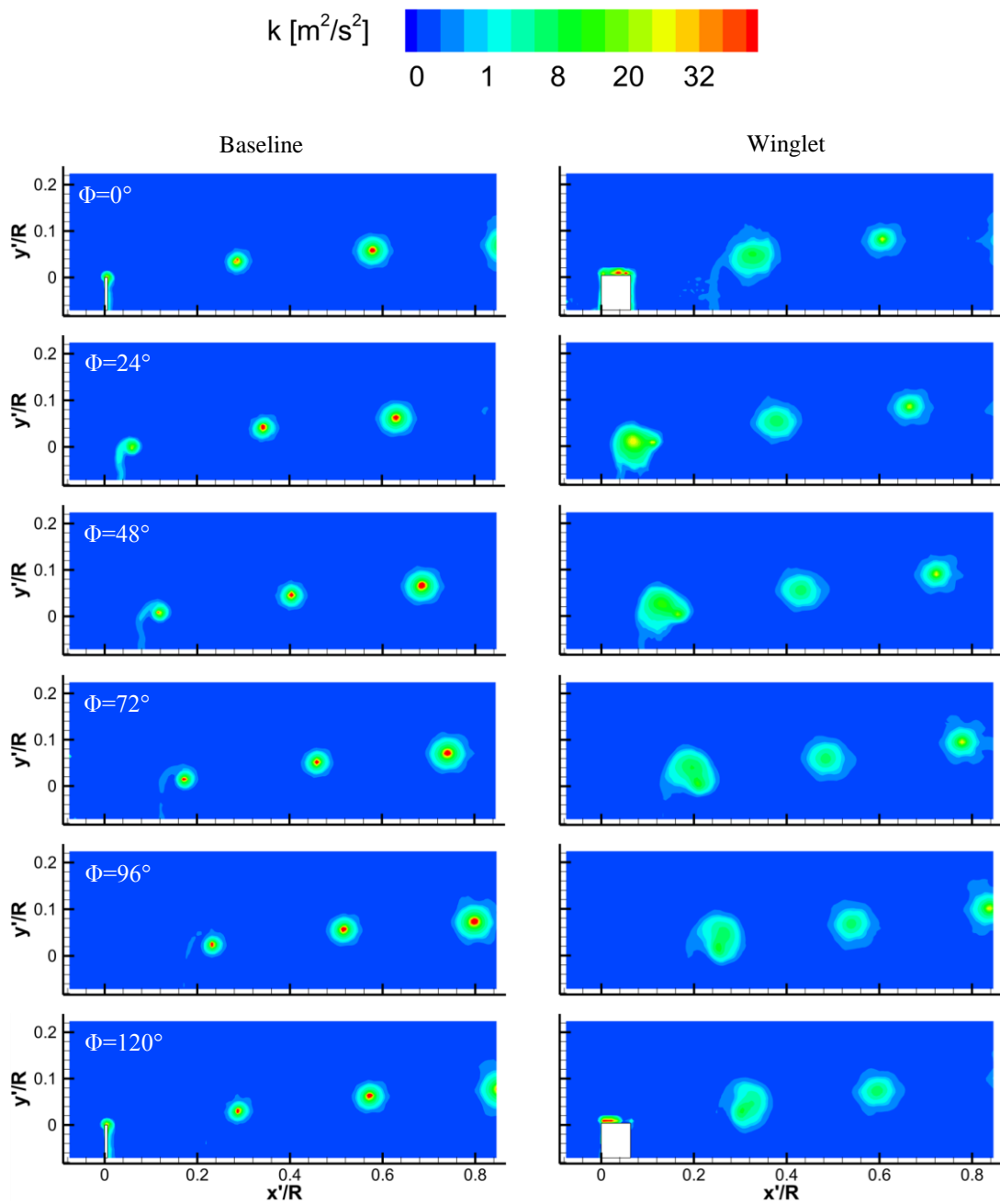


Figure 3-12 Turbulent kinetic energy distribution of rotor phases 0° to 120° for the baseline (left) and winglet (right) cases with 24-degree intervals.

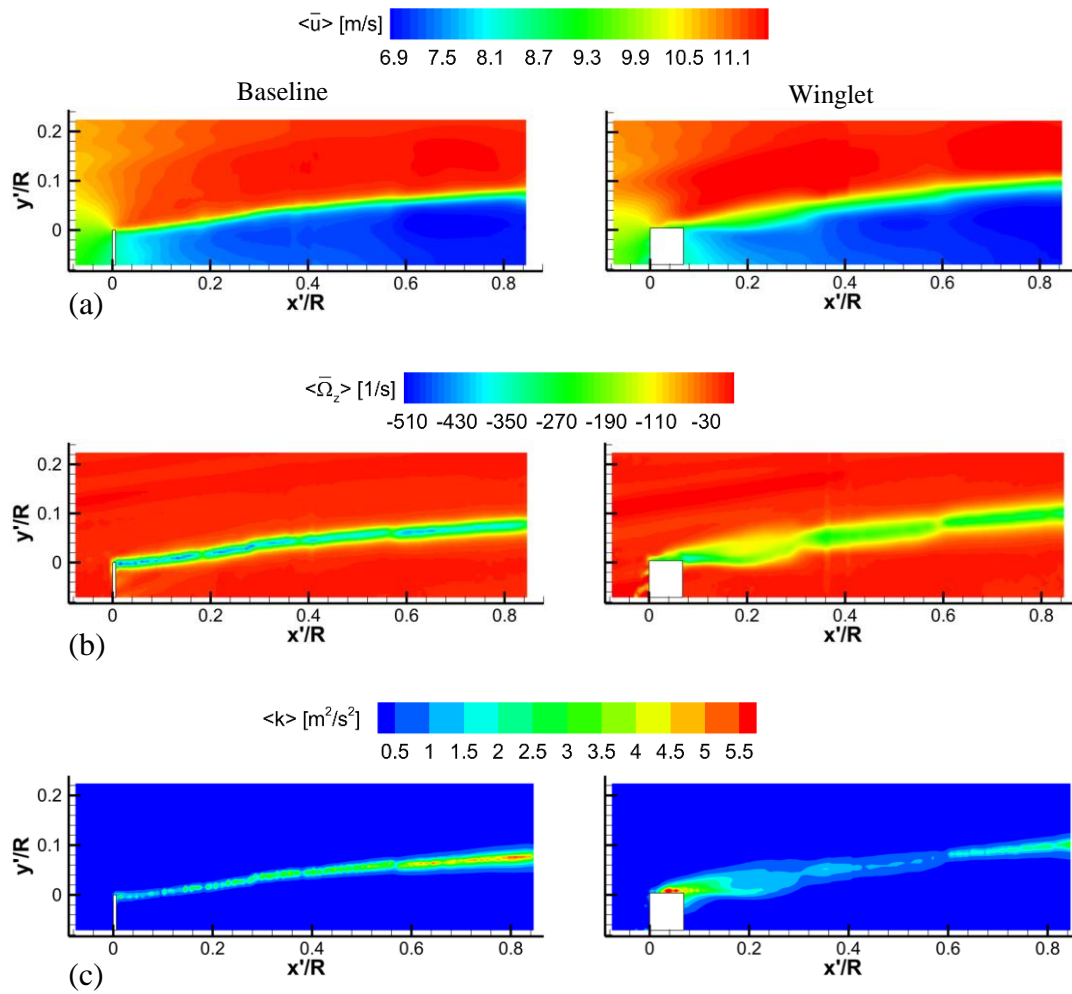


Figure 3-13 The overall average of 21 phases (0° to 120° with 6-degree intervals) for (a) phase-locked average axial velocity, (b) turbulent kinetic energy and (c) phase-locked average vorticity of each phase angle for baseline (left) and winglet cases (right).

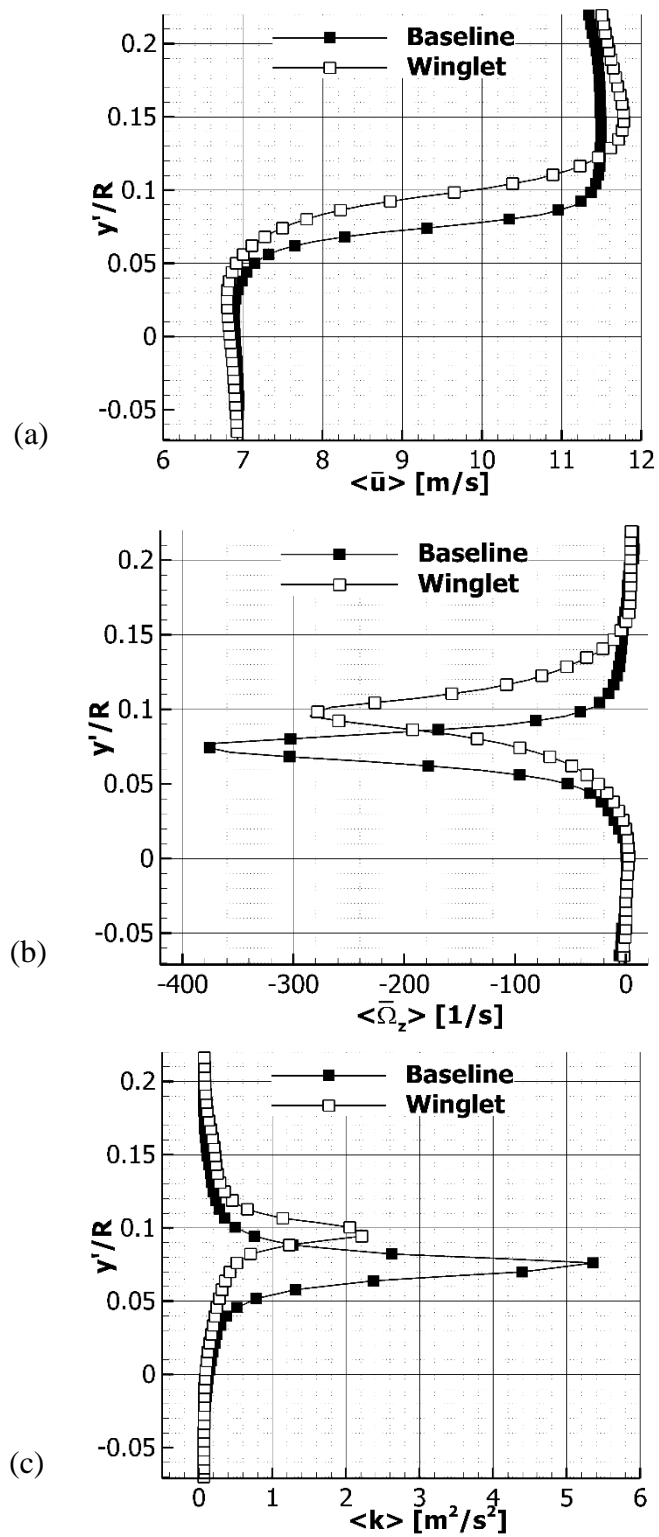


Figure 3-14 Data extracted from a vertical line at $\frac{y'}{R} = 0.8$ from the overall average of 21 phases (0° to 120° with 6-degree intervals) for (a) axial velocity, (b) out-of-plane vorticity and (c) turbulent kinetic energy for baseline and winglet cases.

3.2.2 Effects on tip vortex characteristics

Figure 3-15 shows vortex center positions from vortex age 30° to 330° with 30-degree intervals for the baseline and winglet cases. Vortex age is defined as the blade azimuth angle position after vortex release until the time of measurement. In these measurements, the age of the first vortex is equal to the defined rotor phase angle as the first vortex is shed at rotor phase 0° when blade#1 cuts the laser sheet. The age of the second vortex is equal to the rotor phase angle plus 120° (blade#2 cuts the PIV measurement plane 120° prior to blade#1). Similarly, the age of the third vortex is equal to the rotor phase angle plus 240°. For example, when the rotor is at phase 30°, the first vortex is at age 30°, the second vortex is at age 150°, and consequently, the third vortex is at age 270° (i.e., the rotor has rotated 270° since the formation of the third vortex).

The vortex center coordinates are the locations with zero vortex induced velocity vectors. It can readily be seen that the tip vortices move further downstream and radially outward when a winglet is present at the blade tips. This downstream and radially outward displacement of the vortices for the winglet case is most probably due to the mutual inductance of the co-rotating vortex pair on each other. For example, at vortex age 330°, the tip vortex for the winglet case is about 4.5% further downstream and 30% further radially out compared to the baseline case (relative to the blade tip, $\frac{x'}{R} = \frac{y'}{R} = 0$). This shows that there is more expansion in the wake due to the winglets and this additional expansion is also consistent with literature as a behavior of downwind winglets in wind turbines [14].

Figure 3-16 presents a comparison of baseline and winglet cases for the vortex induced swirl (tangential) velocity magnitude, out-of-plane vorticity and turbulent kinetic energy distributions along a horizontal line intersecting the center of second vortex core at rotor phase 60° (vortex age 180°). The horizontal axis is the non-dimensional distance from the vortex core center normalized by the tip chord length of the rotor blade.

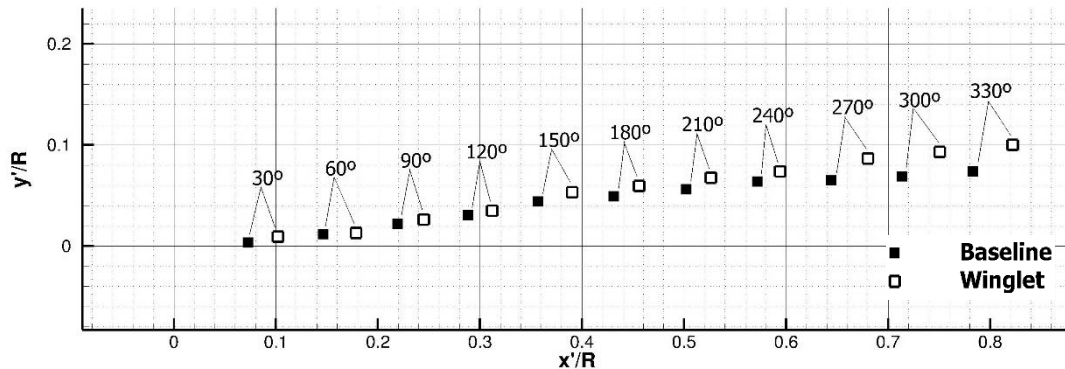


Figure 3-15 Vortex center positions from vortex age 30° to 330° with 30-degree intervals for the baseline and winglet cases.

For both baseline and winglet cases, the vortex induced swirl (tangential) velocity magnitude has a symmetric distribution with respect to the vortex core center as shown in Figure 3-16a. The vortex core diameter, which is estimated as the location of the maximum value for the induced velocity magnitude, is approximately three times larger when the winglets are used whereas the tangential velocity levels at the vortex core diameter are reduced about 50% for the winglet case. The ratio of vortex core diameter to the blade tip chord length is about 35% for vortex age 180° for the baseline case. By attaching the winglets, this ratio increases to 113%.

The vorticity levels within the vortex core are also substantially reduced for the winglet case, as shown in Figure 3-16b, such that the out-of-plane vorticity magnitude at the viscous core center for the winglet case is about 70% less than that of the baseline case. Note that the vorticity levels are spread to a larger area around the core due to the increase in the core diameter.

Figure 3-16c shows a significant reduction in turbulent kinetic energy levels around the vortex core such that the winglet case is about 80% less than that of the baseline case and again a slightly larger area is occupied when the winglet is implemented.

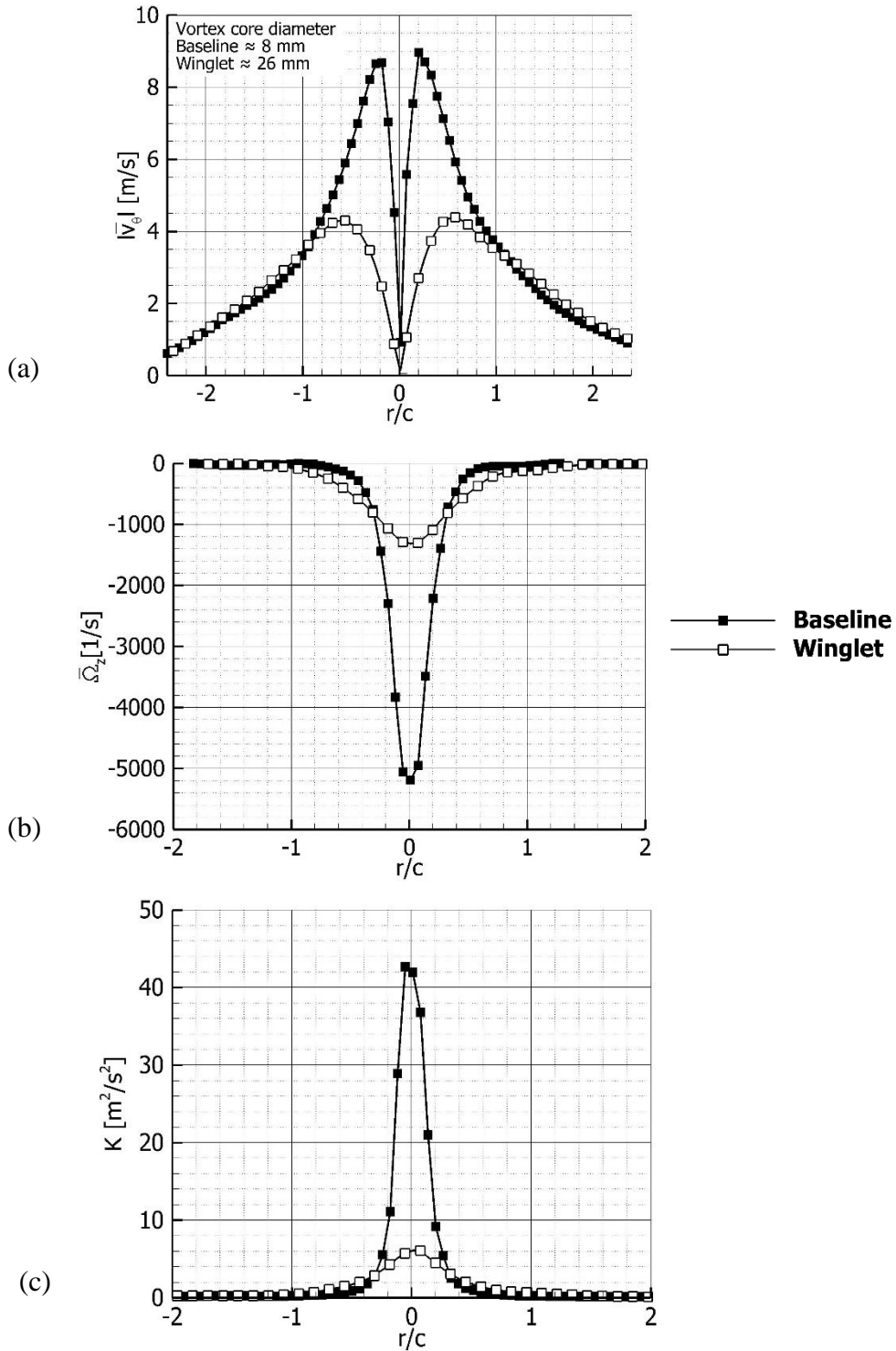


Figure 3-16 (a) Vortex induced swirl (tangential) velocity magnitude, (b) out-of-plane vorticity and (c) turbulent kinetic energy distributions along a horizontal line intersecting the center of second vortex core at rotor phase 60° (vortex age 180°). Horizontal axis is the non-dimensional distance from the vortex core center normalized by the tip chord length of the rotor blade, c .

Figure 3-17 presents a comparison of baseline and winglet data with various vortex core models including Rankine [33], Lamb-Oseen [34], Scully [35], original Vatistas [36] and simple Vatistas [37]. The equations for these models are also included here in Table 3-3 for completeness. The circulation and vortex core radius values that are needed by the models are obtained using the current experimental data.

Table 3-3 Vortex swirl velocity and core expansion models

$$\text{Rankine[33]} \quad V_{\theta}(r) = \begin{cases} \left(\frac{\Gamma_{\infty}}{2\pi r_c}\right) \left(\frac{r}{r_c}\right) & r \leq r_c \\ \left(\frac{\Gamma_{\infty}}{2\pi r_c}\right) \left(\frac{r_c}{r}\right) & r > r_c \end{cases} \quad (3.2)$$

$$\text{Lamb-Oseen[34]} \quad V_{\theta}(r) = \left(\frac{\Gamma_{\infty}}{2\pi r_c(r/r_c)}\right) (1 - e^{-1.2526(r/r_c)^2}) \quad (3.3)$$

$$\text{Scully[35]} \quad V_{\theta}(r) = \left(\frac{\Gamma_{\infty}}{2\pi r_c}\right) \frac{r/r_c}{1+(r/r_c)^2} \quad (3.4)$$

$$\text{Original Vatistas[36]} \quad V_{\theta}(r) = \left(\frac{\Gamma_{\infty}}{2\pi r_c}\right) \frac{r/r_c}{[1+(r/r_c)^{2n}]^{\frac{1}{n}}} \quad (3.5)$$

$$\text{Simple Vatistas[37]} \quad V_{\theta}(r)/V_{\theta_{max}} = r/r_c \left(\frac{\alpha+1}{\alpha+(r/r_c)^4}\right)^m, m = \frac{r/r_c+1}{4} \quad (3.6)$$

Vortex core expansion

$$r_c(t) = \sqrt{4\alpha\delta_v\nu(t + S_c)} \quad (3.7)$$

model (Sant et al.) [38]

Results presented in Figure 3-17a show that the maximum velocity levels at vortex core radius and subsequent decay are generally overpredicted by all models. The Rankine core model, which is the simplest model among the four, overpredicts the maximum swirl velocity up to 2.3 times. The closest results are obtained using the Scully model, which is, in fact, the same as Vatistas model with $n=1$. A further tuning of the Vatistas model with $n=0.85$ shows a significantly improved comparison with the experimental data. Simple Vatistas model with $\alpha=0.7$ also shows an acceptable agreement.

For the winglet case shown in Figure 3-17b, the Rankine, Lamb-Oseen, and Vatistas with $n=2$ models over predict the maximum swirl velocity at the vortex core radius same as what is seen for the baseline vortex but with less difference with the experimental data. Scully vortex model underpredicts the maximum swirl velocity for the winglet vortex, contrary to what is seen for the baseline case. Original Vatistas model with $n=1.15$ and simple Vatistas model with $\alpha=1$ show the best fit with experimental data. The coefficient values that result in the best fit with experimental data for original and simple Vatistas models are included in Table 3-4 for both baseline and winglet cases

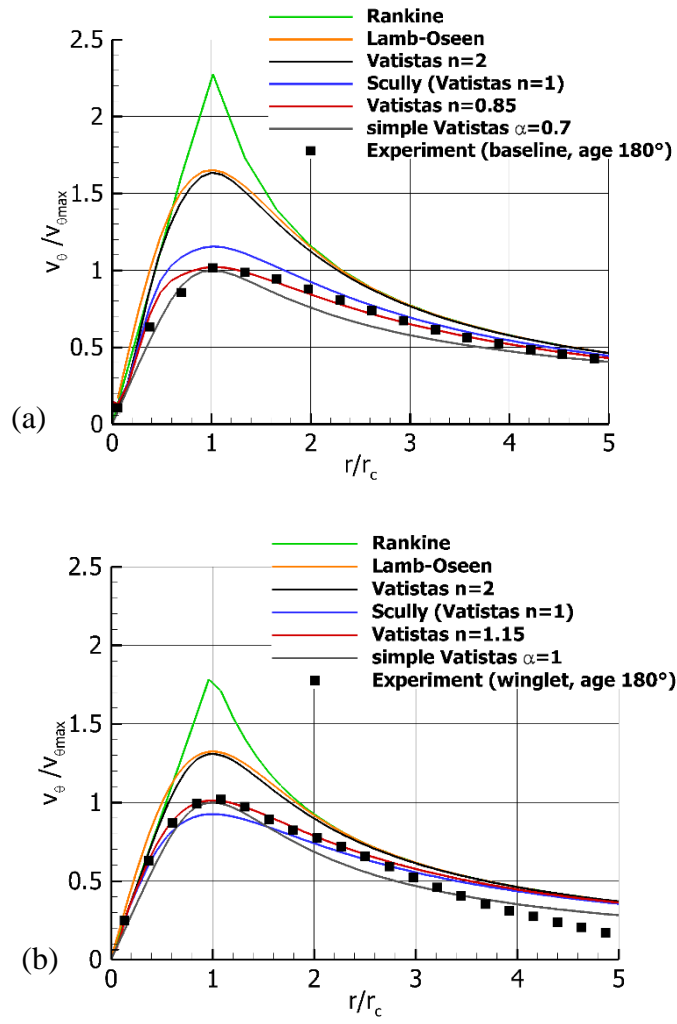


Figure 3-17 Comparison of vortex core models with current experimental data for the second vortex at rotor phase 60° (vortex age 180°) for (a) baseline and (b) winglet cases.

Table 3-4 Coefficient values that give the best fit to the experimental data

	Baseline	Winglet
n , (Original Vatisstas [36], core model)	0.85	1.15
α , (Simple Vatisstas [37], core model)	0.7	1
δ_v , (Sant et al [38], core expansion model)	6	20

Figure 3-18 presents vortex core growth for the baseline case from vortex age 12° to 348° with 6-degree intervals compared to winglet case. The vortex core expansion model of Sant et al. [38] is also presented (Equation 3.7 Table 3-3). For the core expansion model, α is used as 1.25643 and δ_v , which is a coefficient related to turbulent viscosity and suggested to be in the order of 10 for small-scale rotors, is used as $\delta_v=6$ for baseline case and $\delta_v=20$ for winglet case. S_c is a time offset calculated with $t = 0$ at vortex age 12° for the baseline case and at vortex age 156° for the winglet case. Regarding the vortex core expansion, the baseline data agrees very well in general with the expansion model of Sant et al. [38] with constants used as given above.

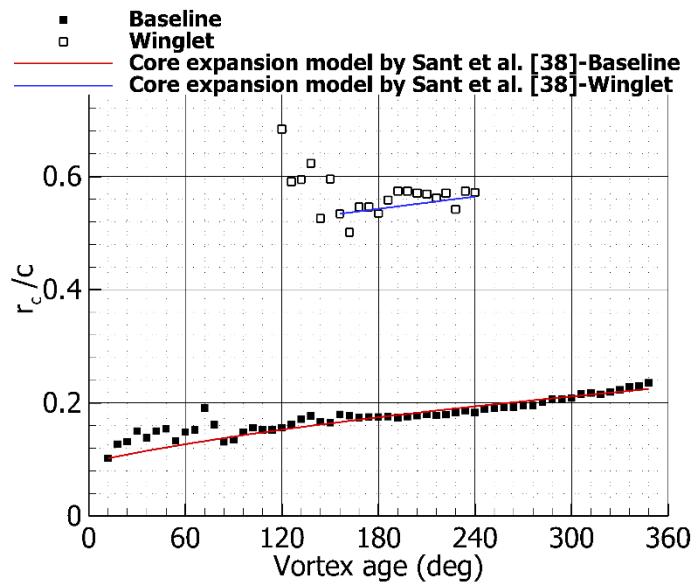


Figure 3-18 Vortex core growth for the baseline case from vortex age 12° to 348° with 6-degree intervals compared to winglet case. The vortex core expansion model of Sant et al. [38] is also presented.

The region up to vortex age 80° ($\frac{x'}{R} < 0.3$) shows some under prediction in a range of 10-20%. The vortex core size evolution for the winglet case shows a reduction in vortex core size up to about vortex age 160° ($\frac{x'}{R} < 0.4$), mainly due to the merging of the two shed vortices from the tip in this region, followed by a steady increase further

downstream. In the region where $\frac{x'}{R} > 0.4$ and for the winglet case, the expansion model shows a good curve fit to the data when a δ_v value of 20 is used, which is about 3 times that of the value used for the baseline case. The vortex core radius for the winglet case is approximately three times larger than that of the baseline case in general.

For the baseline case, the vortex core radius to blade tip chord length ratio varies from 10% to 24% from vortex age 12° to 348° , respectively. This value was measured about 7.5%-10% in the near wake region of a HAWT in Massouh and Dobrev [22] experiments.

3.2.3 Effects on induced drag

For low-speed 3D flows, the induced drag can be estimated using the measured vortex induced velocity vector components as described in Birch *et al.* [39] and Kusunose [40]. Similar to our current measurement cases, the PIV measurement plane in those studies is also perpendicular to the vortex axis, and equation 3.8 given below is used to estimate the induced drag levels.

$$D_i = \iint_S \frac{1}{2} \rho_\infty (\overline{u_v^2} + \overline{v_v^2}) dx dy \quad (3.8)$$

$\overline{u_v}$ and $\overline{v_v}$ are phase-averaged vortex induced velocity vectors. This equation is derived from application of the momentum integral theorem, employing the control volume method [39]. The vortex induced velocities are the components of the crossflow velocity in the measuring plane which is perpendicular to the vortex axis. The whole PIV measurement domain is used for the integration.

Figure 3-19 shows the estimated induced drag magnitudes for both baseline and winglet cases, calculated for rotor phases of 24° to 114° . Due to the existence of the blade in the camera field of view for rotor phases of 0° , 6° , 12° , 18° , and 120° , the shadow and data blanking are different for baseline and winglet cases. Therefore, these

data are not comparable, and they are not presented. It is important to note that as there exist three vortex structures in the measurement plane shed from three consecutive blades of the rotor, the calculated induced drag can roughly be assumed as the total induced drag of the rotor. Results show that there is a noticeable decrease (about 15% in average) in the calculated induced drag levels when the winglets are attached. This reduction in the induced drag is consistent with the increase in the power production (around 3-4%) observed in turbine power measurements around the design TSR of 6 when winglets were used (see section 3.1). As the rotor phase angle increases the difference in estimated induced drag between baseline and winglet cases increases. This could be due to the faster dissipation of the vortices for the winglet case compared to the baseline case. Also for both baseline and winglet cases starting from rotor phase 24°, the calculated induced drag decreases with rotor phase. This can be due to the dissipation of the vortices as they age in general [41].

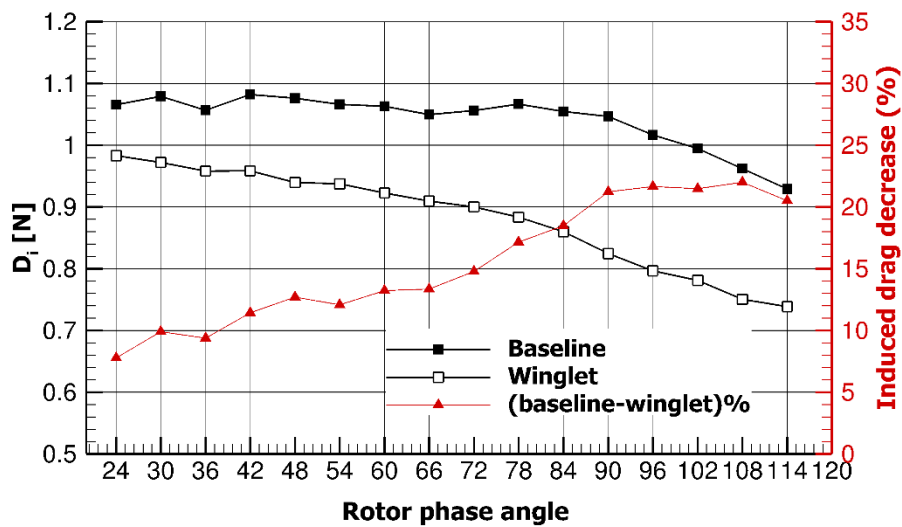


Figure 3-19 Estimated rotor induced drag for baseline and winglet cases, calculated for rotor phases 24° to 114°

In order to compare the estimated induced drag reduction levels with the excess parasitic drag (sum of profile and friction drags) of the rotor due to the presence of winglets at blade tips, we performed XFOIL analysis [42] of the winglet's airfoil (PSU 94-097) at Reynolds numbers corresponding to the relative speed of the rotor at TSR equal to 6. The estimated excess parasitic drag force of the three winglets is around

0.09 N, which is approximately 45% less than the average decrease in the calculated induced drag due to the presence of the winglets. This is consistent with observed results that winglets are causing a reduction in the induced drag of the rotor operating at TSR equal to 6.

3.2.4 Vortex meandering analysis

It has been well established in the literature that tip vortices in water or wind tunnel exhibit a low frequency fluctuating motion called meandering or wandering, induced externally to the vortex [43,44]. Because of this fluctuating motion, any time-averaged Eulerian point measurement is a weighted average in both time and space [45] which can lead to the measurement of decreased swirl velocity, higher vortex core radius, and higher turbulent kinetic energy compared to their correct value (i.e., without meandering)[46].

In PIV measurements, “conditional” averaging method is required to get rid of (or minimize) these possible errors in the characterization of tip vortex structures. In this section, the conditional averaging technique of PIV data and its results are presented and compared to “normal” averaged data.

In order to have a more precise meandering analysis, it is better to have vector maps with smaller vector spacing. To this aim, captured PIV image pairs were reprocessed utilizing adaptive correlation method with 32×32 pixels final interrogation area size with 50% overlap. Moving average validation was conducted on the vector maps before calculating the vector statistics. The vector spacing was obtained equal to 1.44 mm.

The most critical point in the meandering analysis is to determine the vortex core centers. The vortex core center coordinates in each instantaneous vector map were found by calculating the circulation for each node of the domain (vector coordinates) around a square path in a MATLAB code developed for this study. The node with

maximum circulation magnitude is defined as the vortex core center in each instantaneous vector map. The reason for choosing a square path instead of a circular path is that the instantaneous axial and lateral velocities could be directly used for horizontal and vertical sides of the path, respectively. The side length of the path was found by trial and error to have the minimal turbulent kinetic energy and maximal vorticity magnitudes at the vortex centers after the conditional averaging. In general, the path length was chosen approximately equal to the vortex core diameter measured from normal phase-averaged data (presented in previous sections) for each vortex age. Figure 3-20 shows the schematic of the integration path around each node with axial and lateral velocities.

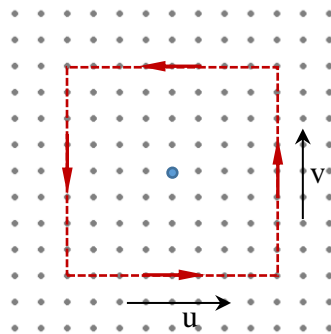


Figure 3-20 Schematic of the path used to calculate circulation around each node.

It should be noted that it was not possible to calculate circulation for the vortex ages that were close to the boundaries of the measurement windows in which the distance to the edge was less than the integration path length.

The meandering analysis was performed for baseline case from vortex age 30° to 330° with 30-degree intervals. For the winglet case, only the vortex ages 180° , 210° and, 240° (which correspond to the second vortex shed from blade#2) were considered for meandering analysis. The reason behind not analyzing the other vortex ages of winglet case was that for the vortex ages less than 180° , the double vortices shed from the blade tip have not completely merged to develop a single vortex. Concerning vortex ages higher than 240° , due to small differences in the assembly of the winglets to the

blade tips, the behavior of the third vortex is different from the behavior of the second vortex, and it might not be appropriate to be considered as a continuation of vortex aging. Figure 3-21 shows the vortex center locations obtained from instantaneous vector maps for the vortex ages in which the meandering analysis was performed.

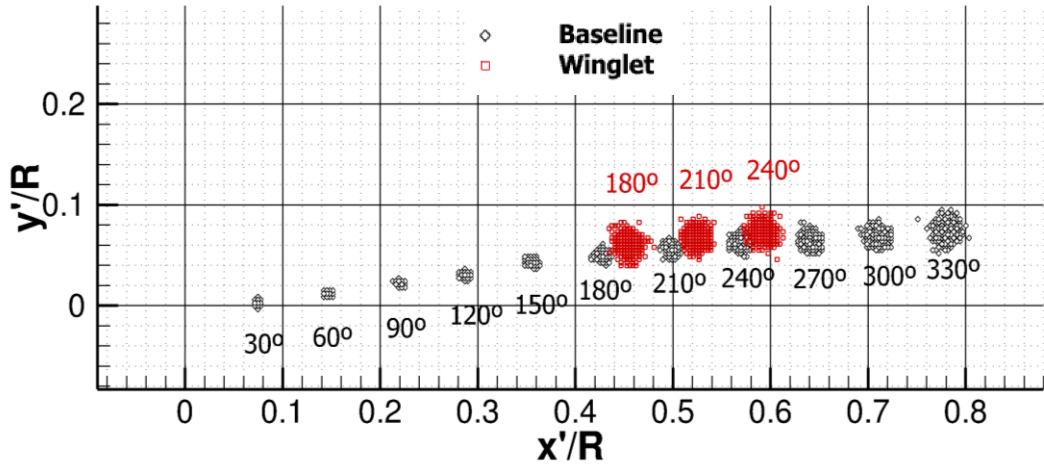


Figure 3-21 vortex center locations obtained from instantaneous vector maps for vortex age 30° to vortex age 330° with 30-degree intervals.

As it is shown in Figure 3-21, as the vortices move downstream, the area in which the instantaneous vortex centers are located is increased for both baseline and winglet vortices consistent with the observations of Nemes et al. [47] and Masouh and Dobrev [22].

After finding the vortex core centers in every instantaneous vector map associated with each particular vortex age, the coordinates were recorded and used to find the meandering amplitude of that particular vortex age. The meandering amplitude is defined as the standard deviation of vortex center coordinates calculated using equation 3.7 as also given in [44],

$$\sigma_x = \sqrt{\frac{1}{N-1} \sum_{i=1}^N (x_i - \bar{x})^2} \quad (3.7)$$

N is the number of instantaneous vector maps for each vortex age (i.e., the number of captured image pairs for each rotor phase). The vortex center meandering amplitude was computed independently for each axis (σ_x, σ_y).

Figure 3-22 shows the vortex meandering amplitude in axial and lateral directions from vortex age 30° to vortex age 330° with 30° -degree intervals for baseline case and from vortex age 180° to 240° with 30° -degree intervals for winglet case. The meandering amplitude is increased in both axial σ_x and lateral σ_y directions as the vortices move downstream (i.e., as the vortices age) similar to observation of Massouh and Dobrev [22] for tip vortices of a model wind turbine.

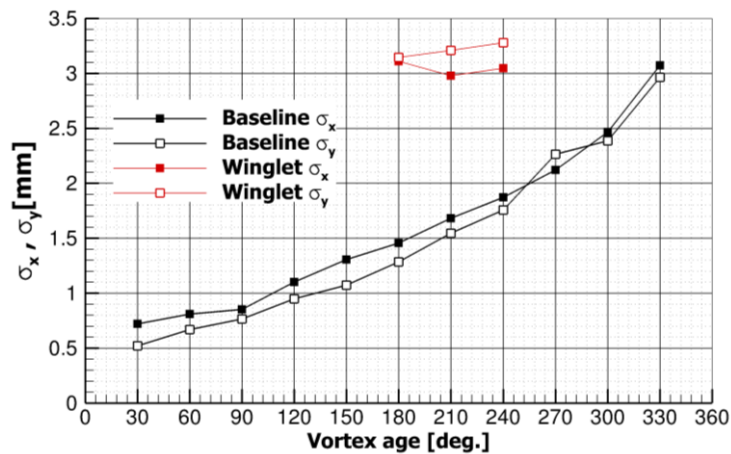


Figure 3-22 Vortex meandering amplitude in axial and lateral directions for baseline and winglet vortices.

The cause of meandering motion of a vortex in a wind tunnel can be several facts such as free stream turbulence, wind tunnel wall boundary, as well as the vibration of the solid boundary (wing or blade)[44]. Devenport et al. [43] and Heyes et al.[48] found that as the vortex becomes stronger, it is more resistant to the vortex meander. The opposite should be valid, suggesting that if the external source causing the meandering remained constant while the vortex strength decreases as it moves downstream (because of vortex dissipation), the meandering amplitude should increase.

To filter out the effects of unsteady vortex meandering for each vortex age, the coordinates were shifted to have the vortex core centers at coordinate (0,0) in all instantaneous vector maps associated with that particular vortex age. Then, vector statistics analysis was performed to obtain “conditionally” phase-averaged vector map.

Figure 3-23 shows a comparison of swirl velocity magnitude, vorticity, and turbulent kinetic energy distribution along a horizontal line intersecting the vortex core center for conditionally phase-averaged and normal phase-averaged data for vortex age 60° for the baseline case. Figure 3-24 and Figure 3-25 show similar distributions for vortex ages 210° and 300° , respectively.

As shown in Figure 3-23 the swirl velocity, vorticity, as well as turbulent kinetic energy distribution, are quite similar for the conditional and normal averaged data at vortex age 60° . As the meandering amplitude is very small in this vortex age, the difference between conditional and normal averaged data was not captured. Please note that the meandering amplitude is about 0.6 mm in both axial and radial directions whereas the vector spacing is approximately 1.44 mm. By increasing the vortex age, the meandering amplitude increases and as expected, the conditional and normal averaged data are not similar anymore.

As shown in Figure 3-24 and Figure 3-25, from swirl velocity magnitude distribution, it was observed that for both 210° and 300° vortex ages, the maximum swirl velocities observed at viscous core radius are higher in conditional averaged data compared to the normal averaged data. As expected, the difference is increased by increasing the vortex age. Figure 3-26 shows swirl velocity distribution in conditional averaged and normal averaged data, for vortex ages 60° , 210° and, 300° for the baseline case over a horizontal line intersecting the vortex centers. As seen in Figure 3-26, by increasing the vortex age, the maximum swirl velocity magnitudes are decreasing in both conditional and normal averaged data which is consistent regarding vortex dissipation.

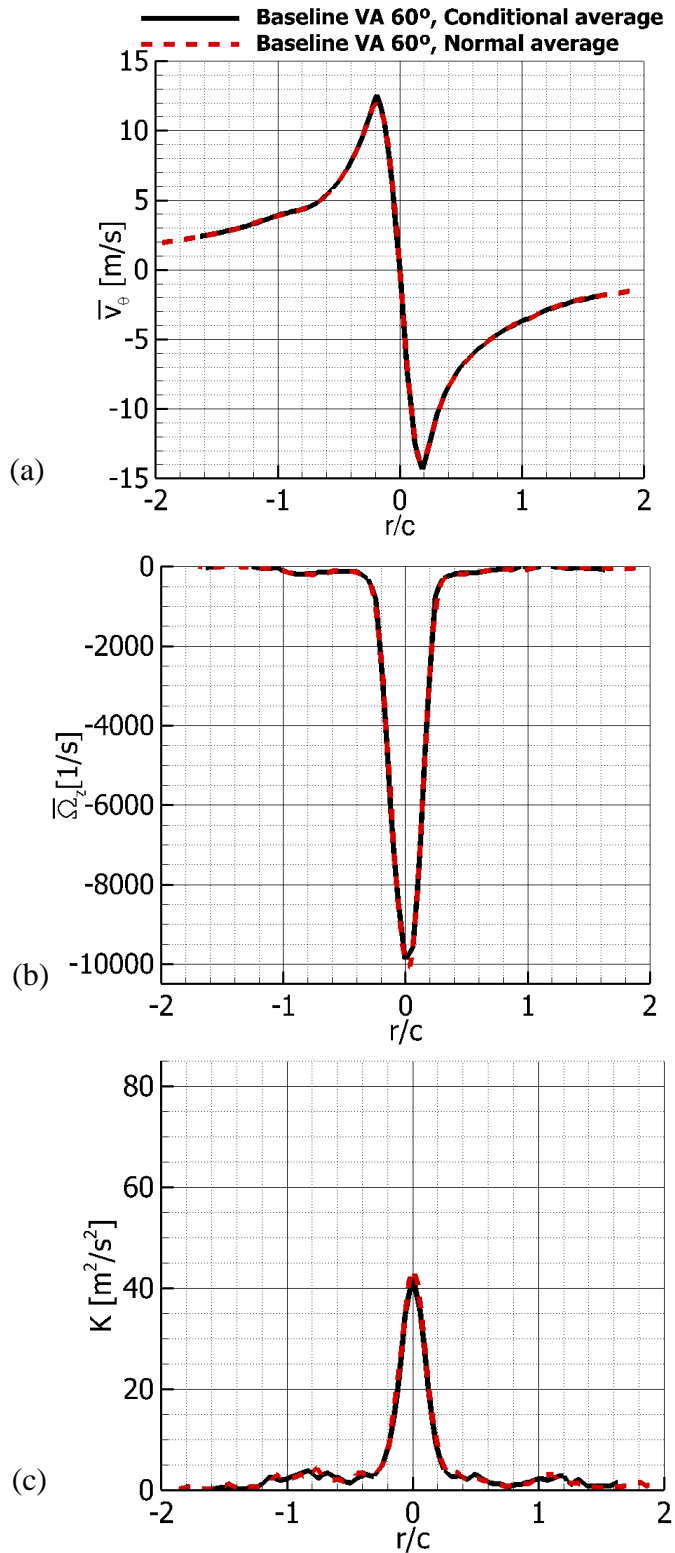


Figure 3-23 Comparison of swirl velocity magnitude (a), vorticity (b) and turbulent kinetic energy (c) distribution along a horizontal line intersecting the vortex core center for conditionally phase-averaged and normal phase-averaged data for vortex age 60° for the baseline case.

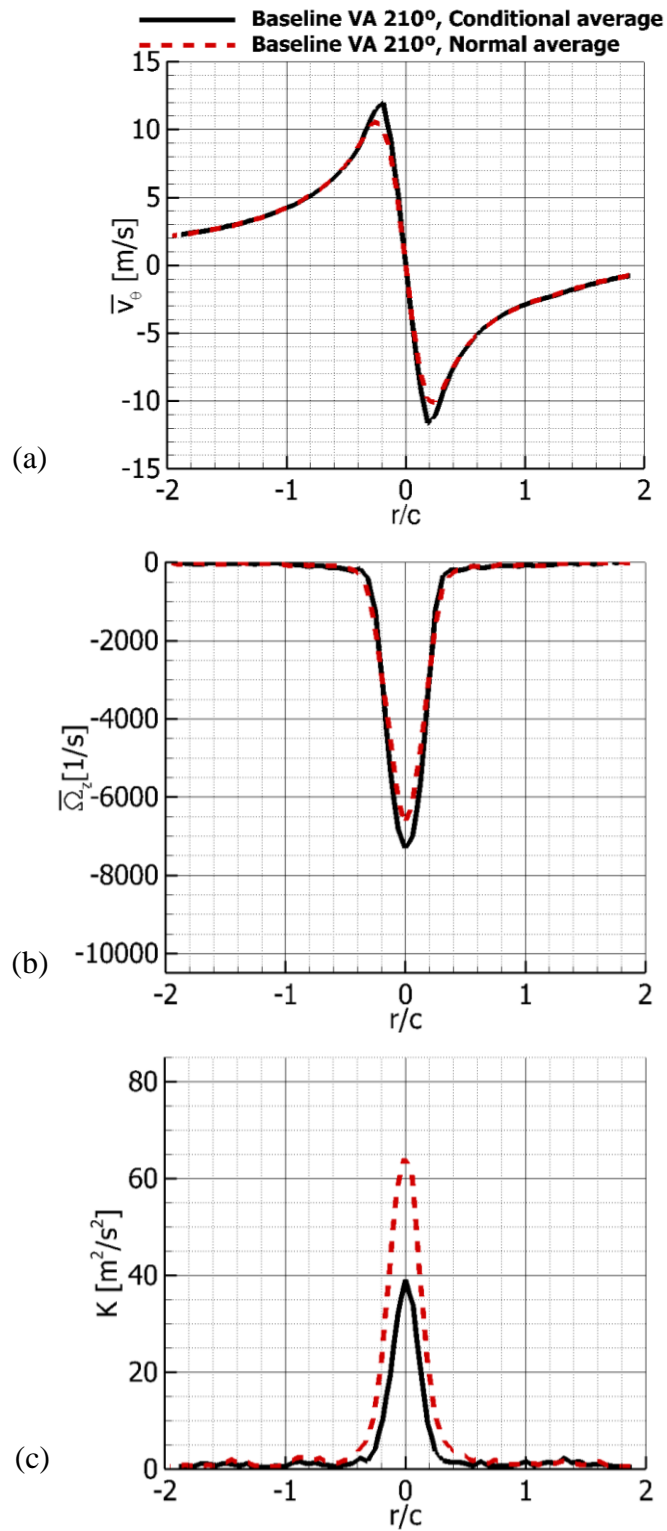


Figure 3-24 Comparison of swirl velocity magnitude (a), vorticity (b) and turbulent kinetic energy (c) distribution along a horizontal line intersecting the vortex core center for conditionally phase-averaged and normal phase-averaged data for vortex age 210° for the baseline case.

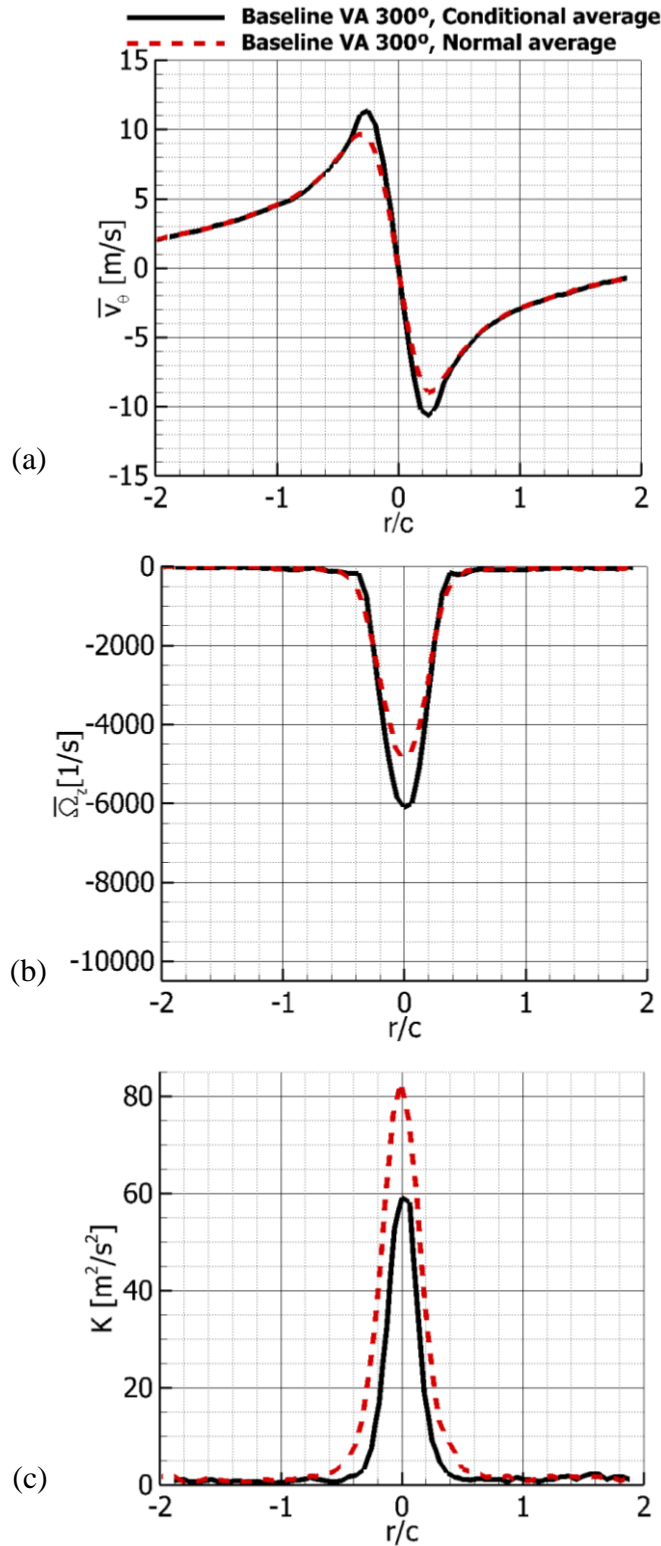


Figure 3-25 Comparison of swirl velocity magnitude (a), vorticity (b) and turbulent kinetic energy (c) distribution along a horizontal line intersecting the vortex core center for conditionally phase-averaged and normal phase-averaged data for vortex age 300° for the baseline case.

Vortex viscous core radius growth with vortex age is shown in Figure 3-27 for both conditional and normal averaged data. It is observed that the vortex core radii are higher in normal averaged data compared to the conditional averaged data and the difference is increasing as the vortex moves downstream. The vortex core expansion model of Sant et al. [38] is also presented (Equation 3.7 Table 3-3). For the core expansion model, $\delta_v = 6$ is used for normal averaged data (as shown in previous section). However, for conditionally averaged data, core expansion model with $\delta_v = 0.6$ has a good fit with the experimental data which shows the importance of meandering effects on the tip vortex characteristics.

Concerning vorticity distributions, for both 210° and 300° vortex ages, the maximum vorticity magnitudes occurring at vortex core centers are higher in conditionally averaged data compared to the normal averaged data and the difference in between increases by increasing the vortex age. Figure 3-28 shows the maximum vorticity occurring at vortex core centers for the conditionally and normal averaged data for the baseline vortex from vortex age 30° to 330°. It is observed that by increasing the vortex age, the maximum vorticity is decreased in both conditional and normal averaged as expected, due to vortex dissipation.

About turbulent kinetic energy distributions, for both 210° and 300° vortex ages, the normal averaged data show higher levels of turbulent kinetic energy in the vortex core vicinity compared to conditional averaged data which is expected as a consequence of vortex meandering motion. This increase in the turbulent kinetic energy due to meandering is consistent with the PIV measurements of Beresh et al. [44].

Figure 3-29 presents the maximum turbulent kinetic energy magnitudes occurring at vortex core centers for the conditionally averaged as well as normal averaged data for the baseline vortex from vortex age 30° to 330°. For normal averaged data, it is observed that the turbulent kinetic energy levels are increasing as the vortices age, which is consistent with the increasing vortex meandering amplitudes. On the other hand, for conditionally averaged data, the maximum turbulent kinetic energy levels

observed at vortex core centers are decreased from vortex age 30° to vortex age 240° (which is consistent with vortex dissipation) but increased from vortex age 240° to vortex age 270° and then again decreased up to vortex 330°. Please note that vortex age 240° corresponds to the second vortex which is shed from blade#2. Whereas vortex ages 270°, 300°, and 330° correspond to the third vortex which is shed from blade#3, and this upward shift in turbulent kinetic energy could have occurred due to either a mismatch in pitch angle of the two blades or excess vibration in blade number #3 compared to blade#2.

Figure 3-30 shows the Comparison of swirl velocity magnitude, vorticity, and turbulent kinetic energy distribution along a horizontal line intersecting the vortex core center for conditionally phase-averaged and normal phase-averaged data for vortex age 240° for the winglet case. Similar to what is observed for baseline vortex the maximum swirl velocity magnitudes is higher in conditionally averaged data compared to the normal averaged data as shown in Figure 3-30a. Figure 3-30b shows that the maximum vorticity magnitude in the vortex core center is higher for the conditionally averaged data compared to normal averaged data.

Regarding turbulent kinetic energy distribution shown in Figure 3-30c, normal averaged data show higher levels of turbulent kinetic energy around vortex core center compared to the conditional averaged data. In general, it is concluded that normal averaging of the data could introduce several errors to vortex characteristics such as reducing the maximum swirl velocity, reducing vorticity levels in vortex core centers, increasing turbulent kinetic energy at vortex core area, and increasing the vortex core radius.

Finally, Self-similar distributions of swirl velocity from conditional averaged data of baseline vortex for vortex ages of 60°, 210°, and 300° are shown in Figure 3-31. As it is seen, the self-similar swirl distributions for all three vortex ages have acceptable fit on each other.

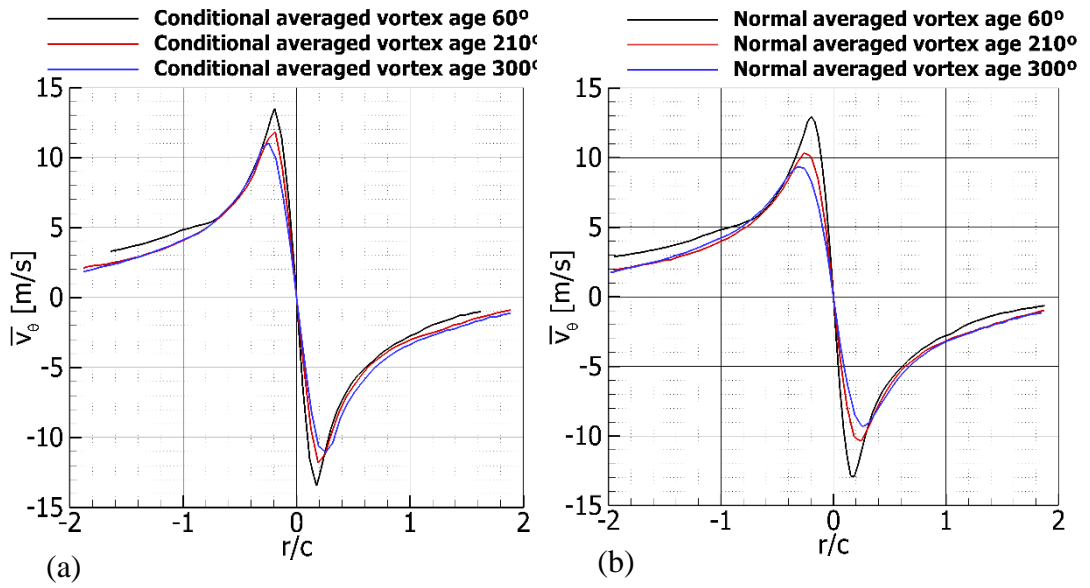


Figure 3-26 Swirl velocity distribution in conditional averaged data (a) and normal averaged data (b), for vortex ages 60°, 210° and, 300° for the baseline case over a horizontal line intersecting the vortex centers.

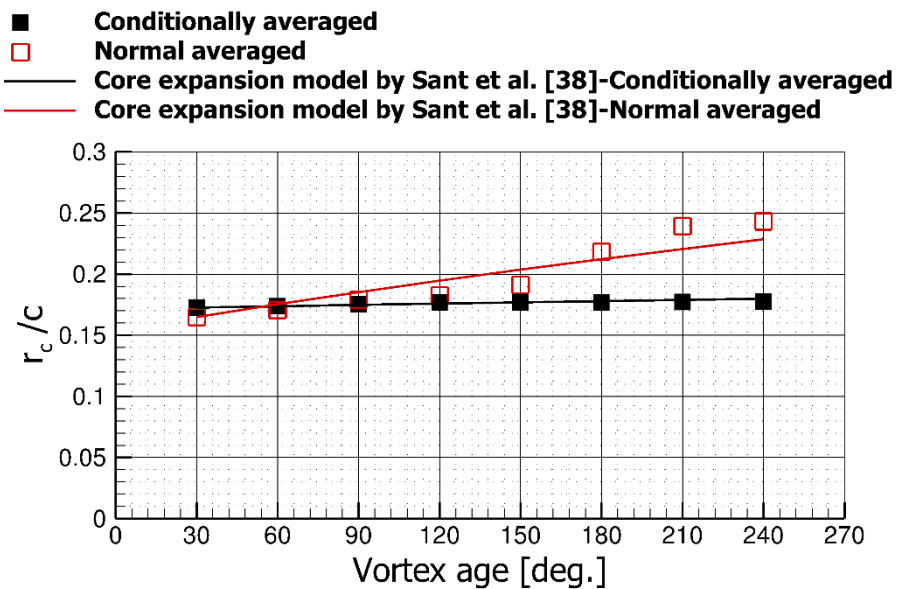


Figure 3-27 Vortex viscous core radius growth with vortex age for conditional and normal averaged data. The vortex core expansion model of Sant et al. [38] is also presented.

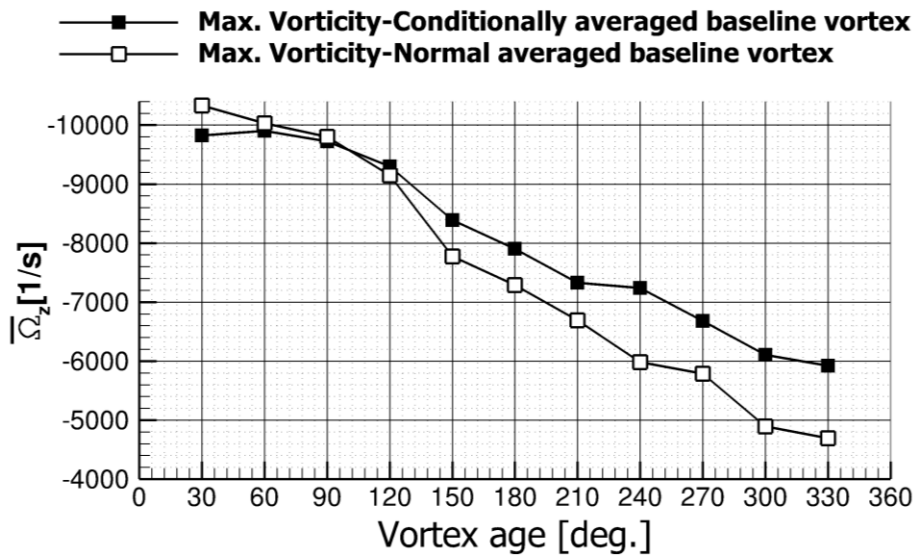


Figure 3-28 Maximum vorticity occurring at vortex core centers for the conditionally and normal averaged data of baseline vortex from vortex age 30° to 330°.

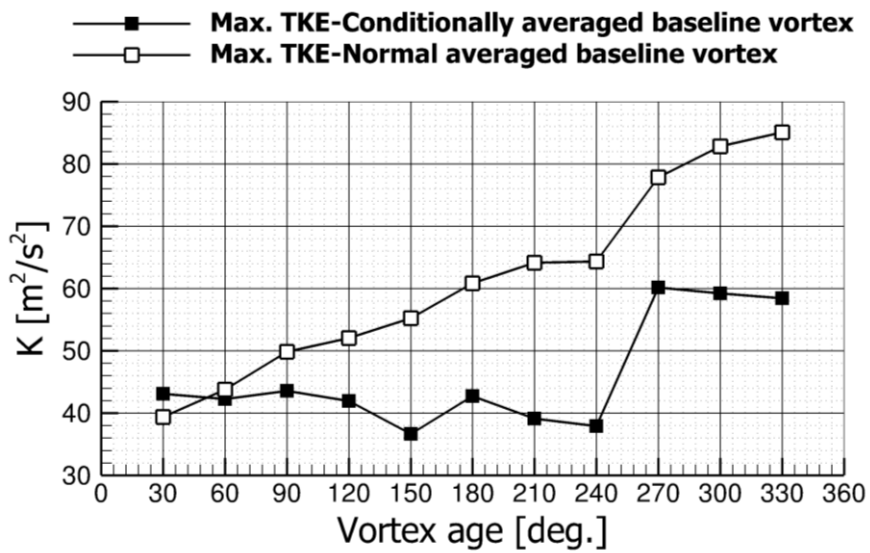


Figure 3-29 Maximum turbulent kinetic energy magnitudes occurring at vortex core centers for the conditionally and normal averaged data of baseline vortex from vortex age 30° to 330°.

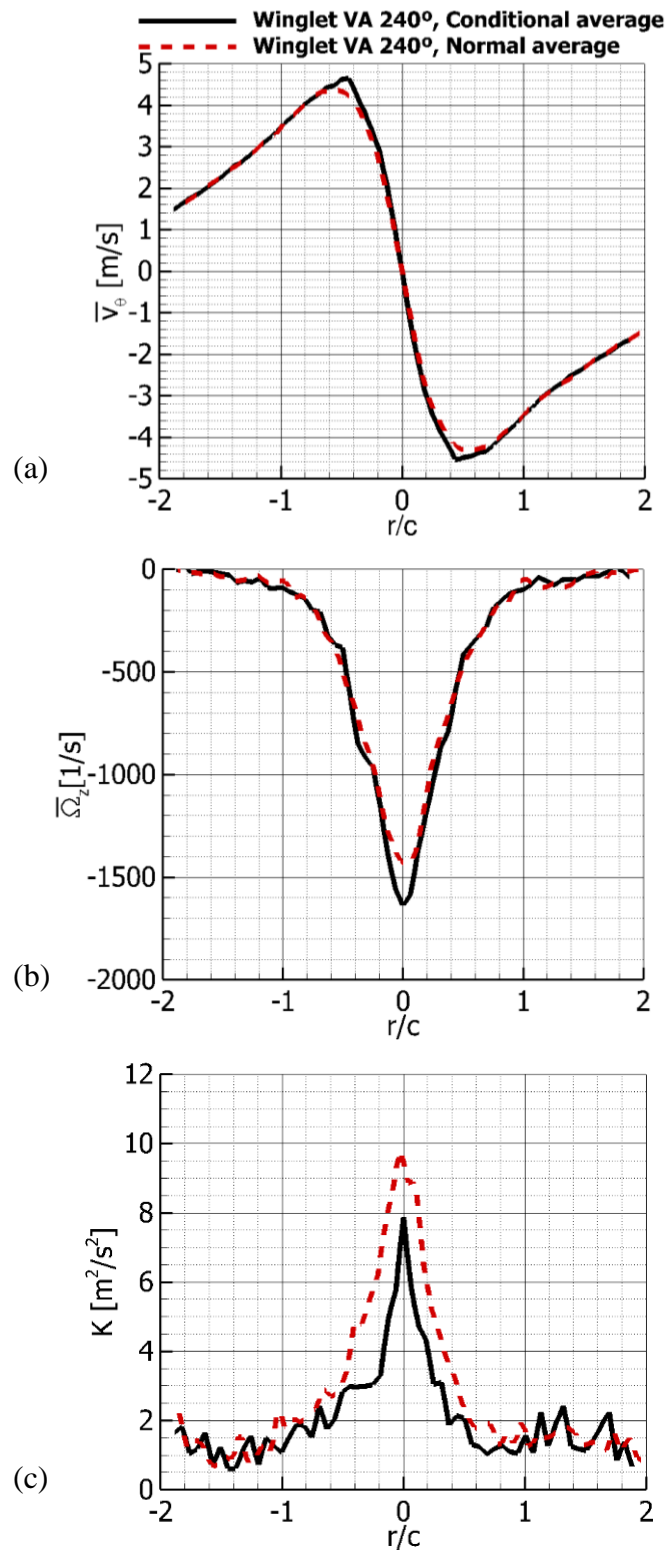


Figure 3-30 Comparison of swirl velocity magnitude (a), vorticity (b) and turbulent kinetic energy (c) distribution along a horizontal line intersecting the vortex core center for conditionally phase-averaged and normal phase-averaged data for vortex age 240° for the winglet case

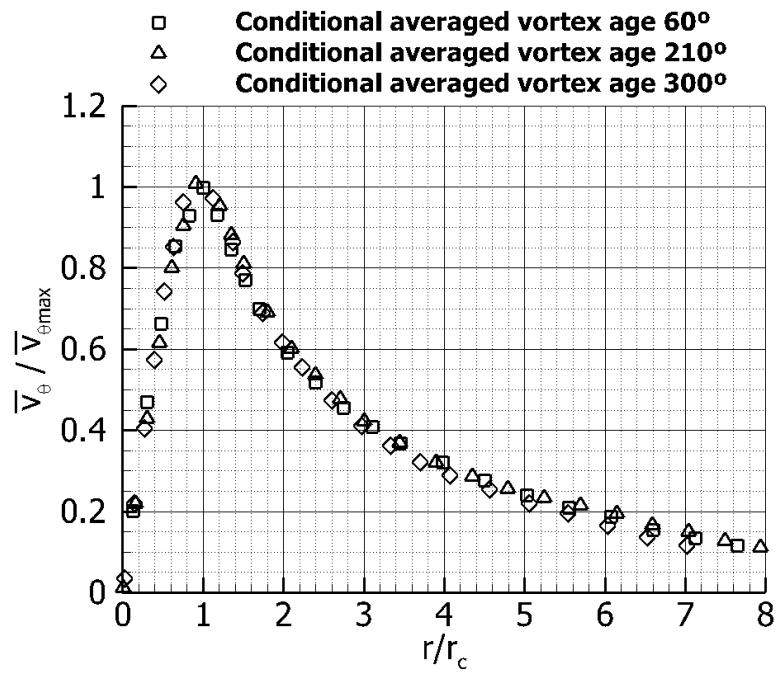


Figure 3-31 Self-similar distributions of swirl velocity in conditional averaged data of baseline vortex (ages 60°, 210°, and 300°)

CHAPTER 4

CONCLUSIONS

The focus of this study was to experimentally investigate the effects of winglets on the aerodynamic performance of two interacting similar model horizontal axis wind turbines and to see the effects of winglets on the tip vortex behavior in the very near wake region. For this purpose, a downwind winglet was designed to be attached to the blade tips of the upstream turbine. A set of wing extensions of the same height as the winglets was also manufactured to be compared.

In the first part of the study, power performances of both turbines were measured with winglets as well as with wing extensions attached to the blade tips of the upstream turbine and were compared to the baseline case (rectangular tip without any tip device). The measurements were performed in two different wind tunnels.

The first set of experiments was performed at large scale closed loop wind tunnel of Norwegian University of Science and Technology (NTNU). Power and thrust measurements were carried out on both upstream and downstream turbines while the upstream turbine was operating with and without winglets. For the wingletted turbine running at the rotor design TSR value ($TSR=6$), power coefficient increased noticeably compared to the non-wingletted case. By attaching the winglets, the thrust coefficient also increased as expected. Measurements on the second turbine were done while it was positioned at two different downstream locations with separation distances of three and six rotor diameters from the upstream turbine. For both locations of the downstream turbine, results showed that it produced less power while operating in the wake of the upstream turbine with winglets. However, the overall power efficiency of two turbines increased for the case with winglets for both three and six diameters distances in between. Additionally, it was observed that by increasing the

distance in between turbines, the power production of the downstream turbine was increased.

The second series of experiments were performed at Middle East Technical University, Center for Wind Energy (METUWIND). The same model turbines were located at the exit of an open jet wind tunnel. Power measurements on both turbines were conducted while the upstream turbine was operating with winglets as well as with wing extensions attached to its blade tips. The results were compared to the baseline case (Rectangular tip without winglets and wing extensions). Measurements showed that connecting winglets to the upstream turbine increased its power coefficient relative to the baseline case. Results with wing extensions indicated that although upstream turbine produced more power with wing extensions attached, the power coefficient remained the same as the baseline case and hence, it was less than wingletted turbine. The second turbine was positioned three rotor diameters downstream of the first turbine. Two turbine measurements show that wing extensions attached to the upstream turbine had the maximum reducing effect on the second turbines performance. The total power production of the two turbines had the maximum value with the wing extensions. From these results, initially, it seemed that using wing extensions (in other words larger rotors) are more beneficial compared to winglets. However, there are always restrictions on increasing the turbines' rotor radius. Another remarkable point is that these results were for only two turbines in line. Considering a higher number of turbines operating downstream of the first turbine, it may not be beneficial to use wing extensions (larger rotors) for the upstream turbines. However, using winglets may still be favorable regarding a higher total power production as well as less structural loads.

Phase-locked PIV measurements were conducted to see the effects of a designed set of winglets on the tip vortex behavior of the HAWT. Trajectories of three vortex structures were captured in the PIV measurement domain. These three vortices were shed from three consecutive blades of the rotor. The measurements were conducted in

21 rotor azimuthal positions defined as rotor phase angles from 0° to 120° with 6-degree intervals for both baseline and winglet cases.

Results show that for the baseline case in which there are no tip devices, there was a strong vortex shed from the wing tip. For both baseline and winglet cases, a strong trailing vorticity sheet near the blade tip was visible in the measurement plane in earlier phases of the rotor. This vorticity sheet was depicted to roll up into the tip vortex in the subsequent phases.

By attaching the winglets, two co-rotating vortex structures were captured shedding from the blade tip. These two vortices gradually merged moving downstream in the following phases and developed a single but non-uniform vortex. It was depicted that the vorticity levels inside the vortex core regions as well as maximum vortex induced velocity levels were noticeably decreased in the winglet case compared to the baseline case. Moreover, the vortex core diameter increased by attaching the winglets.

The turbulent kinetic energy was calculated using the differences between phase-averaged and instantaneous measurements for each phase. It was depicted that by increasing the phase angle, especially for the baseline case, Turbulent Kinetic Energy of the vortices was increasing, which could be due to the increase in vortex wandering motion as the vortices aged.

Regarding the overall average of rotor phases, results showed that the mixing layer thickness was higher for the winglet case. Axial velocity distribution indicated that there was further wake extension in the winglet case compared to the baseline case. For earlier phases of the rotor, TKE levels were slightly higher in winglet case compared to the baseline case. This could be due to mutual interaction of the two vortices shed from the blade tip with the winglet as they were interacting and merging. After the two vortices for the winglet case merged, the TKE levels in the mixing layer were depicted to be lower for the winglet case compared to the baseline case.

Vortex center positions were determined as the locations with zero vortex induced velocity. It was seen that for the winglet case compared to the baseline case, the tip vortices were moved further downstream in the axial direction and outward in the lateral direction. It means that there was more expansion in the wake by attaching the winglets. This is consistent with the literature as a behavior of downwind winglets. Several vortex models were compared to our experimental data. Vatistas model with $n=0.85$ seemed to have good agreement with the experiments.

The induced drag of the rotor blades was calculated for all rotor phases using vortex induced velocity vector components. Results showed that for all rotor phases, there was a noticeable decrease (about 15% in average) in calculated induced drag when the winglets were attached. This was consistent with the increase in the power production of the turbine while performing with the winglets. For both baseline and winglet cases, the calculated induced drag decreased in the following rotor phases, which could be due to the dissipation of the vortices as they aged.

From vortex meandering analysis it was observed that the meandering amplitude increases as the vortex moves downstream (i.e., ages). Additionally, it was shown that when the instantaneous vector maps from PIV measurements are normal averaged, meandering motion can introduce several errors to the vortex characteristics such as reducing the maximum swirl velocity, reducing vorticity levels in vortex core centers, increasing turbulent kinetic energy at vortex core area, and increasing the vortex core radius. However, these errors were minimal at the starting vortex ages and were increased as the vortices moved downstream.

Suggestions for Future works are included below:

- In this study, it has been observed that the effects of winglets on the behavior of the model turbine were very sensitive to the assembly angle of the winglets. So, for similar studies, it will be beneficial to have a more robust winglet attachment mechanism.

- Hotwire measurements can be performed in several downstream positions of the model turbine to see the effects of winglets on the velocity deficit and its recovery in the wake region.
- The maximum distance in between model wind turbines were six turbine rotor diameters. Similar experiments can be conducted with larger distance in between model turbines. Of course, this requires a closed-loop wind tunnel with longer test section (e.g., atmospheric boundary layer simulation test section).
- Phase-locked PIV measurements were conducted in the blade tip region covering only up to about 18 blade tip chord length downstream. PIV measurements can be performed in further downstream to see the behavior of tip vortices in the following vortex ages.
- Data provided in this study can be a validation case for computational fluid dynamics studies that are aiming to design optimum winglets for wind turbines.

REFERENCES

- [1] IEA, Key World Energy Statistics 2016, Statistics (Ber). (2016) 80. doi:10.1787/9789264039537-en.
- [2] IRENA, REthinking Energy, 2017.
- [3] GWEC, Global Wind Report 2016, 2017. <http://files.gwec.net/files/GWR2016.pdf>.
- [4] P. Denholm, M. Hand, M. Jackson, S. Ong, Land-Use Requirements of Modern Wind Power Plants in the United States Land-Use Requirements of Modern Wind Power Plants in the United States, Natl. Renew. Energy Lab. Technical (2009).
- [5] R. Eppler, Induced drag and winglets, *Aerosp. Sci. Technol.* 1 (1997) 3–15. doi:10.1016/S1270-9638(97)90019-5.
- [6] G. a M. Van Kuik, The Lanchester-Betz-Joukowsky limit, *Wind Energy.* 10 (2007) 289–291. doi:10.1002/we.218.
- [7] L.J. Vermeer, J.N. Sørensen, a. Crespo, Wind turbine wake aerodynamics, *Prog. Aerosp. Sci.* 39 (2003) 467–510. doi:10.1016/S0376-0421(03)00078-2.
- [8] J.D. Anderson, *Fundamentals of Aerodynamics (Mcgraw-Hill Series in Aeronautical and Aerospace Engineering)*, 4th ed., McGraw-Hill Science/Engineering/Math, 2005. <http://www.worldcat.org/isbn/0072950463>.
- [9] B. Sanderse, Aerodynamics of wind turbine wakes: Literature review, (2009) 1–46. doi:10.1002/we.
- [10] E. Branlard, *Wind Turbine Aerodynamics and Vorticity-Based Methods*, Springer International Publishing, Cham, 2017. doi:10.1007/978-3-319-55164-7.
- [11] D. Medici, *Experimental Studies of Wind Turbine Wakes-Power Optimisation and Meandering*, (2005).

- [12] M. Gaunaa, J. Johansen, Determination of the Maximum Aerodynamic Efficiency of Wind Turbine Rotors with Winglets, *J. Phys. Conf. Ser.* 75 (2007) 12006. doi:10.1088/1742-6596/75/1/012006.
- [13] M.D. Maughmer, Design of Winglets for High-Performance Sailplanes, *J. Aircr.* 40 (2003) 1099–1106. doi:10.2514/2.7220.
- [14] J. Johansen, N. Sørensen, Aerodynamic investigation of Winglets on Wind Turbine Blades using CFD, Riso-R-1543(EN). 1543 (2006). http://www.risoe.dtu.dk/da/Knowledge_base/publications/Reports/ris-r-1543.aspx?sc_lang=en.
- [15] D. Gertz, D. a. Johnson, N. Swytk-Binnema, An Evaluation Testbed for Wind Turbine Blade Tip Designs - Winglet Results, *Wind Eng.* 36 (2012) 389–410. doi:10.1260/0309-524X.36.4.389.
- [16] M.A. Elfarra, N. Sezer-Uzol, I.S. Akmandor, NREL VI rotor blade: numerical investigation and winglet design and optimization using CFD, *Wind Energy.* 17 (2014) 605–626. doi:10.1002/we.1593.
- [17] N. Tobin, A. Hamed, L. Chamorro, An Experimental Study on the Effects of Winglets on the Wake and Performance of a Model Wind Turbine, *Energies.* 8 (2015) 11955–11972. doi:10.3390/en81011955.
- [18] Y. Shimizu, E. Ismaili, Y. Kamada, T. Maeda, Power augmentation of a HAWT by Mie-type tip vanes, considering wind tunnel flow visualisation, blade-aspect ratios and Reynolds number, *Wind Eng.* 27 (2003) 183–194. doi:10.1260/030952403769016663.
- [19] A. Abdulrahim, E. Anik, O. Uzol, Effects of Mie Vanes and Tip Injection on the Performance and Wake Characteristics of a HAWT, in: *34th Wind Energy Symp.*, American Institute of Aeronautics and Astronautics, Reston, Virginia, 2016: pp. 143–160. doi:10.2514/6.2016-0519.
- [20] I. Grant, M. Mo, X. Pan, P. Parkin, J. Powell, H. Reinecke, K. Shuang, F. Cotton, D. Lee, An experimental and numerical study of the vortex filaments in the wake of an operational, horizontal-axis, wind turbine, *J. Wind Eng. Ind. Aerodyn.* 85 (2000) 177–189. doi:10.1016/S0167-6105(99)00139-7.

- [21] J.P. Xiao, J. Wu, L. Chen, Z.Y. Shi, Particle image velocimetry (PIV) measurements of tip vortex wake structure of wind turbine, *Appl. Math. Mech.* (English Ed. 32 (2011) 729–738. doi:10.1007/s10483-011-1452-x.
- [22] F. MASSOUH, I. DOBREV, Investigation of wind turbine flow and wake, *J. Fluid Sci. Technol.* 9 (2014) 167–176. https://www.jstage.jst.go.jp/article/jfst/9/3/9_2014jfst0025/_article/cited-by.
- [23] P.-Å. Krogstad, J.A. Lund, An experimental and numerical study of the performance of a model turbine, *Wind Energy.* 15 (2012) 443–457. doi:10.1002/we.482.
- [24] P.Å. Krogstad, P.E. Eriksen, “Blind test” calculations of the performance and wake development for a model wind turbine, *Renew. Energy.* 50 (2013) 325–333. doi:10.1016/j.renene.2012.06.044.
- [25] F. Pierella, P.Å. Krogstad, L. Sætran, Blind Test 2 calculations for two in-line model wind turbines where the downstream turbine operates at various rotational speeds, *Renew. Energy.* 70 (2014) 62–77. doi:10.1016/j.renene.2014.03.034.
- [26] P.-Å. Krogstad, L. Sætran, M.S. Adaramola, “Blind Test 3” calculations of the performance and wake development behind two in-line and offset model wind turbines, *J. Fluids Struct.* 52 (2015) 65–80. doi:10.1016/j.jfluidstructs.2014.10.002.
- [27] M.D. Maughmer, T.S. Swan, S.M. Willits, Design and Testing of a Winglet Airfoil for Low-Speed Aircraft, *J. Aircr.* 39 (2002) 654–661. doi:10.2514/2.2978.
- [28] A.J. Wheeler, A.R. Ganji, *Introduction to Engineering Experimentation*, 2nd Edition, Pearson, Orentice Hall, 2004.
- [29] B.G. Van Der Wall, H. Richard, Analysis methodology for 3C-PIV data of rotary wing vortices, *Exp. Fluids.* 40 (2006) 798–812. doi:10.1007/s00348-006-0117-x.
- [30] N. Vermeer, How fast is a tip vortex?, *Nineth IEA Symp. Aerodyn. Wind Turbines*, Stock. Sweden. (1995) 15–20.

- [31] Wi.J. Devenport, C.M. Vogel, J.S. Zsoldos, Flow structure produced by the interaction and merger of a pair of co-rotating wing-tip vortices, *J. Fluid Mech.* 394 (1999) 357–377. doi:10.1017/S0022112099005777.
- [32] A. Romeos, A. Giannadakis, K. Perrakis, T. Panidis, Co-rotating vortex interaction, *Aircr. Eng. Aerosp. Technol.* 88 (2016) 285–293. doi:10.1108/AEAT-02-2015-0071.
- [33] W.J.M. Rankine, *Manual of Applied Mechanics*, (1858).
- [34] C.W. Oseen, Über Wirbelbewegung in Einer Reibenden Flüssigkeit, *Ark. Foer Mat. Astron. Och Fys.* (1911).
- [35] M.P. Scully, *Computation of helicopter rotor wake geometry and its influence on rotor harmonic airloads*, 1975.
- [36] G.H. Vatistas, V. Kozel, W.C. Mih, A simpler model for concentrated vortices, *Exp. Fluids.* 11 (1991) 73–76. doi:10.1007/BF00198434.
- [37] G.H. Vatistas, Simple Model for Turbulent Tip Vortices, *J. Aircr.* 43 (2006) 1577–1579. doi:10.2514/1.22477.
- [38] T. Sant, G. van Kuik, G.J.W. van Bussel, Estimating the angle of attack from blade pressure measurements on the NREL Phase VI rotor using a free wake vortex model:axial conditions, *Wind Energy.* 9 (2006) 549–577. doi:10.1002/we.201.
- [39] D. Birch, T. Lee, F. Mokhtarian, F. Kafyeke, Structure and Induced Drag of a Tip Vortex, *J. Aircr.* 41 (2004) 1138–1145. doi:10.2514/1.2707.
- [40] K. Kusunose, Development of a universal wake survey data analysis code, in: *15th Appl. Aerodyn. Conf., American Institute of Aeronautics and Astronautics*, Atlanta, GA, 1997: pp. 617–626. doi:10.2514/6.1997-2294.
- [41] S.I. Green, ed., *Fluid Vortices*, Springer Netherlands, Dordrecht, 1995. doi:10.1007/978-94-011-0249-0.
- [42] M. Drela, XFOIL: An Analysis and Design System for Low Reynolds Number Airfoils, in: 1989: pp. 1–12. doi:10.1007/978-3-642-84010-4_1.
- [43] W.J. Devenport, M.C. Rife, S.I. Liapis, G.J. Follin, The structure and development of a wing-tip vortex, *J. Fluid Mech.* 312 (1996) 67. doi:10.1017/S0022112096001929.

- [44] S.J. Beresh, J.F. Henfling, R.W. Spillers, Meander of a fin trailing vortex and the origin of its turbulence, *Exp. Fluids*. 49 (2010) 599–611. doi:10.1007/s00348-010-0825-0.
- [45] S.I. Green, A.J. Acosta, Unsteady flow in trailing vortices, *J. Fluid Mech.* 227 (1991) 107. doi:10.1017/S0022112091000058.
- [46] G.R. Baker, S.J. Barker, K.K. Bofah, P.G. Saffman, Laser anemometer measurements of trailing vortices in water, *J. Fluid Mech.* 65 (1974) 325. doi:10.1017/S0022112074001418.
- [47] A. Nemes, M. Sherry, D. Lo Jacono, H.M. Blackburn, J. Sheridan, Evolution and breakdown of helical vortex wakes behind a wind turbine, *J. Phys. Conf. Ser.* 555 (2014) 12077. doi:10.1088/1742-6596/555/1/012077.
- [48] A.L. Heyes, R.F. Jones, D.A.R. Smith, Wandering of wing-tip vortices, 12th Int. Symp. Appl. Laser Tech. to Fluid Mech. Lisbon, Port. July 2004. (2004) 35–3.

APPENDIX A

DETAILED FIGURES FROM PIV MEASUREMENTS

This chapter contains detailed figures from PIV measurements on flow field characteristics near the tip. In order to understand the behavior of tip vortices shed from rotor blades affected by winglets, PIV measurement results of all rotor phases are presented from Figure A. 1 to Figure A. 4. Especially the interaction between two vortices shed from winglet is clearly visible in these plots. Figure A. 1 shows Phase-averaged distribution of axial velocity \bar{u} of rotor phases 0° to 120° for the baseline (left) and winglet (right) cases with 6-degree intervals (total of 21 rotor phases). Figure A. 2 contains Phase-averaged distribution of lateral velocity \bar{v} of rotor phases 0° to 120° for the baseline (left) and winglet (right) cases with 6-degree intervals. Similarly, Figure A. 3 and Figure A. 4 present the distribution of phase-averaged out-of-plane vorticity $\overline{\Omega_z}$ and turbulent kinetic energy, respectively. Out-of-plane vorticity plots are superimposed by vortex induced velocity vectors.

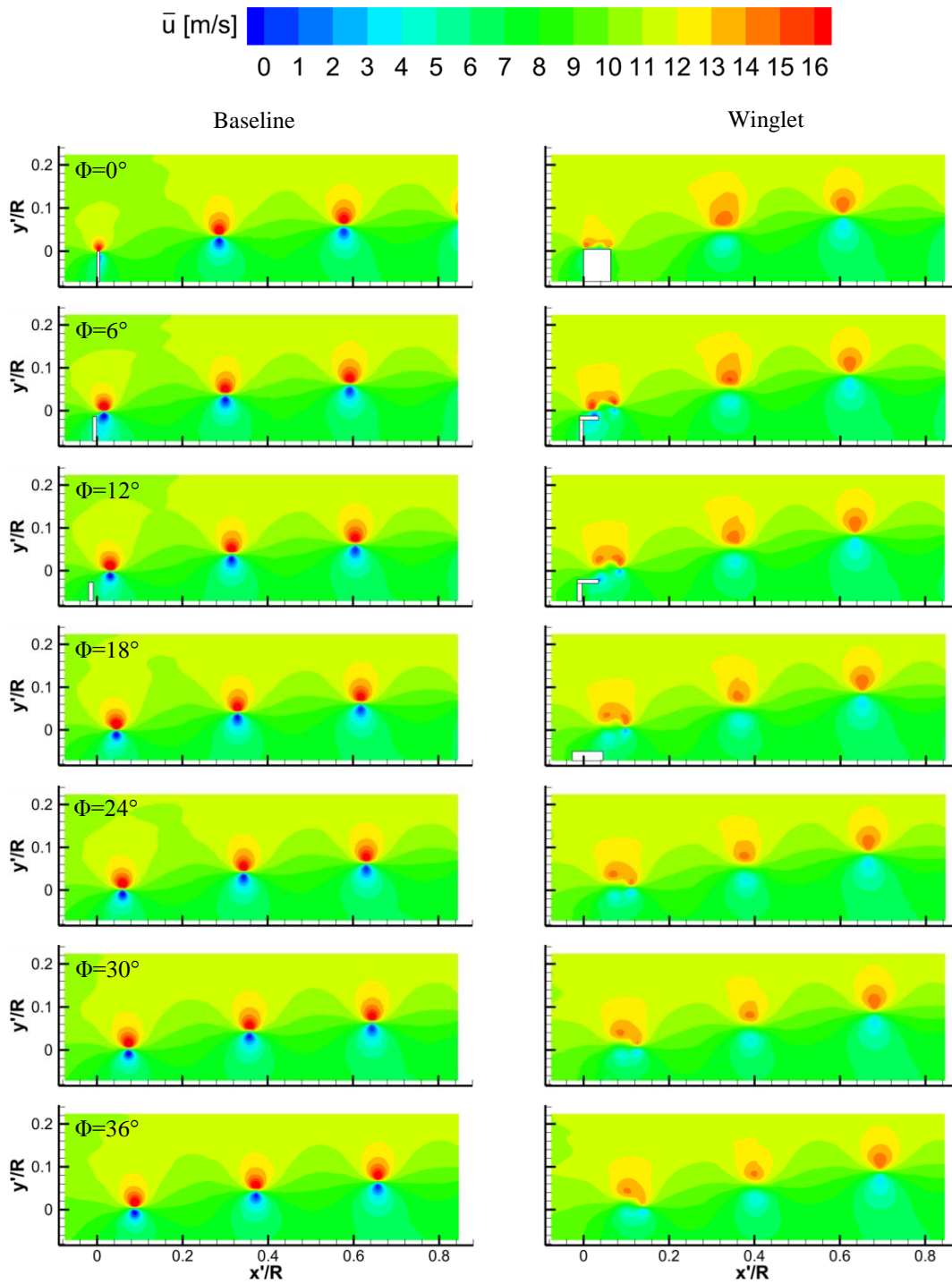


Figure A. 1 Phase-averaged distribution of axial velocity \bar{u} of rotor phases 0° to 120° for the baseline (left) and winglet (right) cases with 6-degree intervals.

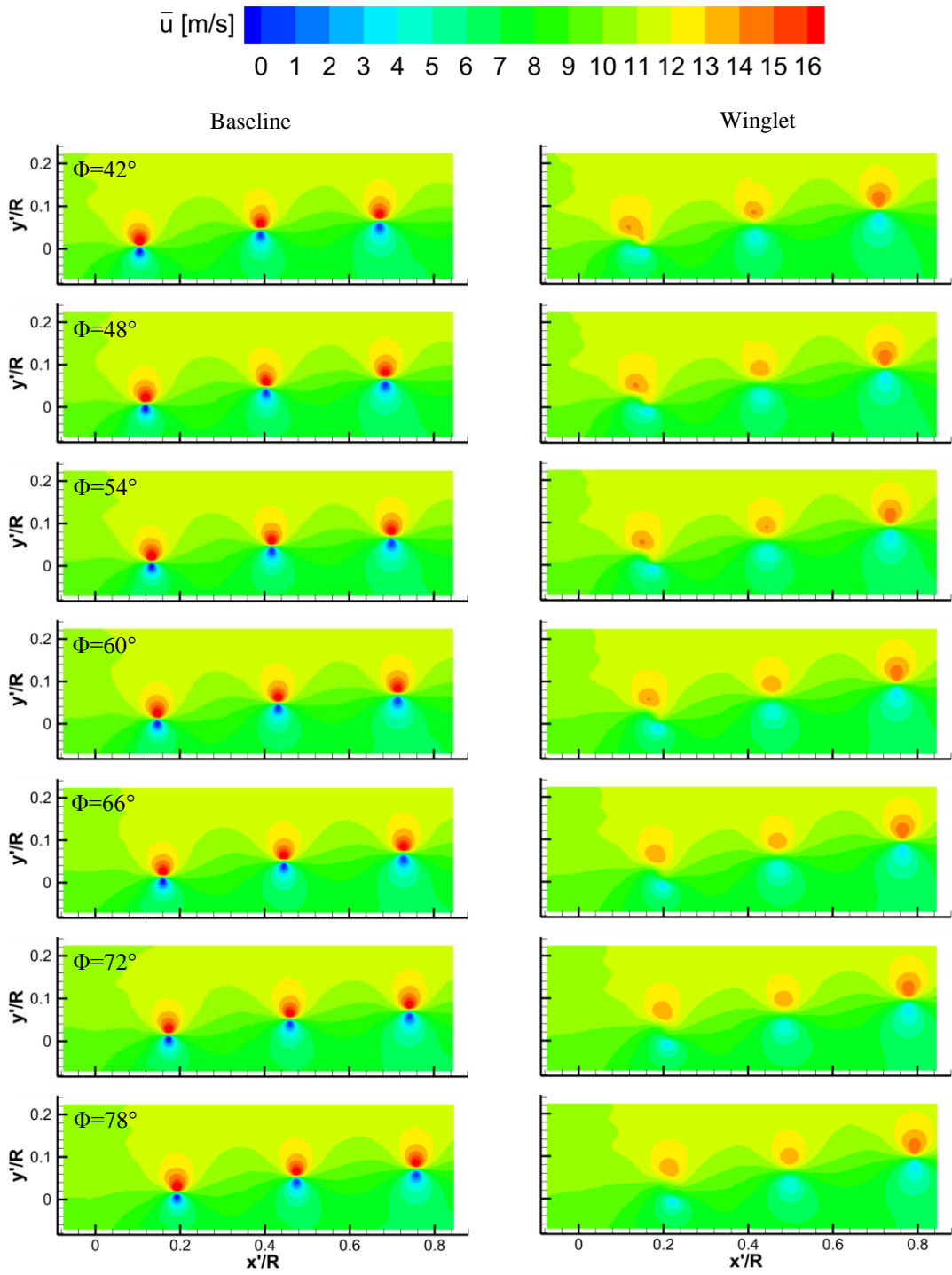


Figure A. 1 (continued).

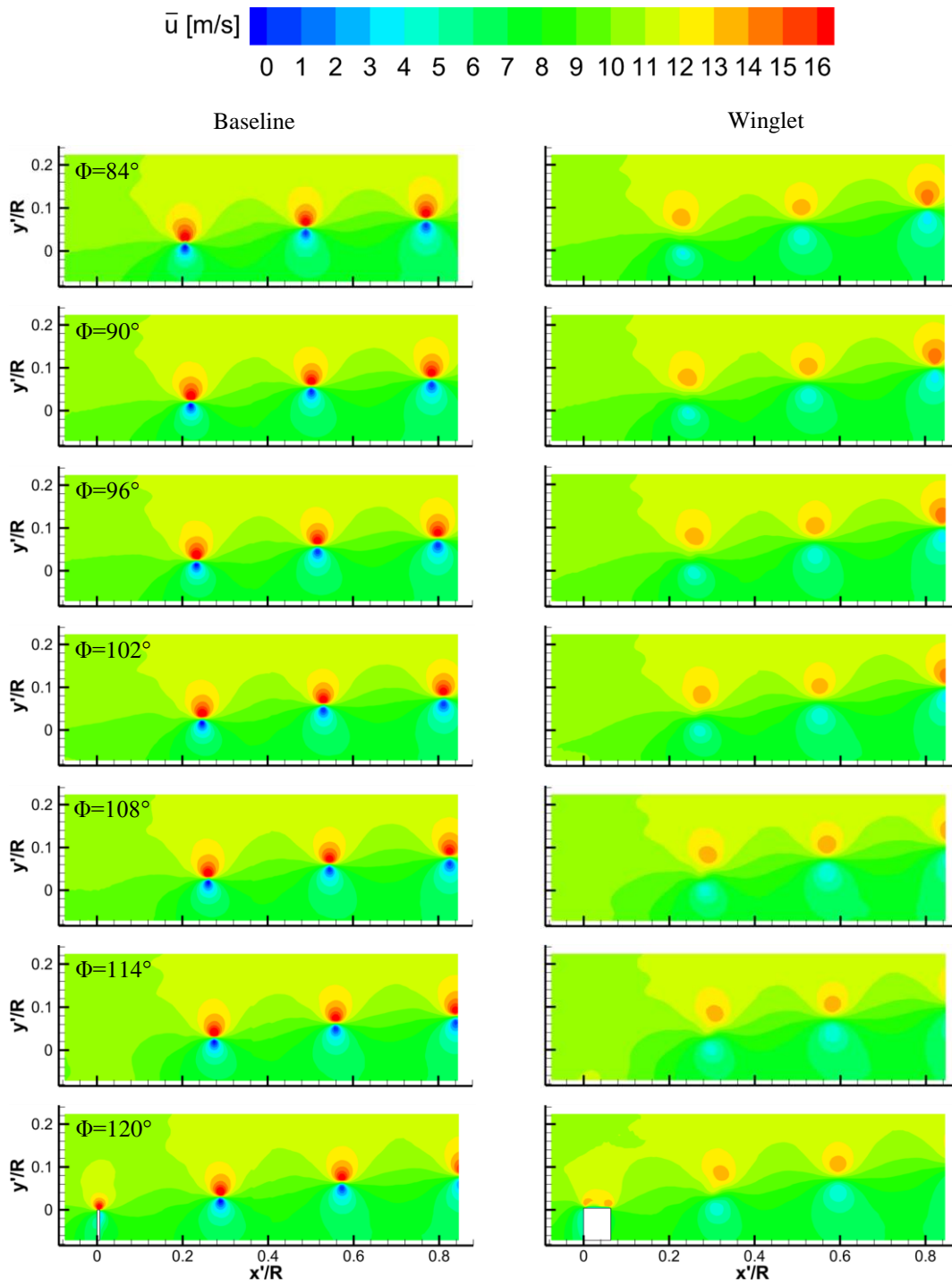


Figure A. 1 (continued).

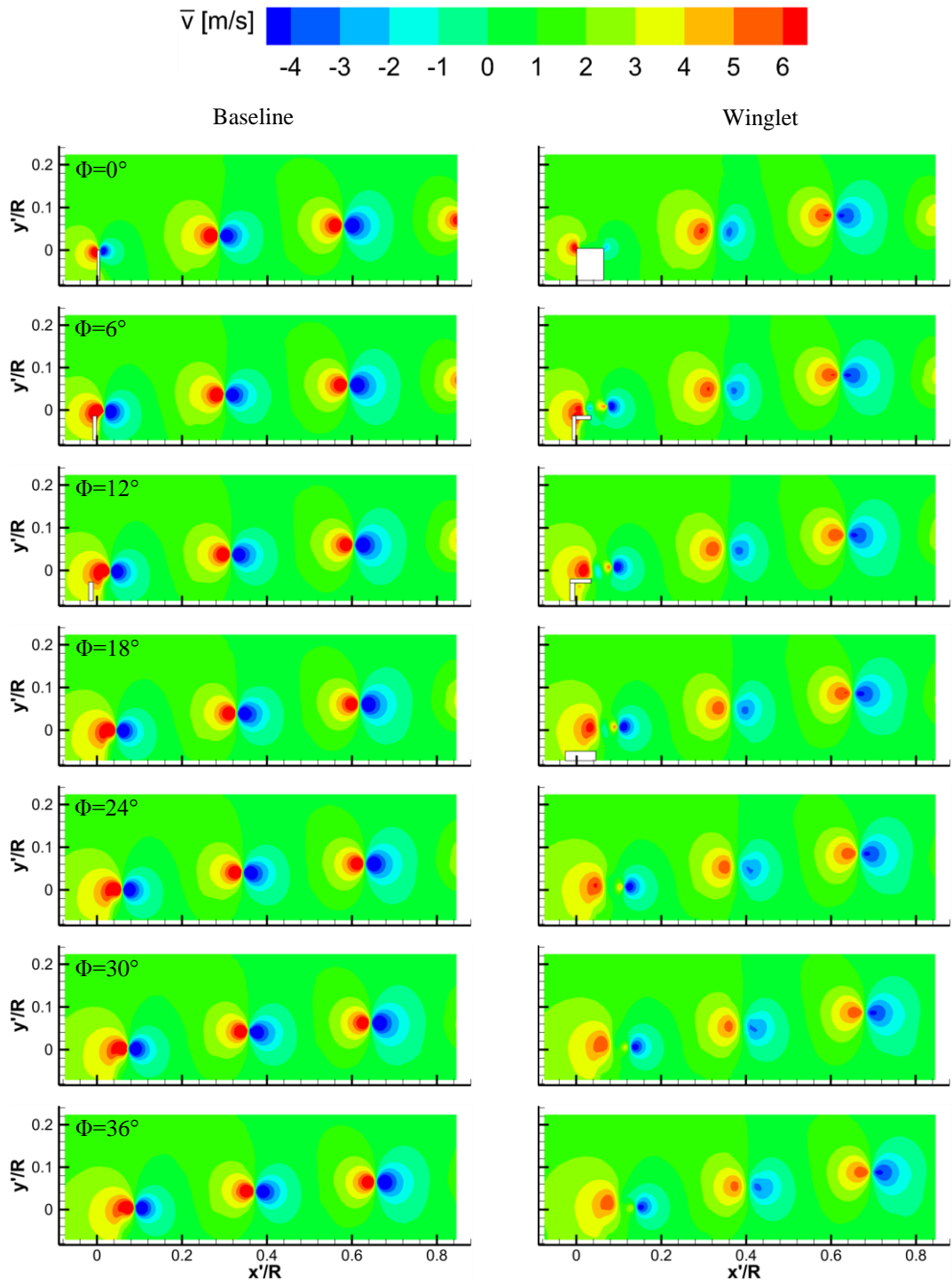


Figure A. 2 Phase-averaged distribution of axial velocity \bar{v} of rotor phases 0° to 120° for the baseline (left) and winglet (right) cases with 6-degree intervals.

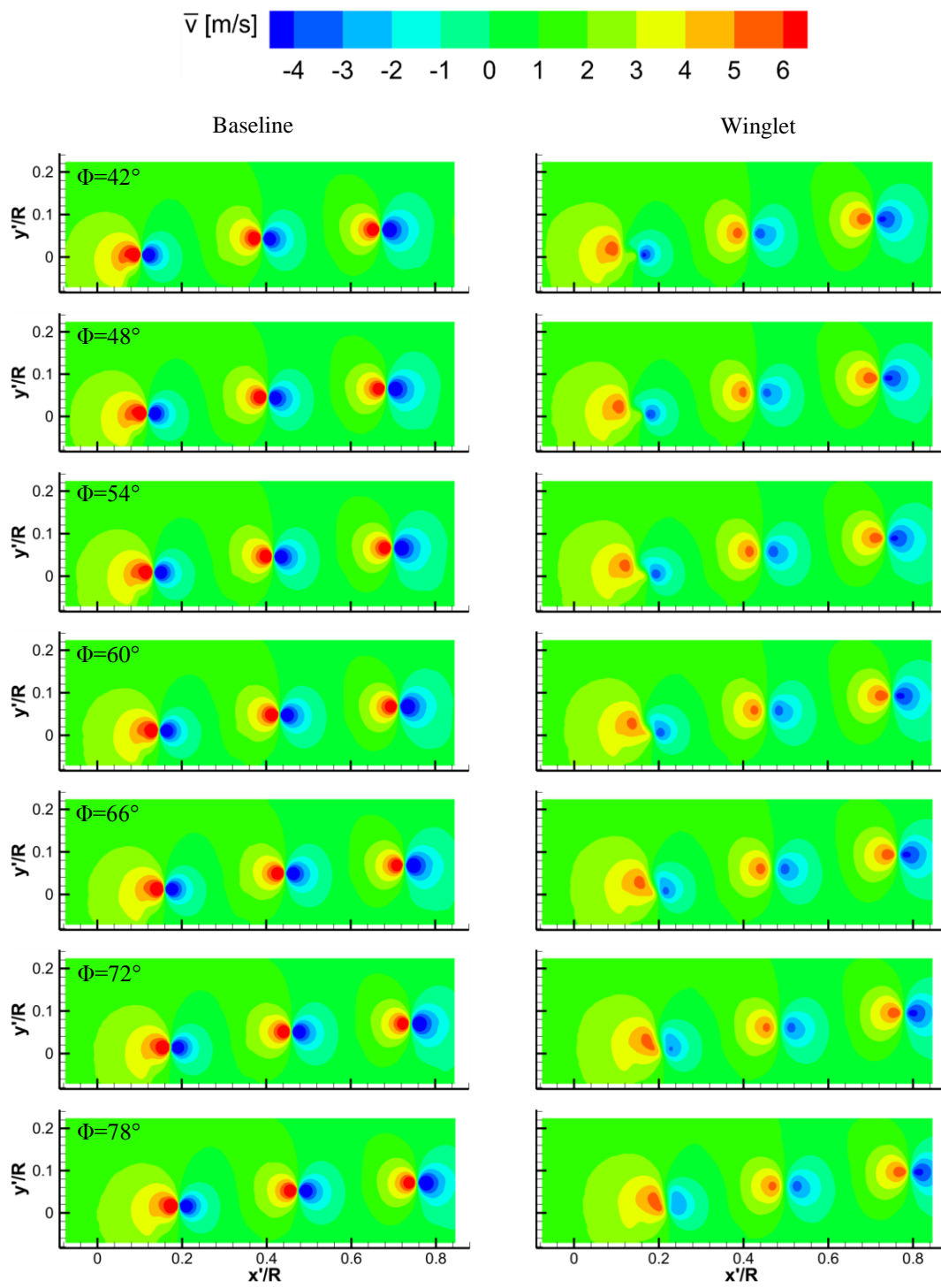


Figure A. 2 (continued).

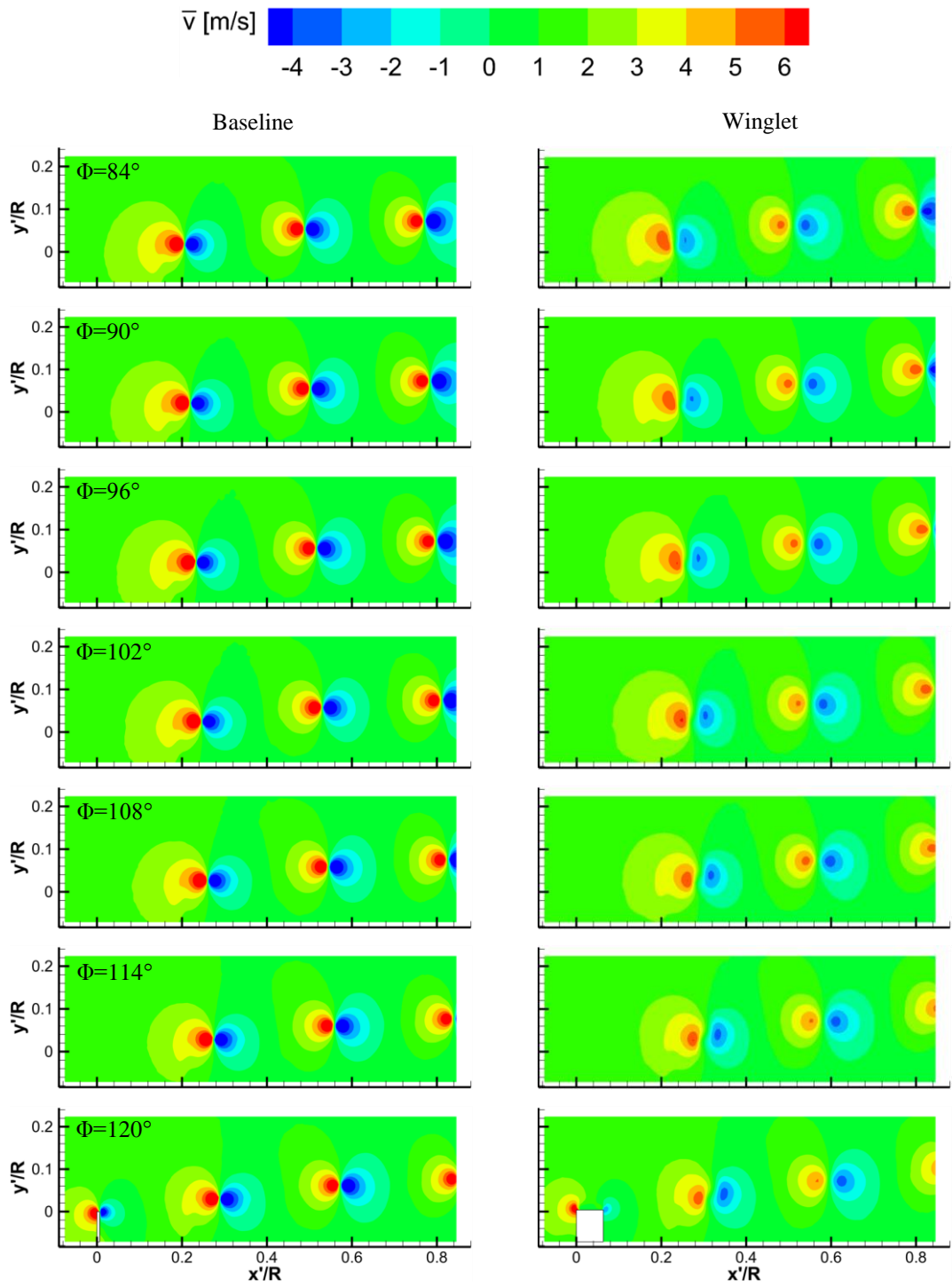


Figure A. 2 (continued).

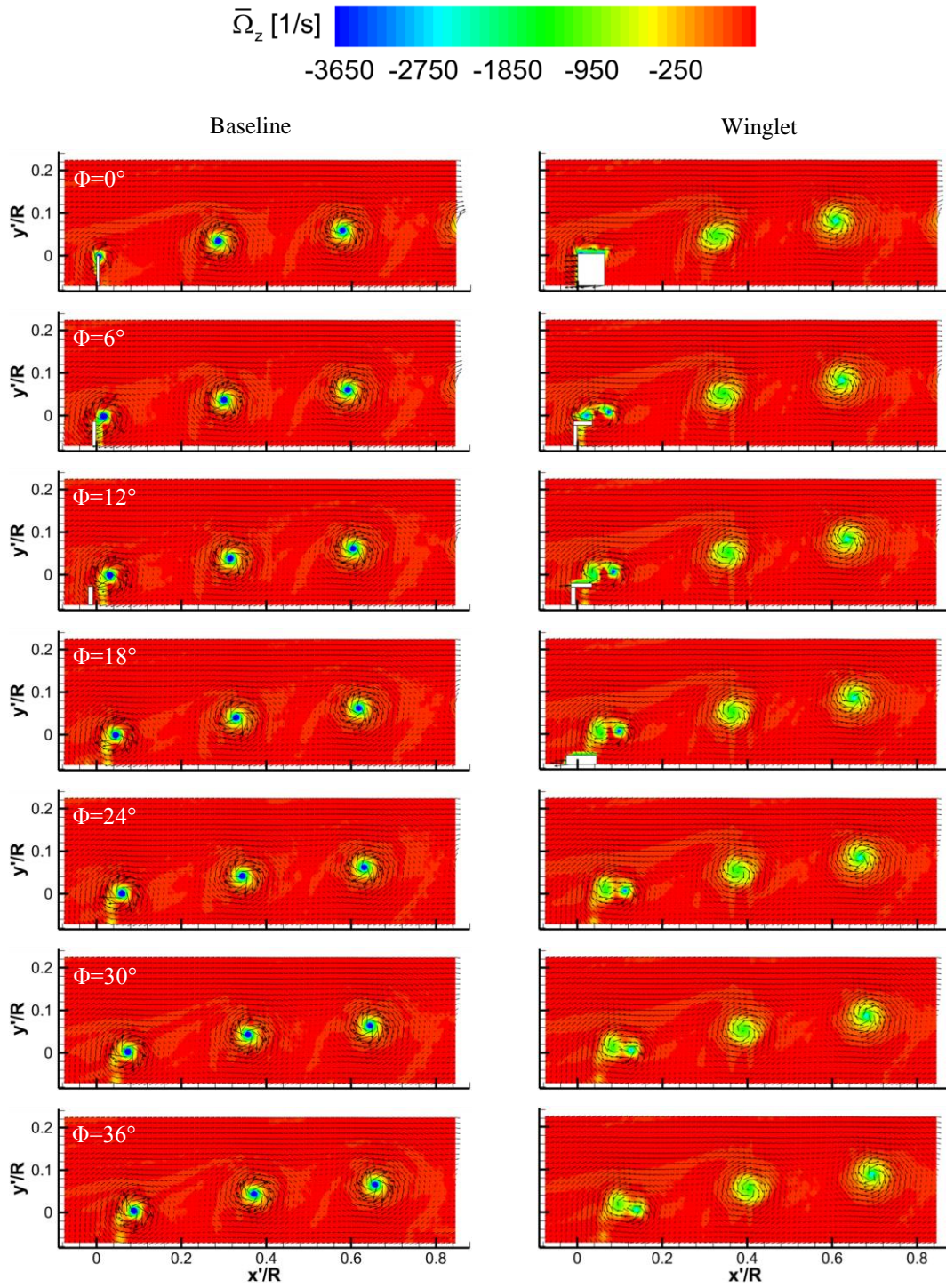


Figure A. 3 Phase-averaged distribution of out-of-plane vorticity ($\overline{\Omega_z}$) of rotor phases 0° to 120° for the baseline (left) and winglet (right) cases with 6-degree interval.

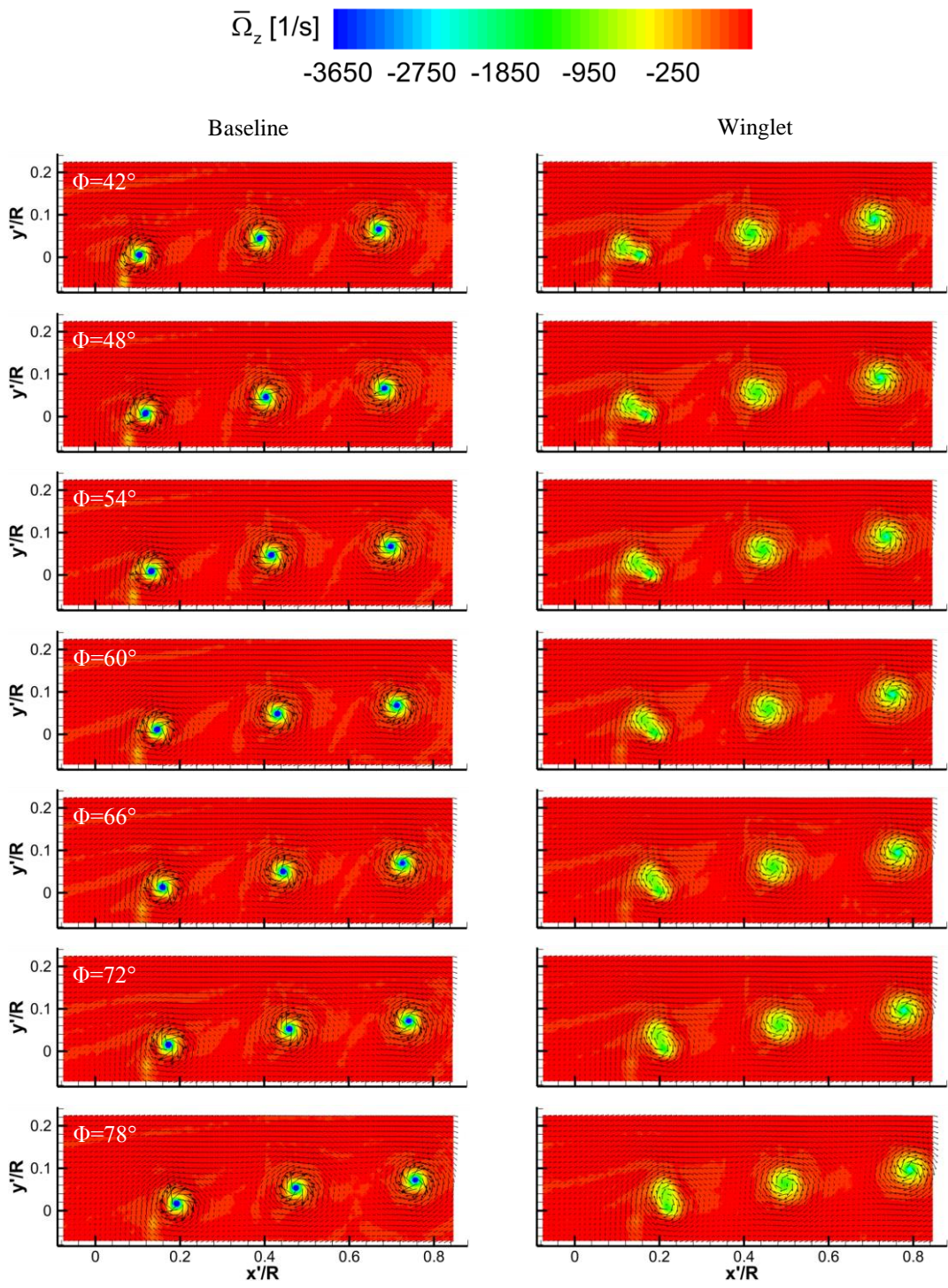


Figure A. 3 (continued).

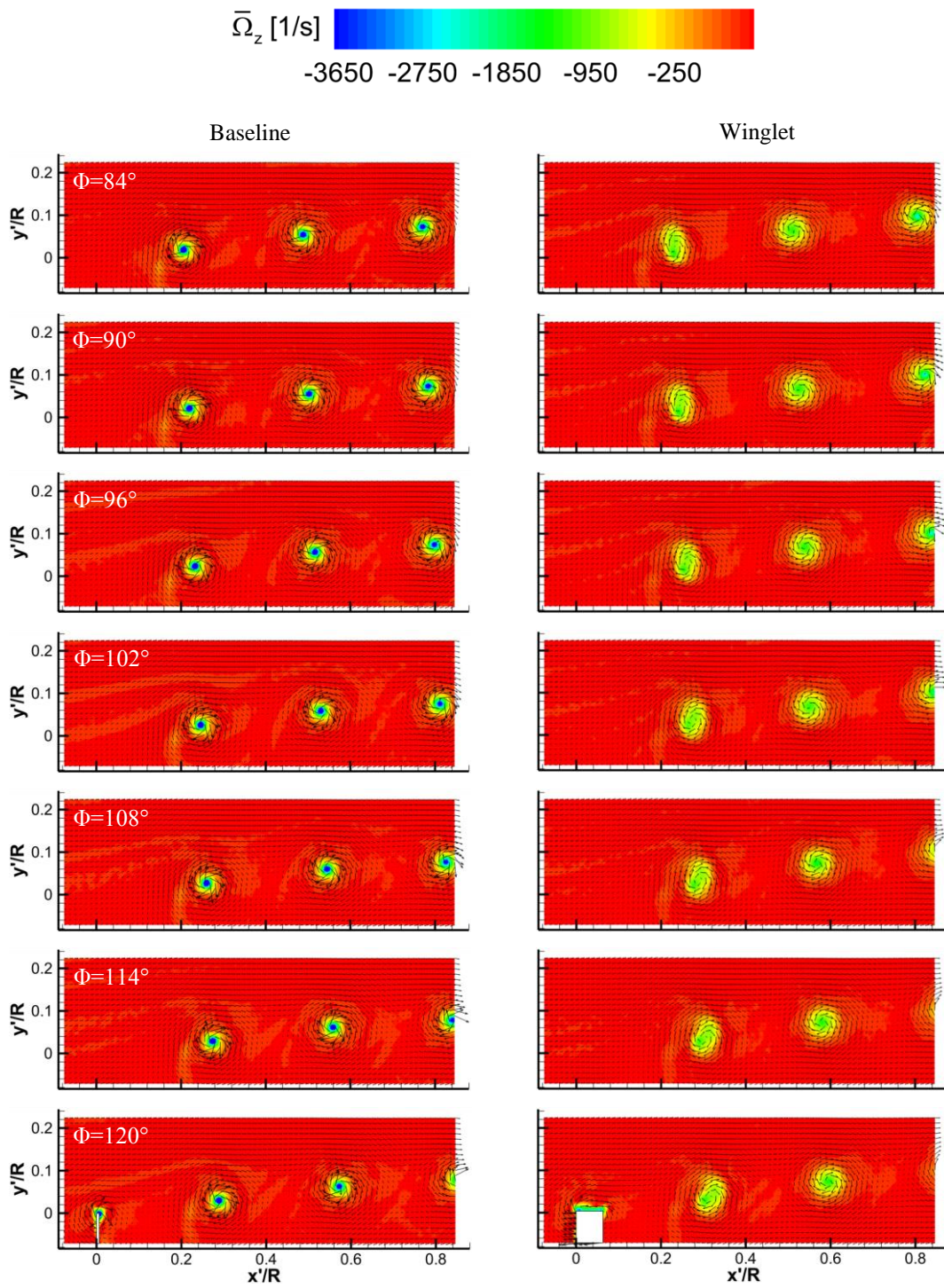


Figure A. 3 (continued).

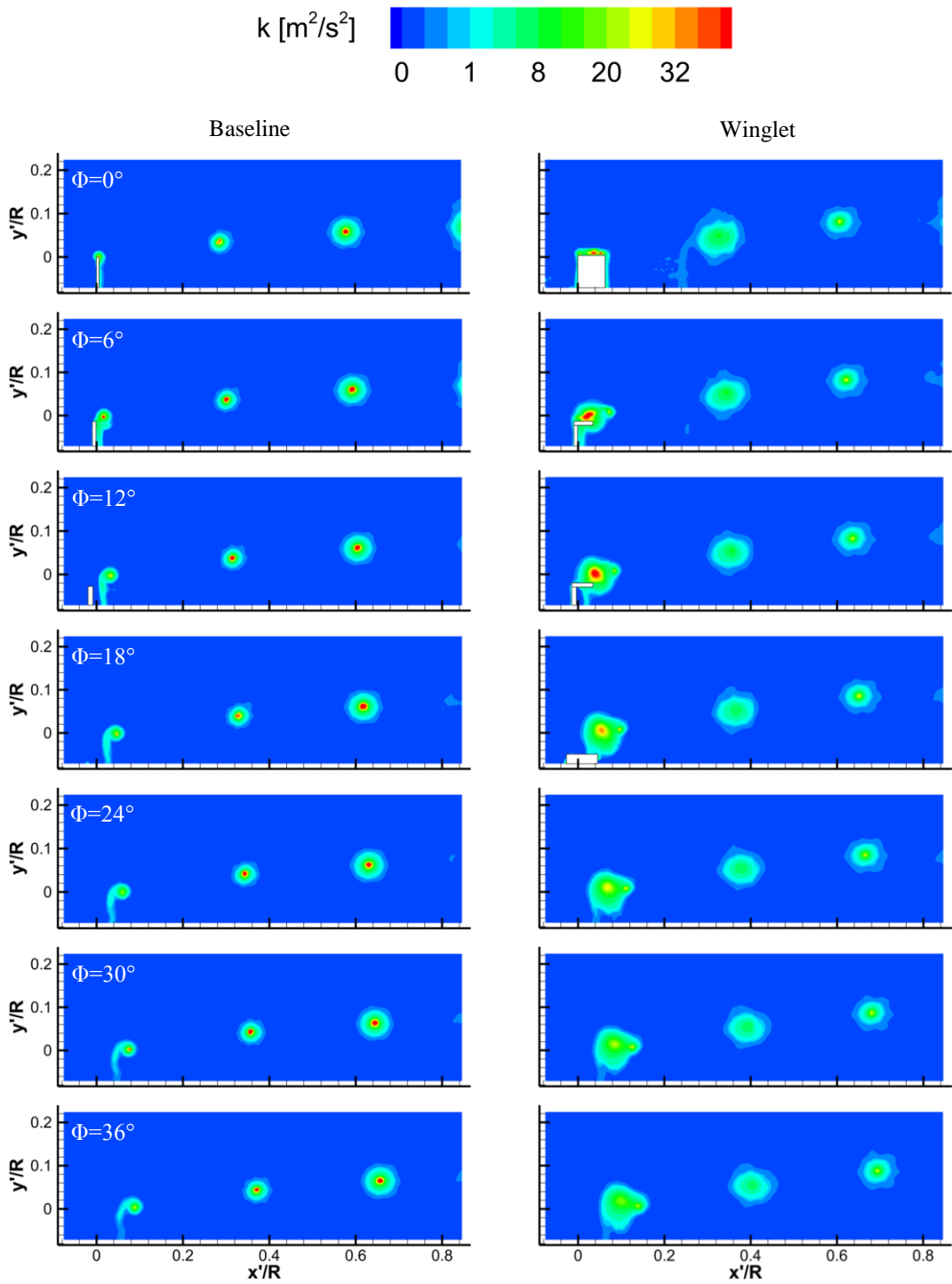


Figure A. 4 Turbulent kinetic energy distribution of rotor phases 0° to 120° for the baseline (left) and winglet (right) cases with 6-degree intervals.

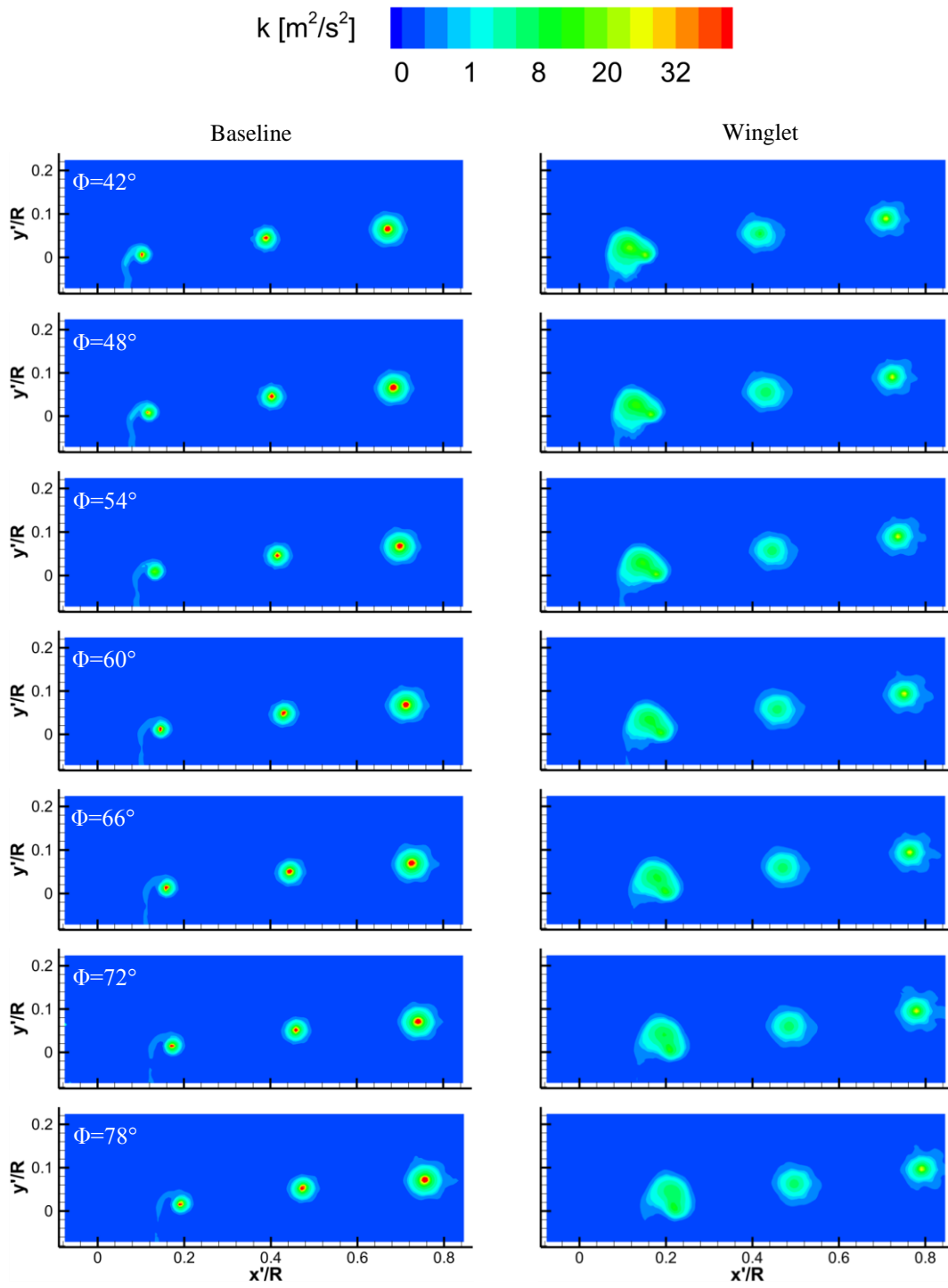


Figure A. 4 (continued).

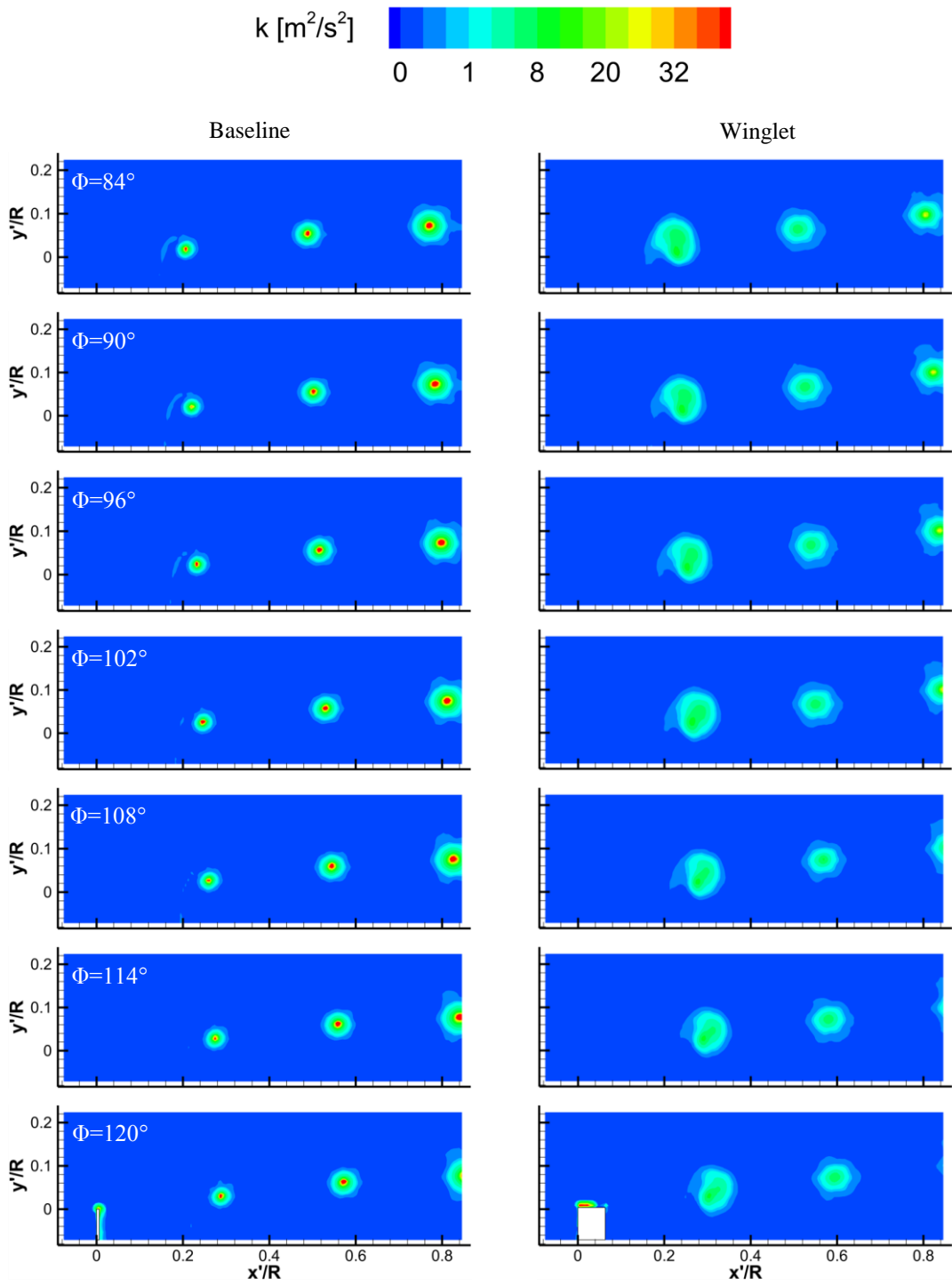


Figure A. 4 (continued).

CURRICULUM VITAE

PERSONAL INFORMATION

Surname, Name: Ostovan, Yasar

Nationality: Turkish (TC)

Date and Place of Birth: 28 June 1984, Karaj, Iran

Marital Status: Single

Phone: +90 539 241 3226

Email: yashar.ostovan@metu.edu.tr

EDUCATION

Degree	Institution	Year of Graduation
M.Sc.	METU, Aerospace Engineering	2011
B.Sc.	Azad University, Tehran, Iran	2006
High School	NODET High School, Urmia, Iran	2001

WORK EXPERIENCE

Year	Place	Enrollment
2012-Present	METU Center for Wind Energy (RÜZGEM)	Experimental Aerodynamicist
2010-2012	Turbotek Turbomachinery Technologies	R&D Engineer

LANGUAGES

English, Turkish, Persian, Azeri

PUBLICATIONS

Article

1- Ostovan Y, Akpolat M, Uzol O Experimental Investigation of the Effects of Winglets on the Tip Vortex Behavior of a Model Horizontal Axis Wind Turbine using Particle Image Velocimetry. Submitted to Journal of Solar Energy Engineering -

Including Wind Energy and Building Energy Conservation.

2- Ostovan Y, Uzol O. Experimental Study on the Effects of Winglets on the Performance of Two Interacting Horizontal Axis Model Wind Turbines. *J Phys Conf Ser* 2016;753:22015. doi:10.1088/1742-6596/753/2/022015.

3- Abdulrahim A, Anik E, Ostovan Y, Uzol O. Effects of tip injection on the performance and near wake characteristics of a model wind turbine rotor. *Renew Energy* 2016;88:73–82. doi:10.1016/j.renene.2015.11.030.

4- Mercan B, Doğan E, Ostovan Y, Uzol O. Effects of camberwise varying tip injection on loss and wake characteristics of a low pressure turbine blade. *Int J Heat Fluid Flow* 2015;54:119–30. doi:10.1016/j.ijheatfluidflow.2015.04.008.

Conference Paper

1- Ostovan Y, Akpolat MT, Uzol O. Experimental Investigation of the Effects of Winglets on the Tip Vortex Behavior of a Model Horizontal Axis Wind Turbine using Particle Image Velocimetry. *Wind energy Sci. Conf.*, Copenhagen, Denmark. 2017.

2- Bartl J, Ostovan Y, Uzol O, Sætran L. Experimental study on power curtailment of three in-line turbines. *Energy Procedia*. 14th Deep Sea Offshore Wind R&D Conf. EERA DeepWind2017, Trondheim, Norway.

3- Orbay E, Bilgen S, Sezer-Uzol N, Ay BO, Ostovan Y. Numerical and Experimental Investigation of Aerodynamic Loads for Tall Buildings with Prismatic and Twisted Forms. *Int. Conf. Wind ENERGY Harvesting*, Coimbra, Portugal

4- Ostovan Y, Anik E, Abdulrahim A, Uzol O, Experimental Investigation of Effects of Tip Injection on the Performance of Two Interacting Wind Turbines. *Conference Proceeding*. Windfarms2015, Leuven, Belgium.

5- Abdulrahim A, Anik E, Ostovan Y, Uzol O. Effects of Tip-Injection on the Flow Downstream of a Model Wind Turbine Rotor Blade Tip. *Conference Proceeding*. 10th PhD Seminar on Wind Energy in Europe October 2014, Orléans, France.

6- Anik E, Abdulrahim a, Ostovan Y, Mercan B, Uzol O. Active control of the tip vortex: an experimental investigation on the performance characteristics of a model turbine. *J Phys Conf Ser* 2014;524:12098. doi:10.1088/1742-6596/524/1/012098.

7- Ostovan Y, Amiri Hazaveh H, Uzol O Aerodynamic Characterization of NREL S826 Airfoil at Low Reynolds Numbers, *Conference on Wind Energy Science and Technology - RUZGEM 2013*, At Ankara, TURKEY.

8- Mercan B, Dođan E, Ostovan Y, Uzol O. Experimental Investigation of the Effects of Waveform Tip Injection in a Low Pressure Turbine Cascade. Vol. 8 Turbomachinery, Parts A, B, C, ASME; 2012, p. 1473. doi:10.1115/GT2012-69316.

9- Ostovan Y, Mutlu T, Onay O, Khalilov J, Kutkan H, ARÇ. AÇIK VE AÇIK JET ODALI RÜZGAR TÜNELLERİNİN TASARIMI , ÜRETİMİ VE. IV. Ulus. HAVACILIK VE UZAY Konf., Istanbul UHUK-2012-000: 2012.

10- Onay O, Khalilov J, Ostovan Y, ARÇ. İNSANSIZ HAVA ARACI PERVANELERİNİN TASARIM , ANALİZ VE TEST. IV. Ulus. HAVACILIK VE UZAY Konf., Istanbul UHUK-2012-000: 2012.

11- Mercan B, Ostovan Y, Dogan E, Uzol O. Effect of Chordwise Modulated Waveform Tip Injection on the Characteristics of the Tip Vortex. 40th Fluid Dyn. Conf. Exhib., Reston, Virigina: American Institute of Aeronautics and Astronautics; 2010, p. 1–8. doi:10.2514/6.2010-4270.

HOBBIES

Snooker, Mountain Climbing, Photography, Motor Sports, Cooking